Optical nonlinearities in semiconductor polariton waveguides

Lloyd Lincoln Charles Tinkler

Submitted for the degree of
Doctor of Philosophy

Department of Physics and Astronomy

August 2015

Abstract

Waveguide polaritons are the quasi-particles arising from the strong coupling of quantum well excitons to the photonic mode of a waveguide. These are complimentary to the polaritons observed in semiconductor microcavities which in the two decades following their first observation have been a rich source of interesting physical phenomena such as parametric scattering, condensation, superfluidity and solitons. Whilst waveguide polaritons are a complimentary scheme they do have a number of important advantages over microcavities, firstly the use of total internal reflection to confine the photonic mode in principle affords lower losses whilst the reduced mode volume increases the coupling to quantum well excitons. Additionally the thin structure more naturally lends the system towards to fabrication of complex polaritonic devices.

The waveguide polariton scheme was first investigated in the late 1980s and early 1990s however the lack of direct access to the dispersion hindered progress. Recently however advancements in photonics have led to the development of integrated grating couplers which are used in this thesis to couple light in an out of the waveguide structure. The relationship between the emission angle from these grating couplers and the internal wavevector is exploited in Chapter 3 to make the first unambiguous observations of waveguide polaritons by a direct observation characteristic anti-crossing dispersion indicative of the strong coupling regime.

In the second half of Chapter 3 the design of the waveguide device was improved by adding further quantum wells to increase the Rabi-splitting and reduce the effect of absorption in the tail of the exciton line. It is then shown that the strong coupling regime is preserved in this device up to 100 K.

In Chapter 4 it is shown that the interactions between polaritons inherited from the exciton component leads to a optical nonlinearity which causes the defocusing of high intensity beams travelling through the waveguide. This nonlinearity can be described as a negative nonlinear refractive index which can support the generation of single or pairs of dark-spatial solitons depending on the initial conditions. Finally this nonlinearity is also shown to persist to 100 K suggesting the possibility of future polaritonic devices operating at higher temperatures.

In Chapter 5 it is shown that the curvature of the polariton dispersion in the anti-crossing regions gives rise to a massive group velocity dispersion which causes the dilation of injected pulses as they propagate along the waveguide. At high particle densities within the pulse this group velocity can be balanced against the optical nonlinearity arising from inter-particle interactions to form bright temporal solitons. Finally due to the comparable nonlinear-, diffractive- and dispersive-length scales it is shown that this system support the formation of a hereto unobserved hybrid of a spatially-dark and temporally-bright soliton.

In this thesis waveguide polaritons are reintroduced as a complimentary system to microcavities and the first observations made of their formation and interactions. This thesis lays the foundation for future studies into waveguide polaritons and showcases their nonlinear properties through the study of spatio-temporal solitons.

Dedicated to my family, and to Helen.

Acknowledgements

This work was funded by a scholarship from the University of Sheffield for which I am grateful.

I would like to thank my supervisor Dr Dmitry Krizhanovskii his guidance, advice and foresight which bore fruitful results. My thanks go to Prof. Maurice Skolnick for his guidance and advice. And I would like to thank Dr Paul Walker who helped me in every aspect of this work, from lab to MATLAB.

Thank you to all those in the LDSD group for your insightful and enlightening conversations, and for the irrelevant and incoherent ones. It has been a been a great privilege to work along side you and pleasure to become friends with you all.

Finally I thank my friends, my family, and most of all Helen, for their understanding, support and love.

Contents

Abbreviations and terminology

BEC ..... Bose-Einstein condensation.

CCD ..... Charge-coupled device.

CVD ..... Chemical vapour deposition.

CW ..... Continuous wave.

DBR ..... Distributed Bragg reflector.

FDTD ..... Finite-difference time-domain.

FWHM ..... Full-width at half-maximum.

FWTM ..... Full-width at one-third of maximum.

FWM ..... Four wave mixing.

GVD ..... Group velocity dispersion.

LHS, RHS .... Left- and right-hand side.

LPB, UPB .... Lower and upper polariton branch respectively.

MBE ..... Molecular beam epitiaxy.

NLSE ..... Nonlinear Schrödinger equation.

OPA, OPO .... Optical parametric amplifier and oscillator respectively.

PhC ..... Photonic crystal.

PID ..... Proportional-integral-differential.

PL ..... Photoluminescence.

QW ..... Quantum well.

SEM ..... Scanning electron micrograph.

SPM ..... Self-phase modulation.

TIR ..... Total internal reflection.

TE, TM ..... Transverse-electric and -magnetic respectively.

ToF ..... Time of flight.

VCSEL ..... Vertical cavity, surface emitting laser.

β ..... In-plane wavenumber inside the waveguide.

Ω ..... Vacuum Rabi splitting.

Δ ..... Detuning between photon and exciton modes.

δ ..... Detuning between exciton and the lower polariton branch.

E_{UP}, E_{LP} ..... Energy of the upper- and lower-polariton branch.

E_X ..... Energy of the exciton transition.

E_C ..... Energy of the TE mode of the waveguide.

k_B ..... Boltzmann constant.

v_g^c, v_g ..... Group velocity of the bare waveguide and of polaritons.

$|C|^2, |X|^2$ ..... Photon and exciton Hopfield coefficients.

List of Figures

List of Publications

L. Tinkler, P. M. Walker, E. Clarke, D. N. Krizhanovskii, F. Bastiman, M. Durska, and M. S. Skolnick, *Design and characterization of high optical quality InGaAs/GaAs/AlGaAs-based polariton microcavities*, Appl. Phys. Lett. **106**, 021109 (2015).

L. Tinkler, P. M. Walker, D. V. Skryabin, A. Yulin, B. Royall, I. Farrer, D. A. Ritchie, D. N. Krizhanovskii, and M. S. Skolnick, *Ultra-Low-Power Hybrid Light-Matter Solitons*, arXiv:1409.0725 (2014).

P. M. Walker, L. Tinkler, M. Durska, D. M. Whittaker, D. N. Krizhanovskii, M. S. Skolnick, I. Farrer and D. A. Ritchie, *Exciton Polaritons in Semiconductor Waveguides*, Appl. Phys. Lett. **102**, 012109 (2013).

Chapter 1

Introduction

The consequences of light coupling to excitons in bulk semiconductors was first considered in the 1950s by S. I. Pekar. The term *polariton* was later coined by J. J. Hopfield [1] to describe the "dressed photons" arising when light with a particular wavevector inside the crystal is repeatedly and reversibly absorbed to form and exciton before being re-emitted at the same wavevector. In this strong coupling regime the wavefunction can no longer be separated into an excitonic and photonic part but instead should be considered as a quasi-particle which possesses characteristics of either species. Polaritons were initially investigated in systems such as bulk CuCl [2] and CdS [3] crystals however the difficulty of optically accessing and manipulating in three dimensions ultimately limit their usefulness.

In the 1990s the technological advancements in VCSELs (vertical cavity, surface emitting lasers) made possible the growth of high quality semiconductor microcavities. Such microcavity devices consist of two distributed Bragg-reflectors (DBR) mirrors forming a Fabry-Pérot cavity with quantum wells (QWs) placed at the antinodes of the electric field inside the cavity: this is shown schematically in Figure 1.1a along with an example of the corresponding dispersion. For small wavenumbers the photons within the cavity have a parabolic dispersion whilst the dispersion of the relatively heavy excitons is approximately flat. In the strong coupling regime two new eigenmodes appear known as the upper- and lower-polariton branches (E_{UP} and E_{LP} respectively) which show a characteristic anti-crossing behaviour. The

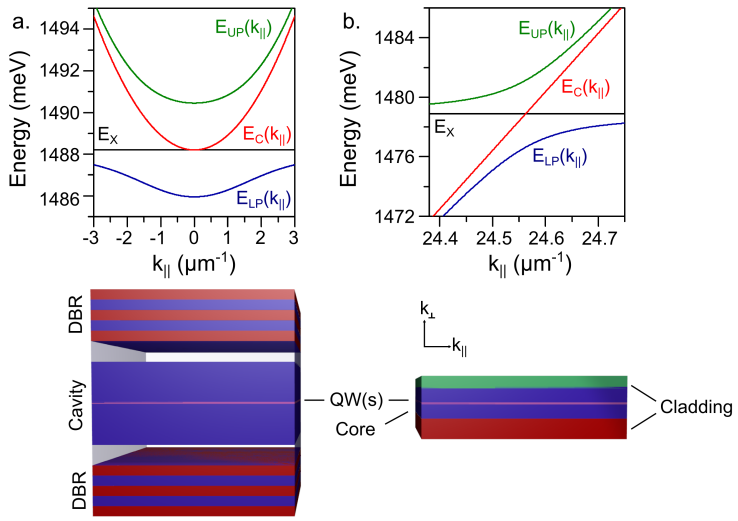

Figure 1.1: Structure and exemplar dispersion of a microcavity (a) and waveguide device (b). Here E_X is the energy of exciton transition, $E_C(k_\parallel)$ is the photon energy, and $E_{UP}(k_\parallel)$ and $E_{LP}(k_\parallel)$ are the upper and lower polariton branches.

closest approach between these modes is called the vacuum Rabi-splitting (or often simply Rabi-splitting) in analogue to atom-cavity systems and is a measure of the coupling strength. The polaritons formed are free to move in two dimensions parallel to the growth direction and may be detected by their decay into photons which tunnel through the mirrors.

Since the first observation by Weisbuch *et al* in 1992 [4] microcavity polaritons have inspired a huge body of literature [5, 6, 7], accelerated by ground-breaking studies of parametric scattering processes [8, 9], non-equilibrium Bose-Einstein condensation (BEC)[1] [10, 11], vortices [12, 13] and superfluidity [14]. Recent years have seen considerable effort towards the development of *polaritonic* devices such as logic elements [15], diodes [16], transistors [17, 18] as well as LEDs [19, 20] and polariton lasers [21].

In this work a complimentary scheme is studied in which the photonic component is instead confined by total internal reflection (TIR) within a semiconductor slab waveguide. This is shown schematically in Figure 1.1b along with an example of the dispersion which illustrates the similarities shared with microcavities.

[1]The exact nature of polariton BECs has been the subject to much debate and is therefore often referred to instead as a *polariton condensate*.

This waveguide scheme has however several important advantages over microcavities. Firstly the use of TIR can, in principle afford lower losses whilst operating at such large wavenumbers by necessity, means that polaritons may propagate long distances within their lifetime. Additionally the smaller photonic mode volume yields a larger Rabi splitting through the greater overlap with the QW. This means that fewer QWs can be used, retaining the strong polariton-polariton interactions inherited from the exciton component which provides huge optical nonlinearities.

From a technological point of view this scheme is advantageous as the photonic mode is certain to be in resonance with the exciton at some wavenumber - in contrast to microcavities where this is fixed by the structure - making the scheme insensitive to variation in growth. Additionally the large number of epitaxially grown layers in a microcavity mean significant strain energy is accumulated which may be released by forming dislocations that strongly modify the potential landscape. This factor requires careful design consideration to achieve high quality devices [22, 23] whereas in the waveguide scheme this is not such a concern. Furthermore whilst the creation of wires [24] or complex structures such as Mach-Zehnder interferometer [25] or photonic crystals (PhCs) [26] require etching through microns of DBR mirrors in a microcavity, control over the photonic mode can be achieved n the waveguide scheme by etching just a few nanometers into the cladding and guide layers. The waveguide scheme therefore naturally lends itself to the fabrication of complex integrated optical circuits, combining the established field of photonics with the large nonlinear effects found in polariton systems.

These *quantum well waveguides* - hereafter *polariton waveguides* - were first investigated in the late 1980s and early 1990s through time of flight measurements which showed the group velocity dispersion associated with the polariton dispersion in AlGaAs- [27, 28] and AlGaN-based waveguides [29]. Since then there have been demonstrations of electric field tuning [30], on-chip directional couplers and Mach-Zehnder interferometers [31, 32] however these previous studies have failed to make the same impact as those on microcavity devices. This may be attributed to the success of microcavities themselves and to the difficulty of realising similar effects in

polariton waveguides. These difficulties stem from the lack of direct optical access to polariton dispersion and critically, a lack of the potential minimum at $k_{\|} = 0$. However it may be possible to overcome these issues using PhCs [33, 34] or gratings etched into the guide to engineer the dispersion. Therefore given the maturity of the respective fields of polariton physics and photonics the time is ripe to revisit polariton waveguides with the motivation of their potential as a platform for optical on-chip processing. Crucially, the previous ventures into polariton waveguides have not unambiguously demonstrated the presence of polaritons nor observed the nonlinear effects associated with strong polariton-polariton interactions. In this thesis the presence of polaritons is evidenced by direct observation of the characteristic anti-crossing dispersion and their nonlinear properties investigated through observations of spatial and temporal solitons.

The nonlinear properties of polaritons derive from the exciton component from which they inherit strong repulsive inter-particle interactions leading to a strong $\chi^{(3)}$-type nonlinearity. The nonlinear properties of polaritons were first investigated at the turn of the millennium in seminal works in which pairs of polaritons were resonantly excited at the *magic* angle ($k_{\|} = k_{pump}$) and then scatter to the ground (signal) state ($k_{\|} = 0$) and to an idler state ($k_{idler} = 2k_{pump}$), conserving both energy and momentum. This scattering process can be stimulated using a weak probe beam to establish a small population in one of the final states [8] or spontaneously seeded by thermally excited polaritons [9]. Drawing analogues with four-wave mixing (FWM) processes in nonlinear optics these cases were likened to an optical parametric amplifier (OPA) or an optical parameteric oscillator (OPO) respectively. In either case these stimulated scattering processes result in a massive, and coherent redistribution of polaritons [35].

The repulsive interactions between particles has a dramatic effect on polariton systems. At high density the effect of interactions result in a blueshift of the occupied mode. Other effects are well illustrated in the OPO scheme, where interactions dictate the temporal coherence of the OPO signal [36] by translating fluctuations in population to fluctuations in energy; and dictate the healing length of the fluid and

thus the physical size of features such as vortices [37].

It has recently been shown that this Kerr-like nonlinearity can be used to generated squeezed light from microcavity pillars [38] which may be useful for continuous-variable optical information processing [39]. Additionally it has also been proposed that given sufficient confinement the interaction-driven blueshift might be exploited using the blockade effect to create single photon sources. In this scheme the presence of a single polariton inside the cavity shifts the system out of resonance with a driving field, preventing a second polariton from entering [40]. To this end novel *open*-cavity systems have been developed where the two DBR mirrors can be positioned individually and where hemispherical mirrors provide photonic confinement on the micron level [41] and potentially to the sub-micron level required for the polariton blockade effect.

These strong interactions also act between polaritons and excitons, causing a local blueshift in the potential landscape which can be used to accelerate [42] or create a potential barrier to a propagating condensate [43, 44]. Finally a condensate travelling through an exciton reservoir can trigger stimulated scattering from the reservoir to amplify the signal [45].

These previous works on microcavities stand as testament to the nonlinear optical properties of polariton systems. A concept well-known in non-linear optics, and of potential use for information transfer is that of a soliton. A soliton is a wave which maintains it shape in time or space over propagation, held together by a balance of dispersive, or diffractive effects and some nonlinearity. The first reported observation of a soliton was famously made by a Scottish engineer called John Scott Russell. In his *Report on Waves* of 1844 [46] Scott Russell describes observing a barge drawn along by horses on the Union Canal near Edinburgh. He noted that when the barge halted suddenly the water accumulated at the bow would continue-on as a rounded, well-defined heap of water, maintaining its shape as it propagated several miles along the channel whilst he pursued on horseback. Figure 1.2 shows a recreation from 1995 of Scott Russell's observation and examples of soliton phenomena observed in other systems. A key feature of all these soliton phenomena is that shape is preserved,

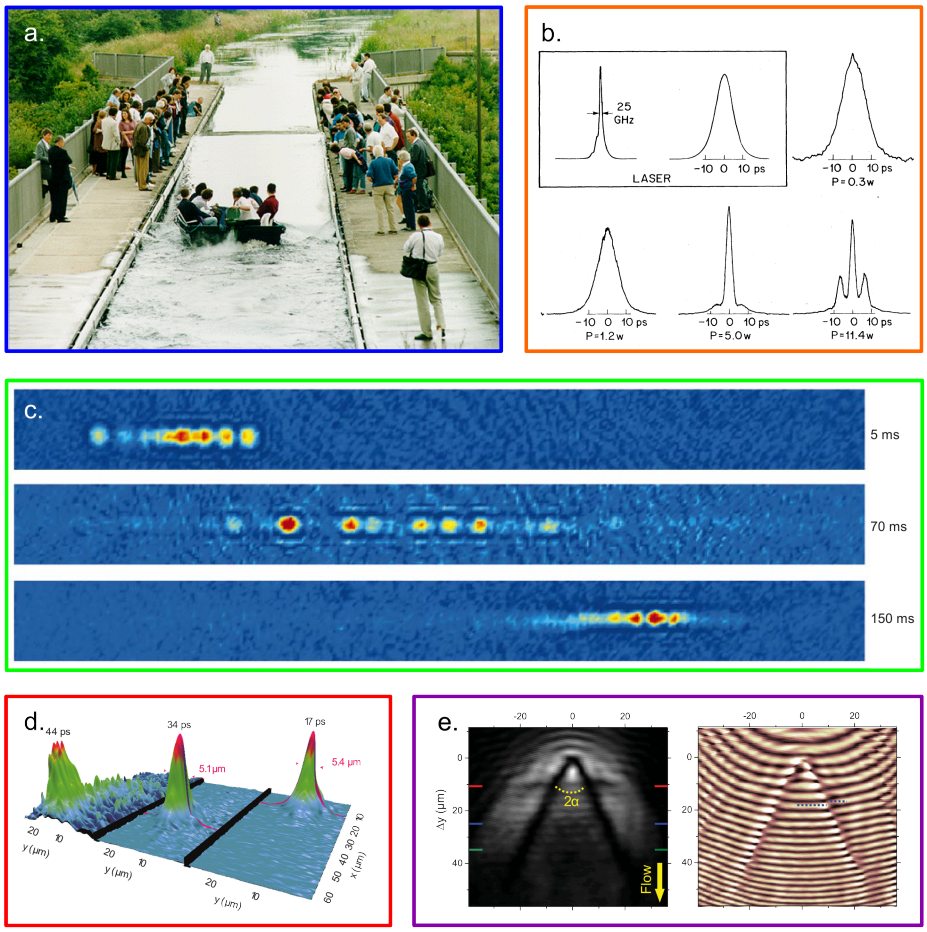

Figure 1.2: Examples of solitons in various systems. (a) Photograph of a reconstruction of Scott Russell's observation of a soliton on the Union Canal near Edinburgh [48]. (b) Autocorrelation signal of output of an optical fibre [49]. (c) Formation of a bright soliton train in a BEC of ^{7}Li atoms [50]. (d) Formation of a bright-temporal soliton of microcavity polaritons [51]. (e) Dark-spatial soliton formed in a polariton superfluid encountering a defect [52].

either in time or equivalently, in space giving classes of temporal and spatial solitons. Additionally, rather than a local increase in amplitude, as Scott Russell's solitary wave, a soliton can also be a local minimum on a bright background. Such dark-solitons have recently been observed in water waves [47] nicely complimenting the original observation by Scott Russell.

Solitonic behaviour has been observed in atomic BECs [53, 50, 54], PhCs [55, 56], semiconductor waveguides [57, 58] and in VCSELs [59]. The most notable application however is in optical fibres - as first demonstrated by Mollenauer *et al* in 1980 [49] - where they can be used to transmit data over vast distances without

degradation, thus increasing the potential throughput of the channel by reducing the guard-time between pulses.

Solitons have similarly proposed as information carriers for on-chip applications. However to study, and to utilise solitons on-chip the length-, and time-scales of the competing diffractive or dispersive and nonlinear effects must be very short. This naturally occurs in polariton systems where the massive group velocity dispersion in the vicinity of the anti-crossing can be balanced against the optical non-linearity arising from polariton-polariton interactions. Recently observations of bright-temporal [51] and dark-spatial solitons [52] in microcavity systems have been the subject of high profile papers. The study of spatio-temporal solitons is therefore of potential interest to both the nonlinear optics and polariton communities in addition to providing an ideal showcase for the properties of waveguide polaritons as a platform.

The majority of this thesis is dedicated to the study of spatio-temporal solitons in polariton waveguides. The remainder of this chapter describes the theoretical background whilst the second chapter describes the experimental techniques. The experimental work is then divided into three chapters: the first of which describes development and characterisation of polariton waveguides; the second describes continuous-wave (CW) experiments investigating the optical non-linearity of the waveguide and observations dark-spatial solitons; and the final experimental chapter describes time-resolved measurements of bright-temporal solitons and hybrid temporally-bright and spatially-dark solitons. The final chapter discusses the future direction of this field and the conclusions of the work.

1.1 Quantum wells and excitons

In a semiconductor the regular arrangment of atoms on a lattice gives rises to the electronic bands that give semiconductors their optical and electronic properties. A simplified diagram of the band structure is given in Figure 1.3a, showing the valance- (E_v) and conduction-bands (E_c). The valance-band is the highest occupied level at 0 K whilst the conduction-band is the lowest energy at which electrons are free

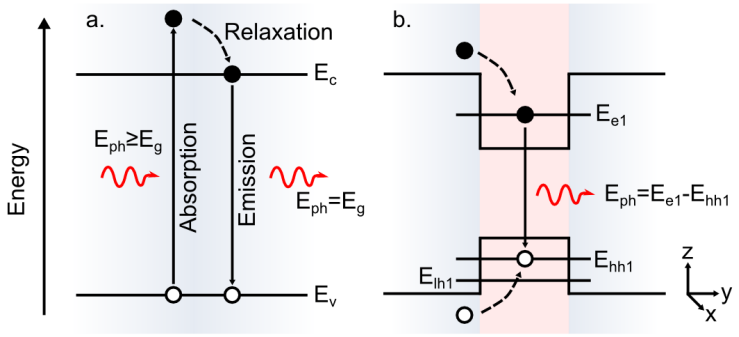

Figure 1.3: Schematics of the band structure in a bulk semiconductor (a) and in a quantum well (b) illustrating the processes of absorption, relaxation and spontaneous recombination. Electrons are depicted as solid black circles whilst holes are shown as empty circles.

to move within the crystal. The difference in energy between these two is known as the band gap (E_g) and is characteristic of the material.

When a photon with energy $E_{ph} \geq E_g$ impinges upon the semiconductor it may be absorbed with the result of promoting an electron to the conduction band, leaving a hole in the valance band. These carriers relax towards the edge of their respective bands and may recombine either non-radiatively, or radiatively to emit a photon of energy E_g. This process of absorption, relaxation and emission, shown in Figure 1.3a is the basis of photoluminescence (PL) experiments in which the emitted light is collected and analysed.

Figure 1.3b shows a schematic of the band stucture of a heterostructure. Here a layer of material with a small band gap is sandwiched between layers with a larger band gap, forming a potential well into which carriers fall and are confined. This can be realised in heteroepitaxial schemes such as molecular beam epitaxy (MBE) in which layers of material are grown sequentially on top of one another. Carriers within the well are confined in one dimension but free to move parallel to the growth direction in the x-z plane. At typical realisation of this using III-V materials may be an $\mathrm{In}_x\mathrm{Ga}_{1-x}\mathrm{As}$ QW in GaAs.

If the width of the potential well is comparable to the de Broglie wavelength the confinement results in discrete subbands for the electron and hole as in the textbook example of a particle in a box. In the example the potential is sufficiently

shallow that only one confined state exist for the electron, and heavy- and light-hole bands (E_{e1}, E_{hh1} and E_{lh1} respectively). An electron and hole pair confined to the quantum well experience Coulomb attraction and may bind to form a state in which the pair orbit each other known as an exciton. The energy of this exciton transition (E_x) is therefore the difference in energy between subbands, less the binding energy of the electron-hole pair. As the transition energy of the heavy-hole exciton is less than that of the light-hole exciton this dominates optical spectra, and hence only the former will be considered further.

Electrons have spin $J_e = \pm\frac{1}{2}$ with respect to the growth axis (y) whilst heavy holes have spin $J_{hh} = \pm\frac{3}{2}$. The resulting electron-hole pairs have either spin $J_x = \pm 1$ or 2. As photons have spin $J_c = \pm 1$ only the former is optically active and is referred to as a bright-exciton whilst the later is a dark-exciton. In this work only the bright-exciton is of consequence. In the absence of magnetic or electric fields these spin projections are degenerate. Their large effective mass gives excitons an approximately flat dispersion over a wide range of in-plane wavenumbers, i.e. $E_x(k_{\|}) \approx E_x$.

In III-V materials excitons are only stable at cryogenic temperatures, where the binding energy of the electron-hole pair is greater than the maximum energy of the phonon bath $\sim k_B T$, where k_B is the Boltzmann constant. Therefore all the experiments in this work are performed at low temperature (4-100 K). Additionally at high densities where the interparticle separation becomes comparable to their diameter, known as the Mott density excitons can disassociate forming and electron-hole plasma. Approaching this density results in an increase in exciton linewidth and a reduction in oscillator strength which has consequences to subsequent polariton effects.

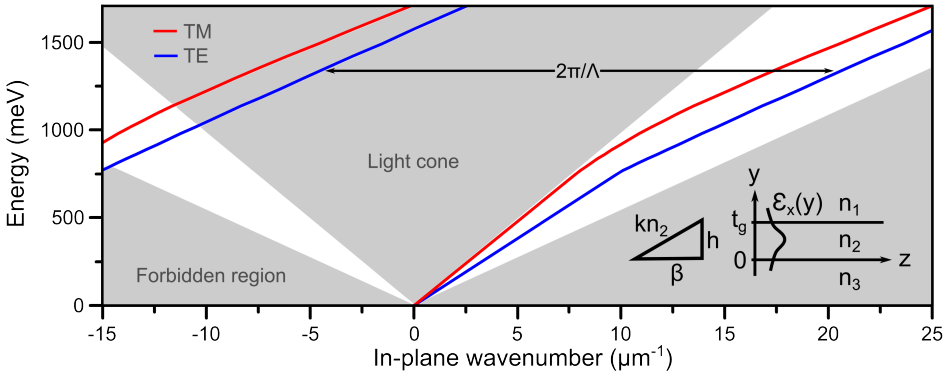

Figure 1.4: Calculated dispersion of the fundamental TE and TM modes of a three-layer slab waveguide of thickness t_g formed by materials of index n_1, n_2 and n_3 as shown schematically bottom left. The dispersion shown here has been calculated for a 135 nm thick GaAs slab waveguide clad in $Al_{0.9}Ga_{0.1}As$ and SiN_x with the imaginary part of their refractive indices set to zero.

1.2 Waveguides

In the simplest case a waveguide may consist of an slab of material of thickness t_g and refractive index n_2 clad in materials of lower index (n_1 and n_3). A schematic of such a structure and an exemplar of the dispersion is shown in Figure 1.4.

If we consider a ray travelling along the z-direction, in order to be guided by TIR the incidence angle formed with the cladding layers must be greater the critical angle arising from Snell's law. By decomposing this ray into the orthogonal components, h and β,[2] we find that guiding occurs for in-plane wavenumbers in excess of $\beta = kn_1$. This line defines the *light cone* shown in Figure 1.4 which contains all the rays which escape the waveguide and may be detected in our experiments. A second, *forbidden* region is defined by the speed of light within the guide, i.e. where $\beta = kn_2$.

From the requirement for the round trip phase to be multiples of 2π we see that β can only take up discrete values between kn_1 and kn_2, corresponding to a particular modes of the waveguide. Formally such an optical mode is a solution to

[2]Hereafter β will denote the in-plane wavenumber inside the guide along the propagation direction whilst k will denote the wavenumber in free space.

Maxwell's wave equation in each layer:

$$\nabla^2\mathbf{E} = \frac{{n_i}^2}{c^2}\frac{\partial^2\mathbf{E}}{\partial t^2},\ i = 1, 2, 3 \tag{1.1}$$

For a wave polarised in x travelling along the z-direction this has solutions of the form:

$$\mathbf{E}(\mathbf{r}, t) = \mathcal{E}_x(y)e^{i(\omega t - \beta_m z)} \tag{1.2}$$

where β_m is the wavenumber of the m^{th}-mode. In the case where $n_2 > n_1, n_3$ the electric field ($\mathcal{E}_x$) is sinusoidal within the guide and decays exponentially in the cladding layers. By applying the condition that the electric- and magnetic fields must be continuous across the boundaries the wave equation can be rearranged to yield a trancendental equation which can be solved graphically or numerically for the tranverse-electric (TE) modes, and with appropriate substitutions, for the transverse-magnetic (TM) modes of the waveguide. Alternatively Equation 1.1 can be solved for arbitrary structures using numerical methods such as the finite-difference time-domain (FDTD) algorithm, or the finite element method (FEM).

In this work only the fundamental modes of the waveguide will be of consequence and so the m^{th}-mode notation will be dropped. Figure 1.4 shows the dispersion of these fundamental TE and TM modes calculated for a 135 nm thick GaAs slab waveguide clad in $Al_{0.9}Ga_{0.1}As$ and SiN_x. Over the range energies of interest in this work (1.45-1.48 eV) these modes are approximately linear and parallel. We may therefore write the energy of either mode as a linear function of wavenumber:

$$E_C^{TE}(\beta) = \hbar v_g^c \beta + E_0 \tag{1.3}$$

$$E_C^{TM}(\beta) = \hbar v_g^c \beta + E_0 + \Delta_{TE-TM} \tag{1.4}$$

where v_g^c is the group velocity of light within the waveguide, E_0 is the energy intersect at $\beta = 0$, and Δ_{TE-TM} is the separation between the TE and TM modes.

1.2.1 Waveguide losses

The performance of a waveguide is characterised by its losses on transmission. This can be due scattering, absorption or radiative losses and are well described as an

exponential decay of the form $I = I_0 e^{-\alpha z}$, where I_0 is the initial intensity and α is the loss coefficient, often expressed as decibels per unit length along z (dB cm^{-1}).

Scattering losses are due to the presence of defects or roughness on the surface of the waveguide or within the crystal itself. In this work the waveguide structures were grown by MBE which produces near perfect crystal structures of very high purity and so losses due to scattering should be negligible.

Radiative losses occur where energy is dissipated into the substrate or cladding. This is generally small for well-confined modes far from cut-off, however imperfections in the crystal can result in coupling to leaky higher-order modes but this is expected to be negligible for the waveguides in this work.

Losses due to absorption can occur by inter- or intra-band transitions. In this work the absorption due intra-band transitions should be minimal as all the devices are undoped and were tested at low temperature (4-100 K) where the free-carrier concentration is negligible. The former can be reduced by choosing the operating wavelength of the waveguide such that the photon energy is well below the band gap of the waveguide material. Here the photon energy was chosen to be 1.45-1.48 eV, well below band edge of GaAs which is 1.519 eV at low temperature [60].

1.2.2 Coupling technology

Whilst using TIR to confine the light has the advantages mentioned previously it does mean some additional device is required to couple light in and out of the guide. The coupling efficiency is strongly dependent upon the modal overlap in space and momentum. The most intuitive scheme is where light is directly injected into the end of the waveguide by matching the input beam profile to the spatial profile of a particular mode. This can be achieved using a optical fibre or laser diode held to the cleaved edge of the waveguide or by focusing through a lens. The coupling efficiency achieved here can be very high, and can improved through integrated couplers which expand the waveguide mode to match the injected mode [61]. Such techniques are problematic in this case however, where the mode volume is small and where sample must be held in an optical cryostat restricting access to the cleaved edge of the

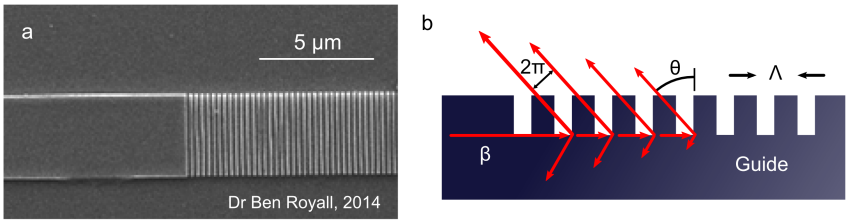

Figure 1.5: Scanning electron micrograph of a diffraction grating etched into the cladding layer of a ridge waveguide (a). Schematic of a grating coupler illustrating the principle of operation (b). Here the grating period (Λ) has been chosen such that $2\pi/\Lambda > \beta$ and so the emission is scattered backwards from the grating at the angle θ.

sample.

A second method is surface-coupling: the most common of which is where a diffraction grating is etched into or deposited onto the waveguide. Figure 1.5a shows an scanning electron micrograph (SEM) of such a grating etched into a the cladding layer of a ridge waveguide. This grating scheme is technologically advantageous as it can be fabricated using conventional methods and can be incorporated into more complex designs and, being integral to the device, is quite robust. However in order to achieve proper mode-matching with an incoming beam the footprint can be quite large.

The grating coupler operates by perturbing the photonic mode in the vicinity of the grating creating spatial harmonics at multiples of $\pm 2\pi/\Lambda$, where Λ is the grating period. The grating period can be chosen such that one of these spatial harmonics now lies within the light cone. This is illustrated in Figure 1.4. The emission angle (θ) is then related to the in-plane wavenumber by:

$$k \sin(\theta) = \beta \pm 2\pi/\Lambda \tag{1.5}$$

The angular dependence of the emission therefore provides information about the internal wavenumber; a factor which has been a considerable boon to experimental studies in microcavities. Similarly, light can be injected into the waveguide by matching the incidence angle and energy to a particular mode and through careful choice of the grating period it can be ensured that light only couples into the desired forward travelling mode. However from conservation of momentum out of plane a

large fraction of the light must also be transmitted towards the substrate as illustrated in Figure 1.5b. Consequently the coupling efficiency is typically only 10-30 % [62]. Such losses may be acceptable to measure the emission but this does severely limit the power which may be coupled into the waveguide. This source of loss may be reduced by engineering the guide such that substrate modes destructively interfere at the lower guide-cladding interface [63].

Consideration must also be given to the finite length of the grating: energy inside the grating region decays exponentially on a characteristic length l, the maximum overlap between this exponential profile and the Gaussian profile from a fibre coupler or laser spot is 80 %. This can be improved by the use of apodized gratings in which the period is varied such that the decay matches the input mode profile [63]. Additionally the exponential decay in the grating also results in an uncertainty $\Delta k = 1/l$ in the external wavenumber and thus emission angle.

1.3 Light-matter coupling

If we now consider the full structure where we have a QW embedded within the slab waveguide a photon travelling along the waveguide close to resonance with the exciton transition may be absorbed to form an exciton, before being re-emitted at the same wavenumber. If the decay rates of the exciton and photonic modes are sufficiently small this process occurs repeatedly in what is known as the strong-coupling regime.

The strong coupling of the TE-mode of a slab waveguide to QW excitons was considered by Beggs *et al* [64, 65] using the transfer matrix matrix method and non-local dielectric response theory. They calculated that a single InGaAs QW placed at the centre of a 150 nm thick GaAs slab waveguide should yield a Rabi splitting of 6.6 meV. This Rabi splitting should be compared with 5.1 meV reported in a semiconductor microcavities containing three InGaAs QWs [14]. The increased coupling strength here arises from the increased overlap between the modes.

Although Beggs and Kavokin do not consider the coupling to the TM-mode in

their work it has been shown within the transfer matrix formalism for a superlattice structure that the coupling reduces according to a $\cos^2$ relationship with incidence angle [66]. This can be understood intuitively by noting that the coupling is dependent upon the electric field amplitude at the plane of the QW which for the TM-mode reduces with incidence angle. As a consequence only the TE-mode of the waveguide is expect to strongly couple to quantum well excitons. Furthermore the detuning between the TE- and TM-modes is sufficiently large that the latter may reasonably be neglected. Hereafter only the TE-mode will be considered and E_C^{TE} will be denoted E_C.

As for a microcavity the dispersion of waveguide polaritons can be described using a two classical coupled-oscillator model:

$$\hat{H} = \begin{pmatrix} E_X + i\gamma_X & \hbar\Omega/2 \\ \hbar\Omega/2 & E_C(\beta) + i\gamma_C \end{pmatrix} \tag{1.6}$$

where Ω is the Rabi-frequency at with energy is transferred between the two modes, and γ_X, γ_C are the linewidths of the exciton and photon modes. Equation 1.6 can be diagonalised to give the dispersion relations of the two new eigenmodes of system known as the upper- and lower-polariton branches (UPB and LPB respectively) which are written as:

$$E_{UP} = \frac{1}{2}\left(E_C(\beta) + E_X + i(\gamma_C + \gamma_X) + \sqrt{(\hbar\Omega)^2 - (\gamma_C + \gamma_X)^2 + \Delta^2}\right) \tag{1.7}$$

$$E_{LP} = \frac{1}{2}\left(E_C(\beta) + E_X + i(\gamma_C + \gamma_X) - \sqrt{(\hbar\Omega)^2 - (\gamma_C + \gamma_X)^2 + \Delta^2}\right) \tag{1.8}$$

where Δ is the detuning, defined as $\Delta = E_C(\beta) - E_X$. Figure 1.6a shows the dispersion of the un-coupled exciton and photon modes and of the two new eigenmodes which demonstrate the anti-crossing behaviour indicative of the strong coupling regime.

Subtracting Equation 1.8 from 1.7 we find that the separation of the two new eigenmodes on resonance $(\Delta = 0)$ is given by:

$$\hbar\Omega' = \sqrt{(\hbar\Omega)^2 - (\gamma_C + \gamma_X)^2} \tag{1.9}$$

from which arises the requirement for strong coupling that $\gamma_C, \gamma_X < \hbar\Omega$. This can be understood as a requirement that the exciton and photon decay rates should

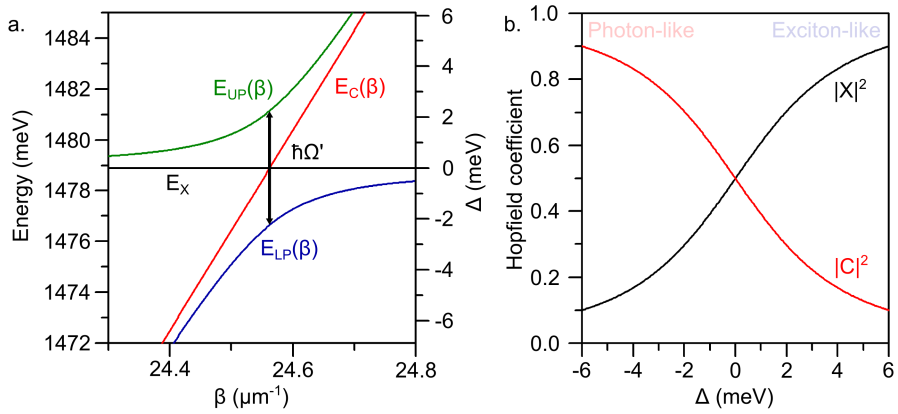

Figure 1.6: Polariton dispersion predicted using the coupled-oscillator model (a) showing the anti-crossing of the upper- and lower polariton branches separated by the Rabi-splitting ($\hbar\Omega'$). Corresponding Hopfield coefficients for the lower polariton branch (b) showing the transition between photon- and exciton-like polaritons with detuning (Δ).

be sufficiently low that the energy undergoes several exchanges between the two modes before decaying. If the linewidths are sufficiently small, the energy splitting between the branches from Equation 1.9 reduces to the Rabi-splitting ($\hbar\Omega' \approx \hbar\Omega$). The homogeneously broadened exciton linewidth is typically around 0.1 meV whilst the inhomogeneously broadened linewidth is around 0.5-1 meV.

Of the two branches the LPB, being at lower energy dominates the optical spectra and is of principle concern. The characteristics of polaritons vary continuously with detuning (Δ) according the photon- and exciton-fractions described by the Hopfield coefficients, denoted $|C|^2$ and $|X|^2$ respectively which for the LPB are defined as:

$$|C|^2 = \frac{1}{2}\left(1 + \frac{\Delta}{\sqrt{(\hbar\Omega)^2 + \Delta^2}}\right) \tag{1.10}$$

$$|X|^2 = \frac{1}{2}\left(1 - \frac{\Delta}{\sqrt{(\hbar\Omega)^2 + \Delta^2}}\right) \tag{1.11}$$

These Hopfield coefficients are shown in Figure 1.6b. For negative Δ polaritons are photon-like $\left(|C|^2 \approx 1\right)$ and travel at group velocities close to that of the bare waveguide. For positive Δ polaritons are exciton-like $\left(|X|^2 \approx 1\right)$ and travel at vanishingly small group velocities but have much stronger inter-particle interactions inherited from the exciton component. Additionally however such polaritons are much closer to the tail of the exciton line and so suffer to greater extent from absorption due to scattering with phonons into the exciton reservoir or with localised

excitons which exist due to fluctuations in the QW potential.

The resulting polariton lifetime cannot be explained by coupled oscillator model from which the lifetime is simply a weighted average of that of the two parent species. In an experimental study of 1997 by Armitage *et al* [67] it was found that the linewidth of the LPB of their microcavity reached a minimum when on resonance. This reduction in linewidth is attributed to *motional narrowing* effect whereby polaritons, having a lower effective mass, are less sensitive than excitons to fluctuations in the potential landscape arising from variation in QW thickness or composition [68].

It has also been suggested that the reduction in linewidth could rather be a result of the asymmetric exciton line often found in real QWs [69]. In this explanation components of the exciton distribution couple to the photon mode with different strengths: those at the centre, where the density of states is greatest, couple strongly whist the components in the tail of the exciton line may only couple weakly. On resonance the polariton branches are sufficiently far from the exciton line that the contributions to the resulting linewidth from components in the tail of the exciton line are negligible. By contrast, far from resonance one of the branches will be sufficiently close to the exciton line that the tail will contribute to the total polariton linewidth.

1.3.1 Group velocity dispersion

Recalling the form of $E_C(\beta)$ for the waveguide from Equation 1.3 and taking the derivative of Equation 1.8 with respect to β yields an expression for the group velocity of polaritons in the LPB with detuning:

$$v_g = \frac{1}{\hbar}\frac{dE_{LP}}{d\beta} = |C|^2 v_g^c \tag{1.12}$$

The variation in group velocity with frequency becomes important when we consider a pulses of light propagating through the waveguide. Spectral components of the pulse travel at different group velocities and so arrive at the end of the waveguide at different times producing a chirp in the output pulse. This property

of a waveguide is characterised by the group velocity dispersion (GVD) parameter β_2, defined as the second derivative of wavenumber with respect to frequency. By convention a negative GVD, which indicates that higher frequencies travel slower with respect to low frequencies is referred to as *normal*, whilst a positive GVD is referred to as *anomalous*. For the polaritons in the LPB the GVD parameter is:

$$\beta_2 \equiv \frac{\partial^2 \beta}{\partial \omega^2} \equiv \frac{\partial}{\partial \omega} \frac{1}{v_g} = -\frac{\hbar^3 \Omega^2}{2 v_g^c \delta^3} \tag{1.13}$$

where δ is the energy of polaritons in the LPB with respect to the exciton energy, $\delta = E_X - E_{LP}$ which is related to the exciton-photon detuning Δ by:

$$\Delta = -\frac{1}{\delta}\left(\left(\frac{\Omega}{2}\right)^2 - \delta^2\right) \tag{1.14}$$

Taking calculated values $v_g^c = 0.28c$ and $\Omega = 6.6$ meV from the work of Beggs *et al* [65], for half exciton-photon polaritons β_2 is in excess of -10^3 ps^2 m^{-1}. This GVD parameter is greater than that found in optical fibres [70], fiber Bragg gratings [71], and in photonic crystal waveguides [55] where the dispersion is been deliberately engineered. Table 1.1 summarises the GVD found in several different systems in which soliton effects have been experimentally demonstrated.

1.3.2 Polariton nonlinearities

Polaritons interact through Coulomb interactions inherited from the exciton component. In semiconductor microcavities the strength of these interactions, denoted g is still the subject of some debate but is expected to be on the order of several μeV μm^2 [14, 72]. In microcavities this is further complicated as excitons of either spin only couple to the correspondingly circularly polarised cavity mode and so their interactions inherit a spin dependence. The inter-particle interaction is then given by $g = \alpha_1 + \alpha_2$, where α_1 and α_2 are the interactions between polaritons of opposite- and like-spins respectively and $\alpha_1 \sim -10\alpha_2$ [73, 74]. At high density these predominantly repulsive interactions results in a renormalisation (blueshift) of the polariton dispersion proportional to the density and the exciton fraction $|X|^2$. The interactions also lead to a broadening of the exciton resonance however this does not

significantly affect the exciton oscillator strength however until the density leads to the ionisation of excitons and thus to a quenching of the strong-coupling regime [75].

In an optical system the nonlinear response can be characterised as a change in refractive index, $n = n_L + n_{NL}(I)$ where n_L is the linear part and n_{NL} is the nonlinear part of the refractive index and I is the intensity of the light. For a Kerr medium the nonlinear part is given by $n_{NL}(I) = n_2 I$. The nonlinear refractive index, n_2 can have either a positive or negative sign. For a beam travelling in a material with a positive n_2 the index locally increases at the centre of the beam causing the beam to focus as if passed through a lens. A positive n_2 can therefore be described as a self-*focusing* nonlinearity whilst a negative n_2 can be described as a self-*defocusing* nonlinearity. From Equation 1.12 we can deduce that a blueshift of the LPB driven by inter-particle interactions has the effect of reducing the effective mode index ($n_{eff} = c/v_g$). Therefore neglecting higher order terms, the effective optical nonlinearity is expected to be characterised by a negative n_2.

The magnitude of this nonlinearity can be estimated by noting that the blueshift of the polariton dispersion, which is proportional to the particle density and scales with exciton fraction $\left(\Delta E = |X|^2 g\rho\right)$, is equivalent to a change in wavenumber ($\Delta k = \Delta E/\hbar v_g$). Taking the calculated parameters from the work of Beggs *et al* and assuming an interaction constant of $g = 1$ μeV μm^2 the effective nonlinear refractive index is expected to be on the order of 10^{-13} m^2 W^{-1}, several orders of magnitude about that found in bulk AlGaAs (10^{-16} m^2 W^{-1}) [76] and silicon (6×10^{-18}m^2 W^{-1}) [56].

To compare the nonlinear properties of systems with different geometries it is convenient to use the effective nonlinear parameter γ which describes the change in wavenumber per unit power normalised to the effective mode area (A_{eff}) given by:

$$\gamma = \frac{n_2 k}{A_{eff}} \left(\frac{n_g}{n_0}\right)^2 \tag{1.15}$$

Takes into account the slow-down effect found in photonic crystals and mode volume which serve to enhance the intensity of the field inside the devices. Table 1.1 lists the effective nonlinear parameters for several material systems in which optical solitons

Table 1.1: Material parameters of systems with experimentally demonstrated soliton effects.

System	β_2 (ps^2m^{-1})	γ ($W^{-1}m^{-1}$)	Ref.
Optical fibres	0.022	0.0011	[70, 49]
Fibre Bragg grating	2000	0.0094	[71]
GaInP PhC WG	1100	920	[55]
AlGaAs WG	1.05	3.0	[77]
Silicon PhC WG	-4700	58	[56]
Silicon-on-insulator WG	-2.15	226	[78]

have been observed from which it can be seen that it is difficult to simultaneously obtain an large dispersive effect and nonlinearity. The waveguide polariton structure however can be considered as a metamaterial which simultaneously exhibits a large GVD and optical nonlinearity, making it particularly suited to the study of optical solitons on short scale lengths and at low power.

1.4 Solitons in nonlinear optics

Solitons arise from the balance between dispersive or diffractive effect and some nonlinearity. Formally the term soliton is restricted to solutions of nonlinear partial differential equations such as the Korteweg-de Vries equation for water waves, or Maxwell's equations for light travelling through a Kerr medium, which have the special property of being shape-invariant in time or space, and on collision of other solitons. The term is often used however to describe solutions of non-integrable systems that display some of the properties of solitons.

For TE-polarised wave travelling in a slab waveguide along the z-direction the electric field is defined in the x-direction by the particular mode, we can therefore write $E(\mathbf{r}) = \mathcal{E}_x(y)A(x,z)e^{-i\beta z}$ where $A(x,z)$ describes the envelope of the beam. Thus the optical intensity which might be recorded experimentally is proportional to $|A|^2$. Substituting $E(\mathbf{r})$ into Maxwell's wave equation (Equation 1.1) and assuming a Kerr-type nonlinearity and making use of the paraxial approximation, that second

derivative with respect to y and z is negligible, yields:

$$i\frac{\partial U}{\partial Z} + \frac{1}{2}\frac{\partial^2 U}{\partial X^2} \pm |U|^2 U = 0 \tag{1.16}$$

This is referred to as the (1+1)D nonlinear Schrödinger equation (NLSE) in reference to that found in quantum mechanics. The (1+1)D refers to one transverse direction, in this case x and the propagation direction, z. Here the following substitutions have been made to give the NLSE in dimensionless units:

$$X = x/w_0,\ Z = z/L_{DF},\ U = A\sqrt{k|n_2|L_{DF}} \tag{1.17}$$

where w_0 is related to the beam waist of the input beam and L_{DF} is the diffraction length which is the characteristic distance over which the cross section of the beam doubles, for a Gaussian beam $L_{DF} = \beta w_0^2$. Again β is the wavenumber inside the guide whilst k is that in free space and n_2 is the nonlinear part of the refractive index.

In certain cases the NSLE can be solved to obtain bright and dark soliton solutions, depending upon the sign of nonlinearity. Additionally because of the equivalence between propagation in space and in time the NLSE can be rewritten to describe temporal solitons.

1.4.1 Spatial solitons

Spatial solitons maintain their shape through the balance between diffraction and an optical nonlinearity. In the case of a self-focusing nonlinearity the refractive index in the region of high intensity effectively forms a waveguide which confines the light [79]. Such self-trapping was first observed for light passing through a sodium-vapour cell [80]. In this case the soliton was stabilised by the nature of the nonlinearity whereas in Kerr media such two-dimensional solitons are generally unstable; the beam undergoing a catastrophic collapse [81] or fragmentation into filaments [82]. In 1972 it was shown by Zakharov and Shabat that the (1+1)D NLSE was integrable for a Kerr media using the inverse scattering method [83], giving rise to a solitonic solution of the form:

$$U(X, Z) = U_0\ \mathrm{sech}(U_0 X)\ e^{iU_0^2 z/2} \tag{1.18}$$

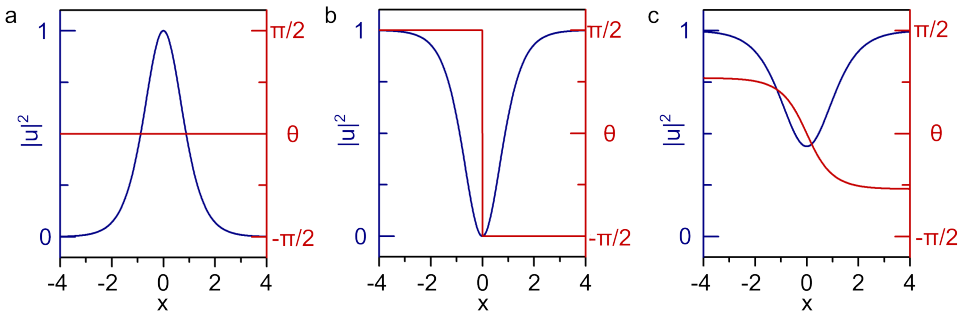

Figure 1.7: Intensity ($|U|^2$) and phase (θ) profiles of the bright, dark and grey-soliton solutions of the nonlinear Schrödinger equation (a, b and c respectively) at $Z = 0$.

where U_0 is the peak amplitude of soliton in the dimensionless units.

It is clear from Equation 1.18 that intensity ($|U|^2$) has a characteristic $\text{sech}^2()$ which does not change as it propagates in the z-direction and so can properly be regarded as solitonic. As the solution consists of a local maximum in space on an otherwise dark background this is known as a bright spatial soliton. The calculated intensity and phase profile of the bright spatial soliton is shown in Figure 1.7a.

From the substitutions made to render the NLSE into dimensionless units in Equation 1.17 the size of the bright soliton is dictated by the dispersion length, the strength of the nonlinearity and the amplitude of the optical intensity. Therefore increasing the power of the beam entering the nonlinear medium should cause the size of the soliton to reduce as the diffractive effects are counteracted by the nonlinear effects to a greater extent.

By contrast to self-focussing media, a plane wave in a self-defocussing nonlinear medium is always stable. Shortly after the discovery of bright solitons it was shown that self-defocussing media could support a soliton solution consisting of a dip in intensity coinciding with a phase jump, on a bright background extending out to infinity in either direction [84]. This solution which has the form:

$$U(X,Z) = U_0\left(\cos\phi\,\tanh(U_0\cos\phi(X - vZ)) + i\sin\phi\right)e^{-iU_0^2 z} \tag{1.19}$$

where $\pi - 2\phi$ is the total phase-shift in radians across the dark notch and is related to the transverse velocity v. For the special case where $2\phi = \pi$ then Equation 1.19 reduces to that of an ideal dark soliton with a characteristic $\tanh^2()$ shape and an

instantaneous phase jump shown in Figure 1.7b. When total phase-shift is less than π the change in phase is more gradual and the minimum intensity of the notch no longer reaches zero. The soliton then travels transverse to the wavefront at some velocity (v) and is referred to as a *grey* soliton. Such a grey soliton is shown in Figure 1.7c for $\phi = \pi/4$. The *blackness* of a grey soliton can be characterised by the size of the dip in intensity relative to the background:

$$Blackness \equiv \frac{|U_{max}|^2 - |U_{min}|^2}{|U_{max}|^2} \tag{1.20}$$

For the soliton given in Equation 1.19 $|U_{min}|^2 = |U(0,0)|^2$ and $|U_{max}|^2 = |U(\pm\infty, 0)|$. Substituting into Equation 1.20 the blackness of the grey soliton is $\cos^2(\phi)$.

Experimentally, dark solitons have been observed by imprinting either the characteristic phase-jump or intensity dip onto the pump before passing through a nonlinear medium. In the latter case this produces pairs of dark solitons with opposite phase that propagate away from one another at some transverse velocity determined by the width of the dark notch at the input. Whilst mathematically dark solitons occur on an infinite bright background - which implies infinite power - in practice they can be observed with a finite width, though the trajectory of soliton pairs is limited to within the pump spot. Such dark solitons were first observed around 1990 in bulk nonlinear media [85, 86] and in nonlinear glass waveguides [87], and subsequently in a range of systems including photovoltaic- [88, 89] photorefractive-crystals [90].

An important potential application of dark solitons arises from the fact that the refractive index is locally lower inside the dark notch than in the surrounding region, effectively forming a waveguide written by the pump beam. Dark solitons have therefore been proposed for use as re-configurable waveguides [91, 92], y-splitters [93] and multiport routers [94].

1.4.2 Temporal solitons

Temporal solitons are formed in the balance of some nonlinearity against the dispersive effects of the channel. Again these solitons are solutions to the NLSE which

after rewriting as a functions of time reads:

$$i\frac{\partial U}{\partial Z} + \frac{1}{2}\frac{\partial^2 U}{\partial \tau^2} \pm |U|^2 U = 0 \tag{1.21}$$

where the following substitutions have been made:

$$\tau = (t - Z/v_g),\ Z = z/L_D,\ U = A\sqrt{|\gamma| L_D} \tag{1.22}$$

Here T_0 is the duration of the input pulse and $L_{DS} = T_0^2/|\beta_2|$ is the dispersion length, which is the characteristic length over which a Gaussian pulse propagates before increasing in duration by a factor of $\sqrt{2}$ due to GVD.

The NLSE from Equation 1.21 has a solitonic solution of the form:

$$U(0, \tau) = N\text{sech}(\tau) \tag{1.23}$$

which corresponds to a bright temporal soliton travelling in the z-direction. The parameter N here describes the order of the soliton:

$$N^2 = \frac{\gamma P_0 T_0^2}{|\beta_2|} \tag{1.24}$$

where P_0 is the peak power of the pulse. For $N = 1$ a pulse with $\text{sech}^2()$ envelope does not change as it propagates and so is referred to as the fundamental soliton. For integer values $N > 1$ the pulse follows a periodic pattern in z. From Equation 1.24 the condition $N = 1$ for the fundamental soliton can be understood as a requirement that the dispersion length must be equal to the nonlinear length $L_{NL} = 1/\gamma P_0$ which is the characteristic length required to develop a phase change 2π.

Considering a pulse of duration $T_0 = 0.5$ ps and using the estimate of β_2 from Section 1.3.1 $L_{DS} = 250$ µm. Equating this to L_{NL} and assuming an effective mode volume $A_{eff} = 10$ µm^2 yields a peak power of $P_0 = 50$ mW corresponding to pulse energies of femto-Joules, orders of magnitude below that observed in comparable systems presented in Table 1.1.

In a system with loss the pulse decays as it propagates; eventually the intensity becomes so small that the nonlinear effect can no longer compensate for the dispersion. At this point the soliton decays and propagates as a dispersing wavepacket. However if the characteristic soliton formation length $L_{DS} \approx L_{NL} < L_{loss}$ then the

soliton adiabatically accommodates the loss by adjusting its temporal width thus maintaining the same soliton number until such point as $L_{DS} > L_{NL}$.

1.5 Solitons in atomic systems

Solitonic phenomena have also been have also been observed in atomic BECs. For a dilute gas of weakly interacting particles at zero temperature the behaviour is well described by the Gross-Pitaevskii equation (GPE) [95]:

$$\left(-\frac{\hbar\nabla^2}{2m} + V_{ext} + g|\psi|^2\right)\psi = E\psi \tag{1.25}$$

where the ψ is the order parameter or wavefunction describing the condensate, V_{ext} is the external potential, m is the mass of the particles and g describes the strength of their interactions.

The GPE has a similar form to the NLSE given in Equation 1.16 - where the interaction strength between particles now plays the role of the nonlinearity - and similarly, if the interactions between particles are repulsive ($g < 0$) has the solution:

$$\psi(x,t) = \psi_0\left(\cos\phi\,\tanh\left(\cos\phi\frac{x-vt}{\xi\sqrt{2}}\right) + i\sin\phi\right) \tag{1.26}$$

corresponding to a dark soliton in the x-direction where $\pi - 2\phi$ is the total phase-shift in radians across the dark notch and $|\psi_0|^2$ is the background particle density. Here $\xi = \hbar/\sqrt{2mg|\psi_0|^2}$ is the healing length of the fluid which is the characteristic length scale of modulations in the density. For the case where $2\phi = \pi$ Equation 1.26 reduces to a fundamental dark soliton. For $2\phi < \pi$ the density and the centre of the dark notch no longer reaches zero and so corresponds to a grey soliton which propagates with velocity $v = c_s\sin\phi$, where $c_s = \sqrt{g|\psi|^2}$ is the speed of sound in the fluid.

Such dark solitons are unstable with respect to density fluctuations in the remaining (y and z) dimensions but have been observed experimentally by confining the condensate through the external potential [54, 96].

From Equation 1.26 the size of the dark soliton in a BEC is dictated by strength of the interactions and the particle density in much the same way as the size of an

optical dark soliton is dictated by the strength of the nonlinearity and the intensity of the optical field. Furthermore the blackness and velocity of the soliton is once again dictated by the total phase change across its centre.

Finally, if the interactions between particles are attractive ($g > 0$) the GPE also has a solution:

$$\psi(x) = \psi_0 \frac{1}{\cosh\left(x/\xi\sqrt{2}\right)} \tag{1.27}$$

corresponding to a bright soliton in the x-direction where once again the size of the soliton is dictated by the healing length, and therefore by the density of the fluid and the strength of the particle interactions. This bright soliton solution is also unstable but has been observed experimentally with tight radial confinement through an external potential [50, 53].

1.6 Solitons in polariton systems

Recently a number of soliton-like phenomena have been observed semiconductor microcavities, the underlying physics is similar to that that introduced in Section 1.5. Unlike atomic condensates however where the particle number is conserved, in semiconductor microcavites polaritons decay either by non-radiative recombination of the exciton or by photons tunnelling through the DBR mirrors. Microcavity polaritons typically have a lifetime on the order of 10s ps [97, 98] and up to 100 ps in ultra-high-Q devices [99]. Polariton phenomena are therefore intrinsically out of equilibrium and require some external feed of polaritons to be sustained. In the work of Sich *et al* [51] they realised bright polariton solitons in a semiconductor microcavity as proposed by Egorov *et al* [100, 101]. The feeding was achieved using a linearly polarised CW pump to create a low density population at the inflection point of the polariton dispersion where the effective mass is negative. A cross-polarised pulsed writing beam was then used to locally trigger a high density wavepacket utilising the polariton bistability. The initial self-focusing of the wavepacket due to the negative effective mass is then balanced against the repulsive polariton-polariton interactions. They subsequently showed that linearly polarised solitons are unstable due to po-

larisation multistability [102] whilst circularly polarised solitons are stabilised by a synchronisation between the non-degenerate TE- and TM-modes of the cavity [103]. Recently the group at the University of Sheffield have also shown that by altering the geometry of the writing beam they can excite trains or arrays of bright solitons [104]. Importantly due to the losses in the system which necessitate the use of CW pump to replenish the population these are termed *dissipative* solitons to distinguish them from conservative solitons where the particle number is maintained as in water waves or atomic BECs.

In a study of polariton superfluidity by Amo *et al* the feeding of polaritons was achieved using a triggered-OPO (TOPO) scheme [105]. A CW pump was used to create a polariton population below the threshold for condensation at some finite in-plane wavenumber. A pulsed idler beam with large in-plane momentum was then used to locally trigger the scattering polaritons into a lower-momentum signal state. Using angle resolved spectroscopy they noted a linearised Bogoliubov dispersion indicative of the superfluid regime [106]. The excited droplet therefore did not disperse as it propagates but cannot be considered as solitonic as the polariton-polariton interactions serve to stimulate scattering into the signal state, replenishing the population in the droplet rather than stabilising the wavepacket.

Subsequently Amo *et al* observed the formation of dark soliton pairs in the subsonic superfluid flow nucleated by a natural defect in the microcavity [52]. These solitons propagate with a transverse velocity dictated by the velocity of the flow relative to the speed of sound in the fluid which, in turn is dictated by the polariton density and their interactions. Using interference measurements they observed the characteristic phase jump approaching π coinciding with the dip to zero intensity which is clear evidence of a dark soliton.

In conclusion waveguide polaritons are a revived scheme which is expected to simultaneously display both large GVD and highly nonlinear properties arising from polariton-polariton interactions. This makes waveguide polaritons particularly suited for the study of solitonic effects which will be the subject of this thesis.

Chapter 2

Experimental methods

This chapter reviews the key techniques and procedures used in this body of work.

All experiments were performed at low temperature (5 K) in optical cryostats of either of a cold-finger or vapour-flow type. In the former the sample is mounted in an evacuated chamber (10^{-5} mBar) on a copper finger attached to a heat exchanger. Liquid helium is drawn by vacuum from a dewar through a capillary in the heat exchanger, cooling the copper cold-finger and sample. In the vapour-flow cryostat the helium is drawn through the sample chamber, cooling the sample directly. In this case the cryostat has an insulating high-vacuum jacket.

In temperature dependence measurements the temperature was monitored using a factory-fitted and -calibrated sensor mounted on the heat exchanger of the cold-finger cryostat. The temperature was adjusted through the helium flow rate and stabilised using a resistive heater-coil inside the cryostat connected to a PID (proportional-integral-derivative) controller.

The sample under test was excited using laser focused through a lens - often a microscope objective - to a spot on the sample surface. The resulting PL emission was collected through this same lens and imaged onto the entrance slit of a spectrometer. The spectra was collected using either a HORIBA TRIAX^{TM} 550- or 350-series single-grating spectrometer equipped with Princeton Instruments PIXIS^{TM} 1024 $\times$ 1024 pixel CCD (charge coupled device) cameras with a pixel size of 13 μm affording a spectral resolution of 0.2-0.3 Å.

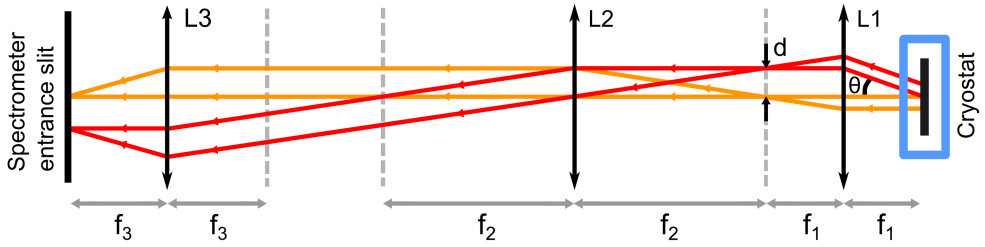

Figure 2.1: Schematic of the experimental setup used in angle-resolved spectroscopy measurements consisting of three lens labelled $L1$-$L3$ here which the focal length $f1$-$f3$. Here the orange rays leave the sample parallel to the optical axis and normal to the surface whilst the red rays leave at an angle θ.

2.1 Angle-resolved spectroscopy

Angle-resolved spectroscopic measurements were made by imaging the Fourier transform of the PL emission onto the entrance slit of the spectrometer. Figure 2.1 illustrates the principle of this technique. Parallel rays leaving the sample surface pass through the same point in the plane one focal length behind the imaging lens. The angular dependence (θ) of the emission at the sample surface is therefore transformed into a spatial dependence (d) in the Fourier plane given by:

$$d = f_1 \sin(\theta) \tag{2.1}$$

where f_1 is the focal length of the objective lens (L1). This plane is then imaged onto the entrance slit of the spectrometer and dispersed onto the CCD camera. The vertical axis of the resulting two-dimensional spectrum can then be rescaled to give the angular dependence of the emission.

2.2 Continuous-wave experiments

In Chapters 3 and 4 polaritons were excited using CW excitation. Figure 2.2 shows a schematic of the experimental setup. Excitation was provided by either a Ti:Sapphire laser which could be tuned continuously from 790-850 nm, or by a diode laser emitting at 685 nm. The position of the pump spot could be changed by slightly tilting M3 whilst the angle of incidence can be adjusted by moving M3

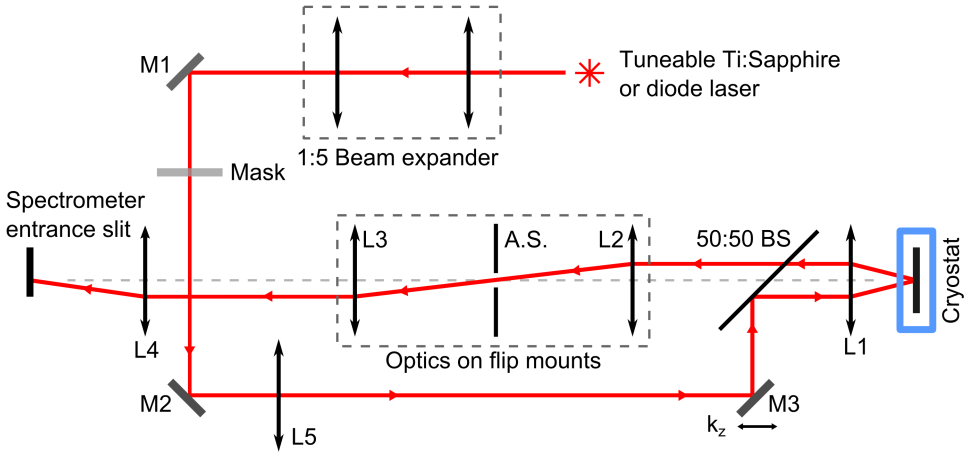

Figure 2.2: Schematic of the micro-photoluminescence setup used in the continuous-wave experiments consisting of lenses $L1$-$L5$, mirrors $M1$-$M3$, a 50:50 beam splitter (BS) and aperture stop (A.S.).

on a translational stage.

An image of the sample surface is formed at the aperture stop (A.S.). This was positioned to ensure that only emission from the output grating was collected. This spatially filtered image was then projected onto the entrance slit of the spectrometer. Alternatively, elements L3 and A.S. could be removed to record the angular dependence of the emission as described in Section 2.1.

In Chapter 4 amplitude- or phase-masks were placed in the pump beam in order to excite dark solitons. The phase mask consisted of a film of silicon nitride deposited on a microscope cover slide which introduced a π-phase delay to a portion of the beam. The amplitude mask consisted of a wire approximately 100 µm in diameter introduced into the beam. L5 was used in conjunction with the objective lens, L1 to project an image of this mask onto the sample surface.

The power of the out-coupled light from the waveguide was measured using a commercially available silicon photodiode-based power meter placed directly behind the A.S. The power meter was factory-calibrated and was compensated for its wavelength dependence. Losses due to the optics in the apparatus was accounted for by measuring the transmitted power through each element in isolation.

2.3 Interferometry

In Chapter 4 interference measurements were used in the CW experiments to recover the phase of the emission at the output of the waveguide. This section details the experimental setup and the techniques used in processing the interference patterns to retrieve phase maps. A good text is on this subject is *Holographic Interferometry* by P. K. Rastogi (editor) [107].

2.3.1 Off-axis holography

Off-axis holography is a technique in which a signal with an unknown phase is combined with reference resulting in interference fringes, the distribution of which is a function of the angle between the two beams and their relative phases. Analysis of these fringes therefore allows access to the underlying phase of the signal.

A schematic of the experimental setup used is shown in Figure 2.3. In the setup a portion of the pump beam is combined with the emission signal at the aperture stop of the spatial filter. The addition of lens L6 in combination of L2 provides an additional magnification of the reference beam affording approximately constant intensity across the aperture stop. The resulting interference pattern at the aperture stop is then imaged onto the entrance slit of a single-grating spectrometer and recorded on a CCD camera.

The origin of the intensity fringes can be illustrated by writing the signal as:

$$s(x,z) = |s(x,z)|e^{-i\phi(x,z)} \tag{2.2}$$

where $|s(x,z)|$ describes the spatial variation in intensity of the signal and $\phi(x,z)$ describes the variation in phase. Again we follow the convention that the direction of propagation is along the z-direction. The reference beam is then assumed to have a constant intensity and a variation in phase given by the angle of the beam:

$$r(x,z) = re^{i2\pi\xi z} \tag{2.3}$$

in which $\xi = sin(\theta)/\lambda$, where θ is the angle between the beams in the y-z-plane

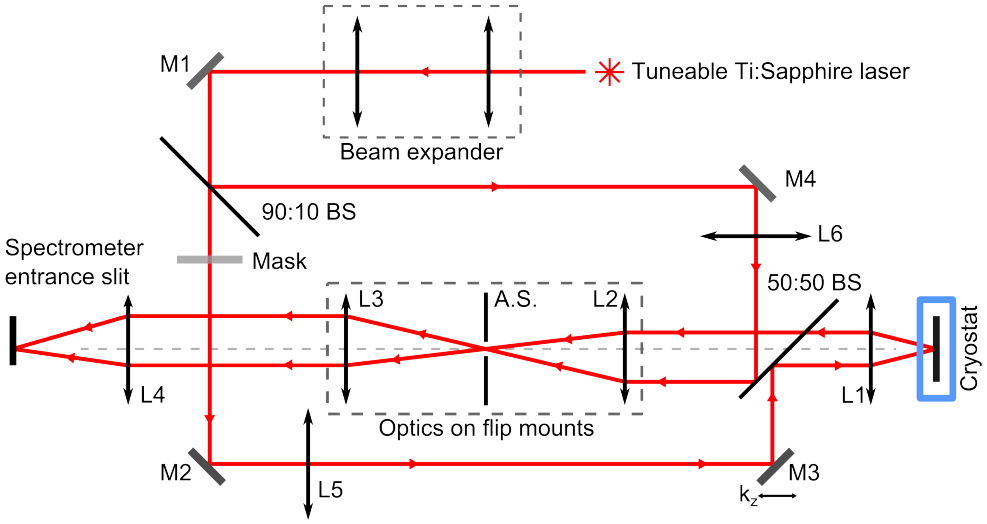

Figure 2.3: Schematic of the experimental setup used for the interferometric measurements consisting of lenses $L1$-$L6$, mirrors $M1$-$M4$, beam splitters (BS) and an aperture stop (A.S.).

and λ is the wavelength. The resulting intensity at the image plane is then:

$$\begin{aligned} I(x,z) &= |r(x,z) + s(x,z)|^2 \\ &= |re^{i2\pi\xi z} + |s(x,z)|e^{-i\phi(x,z)}|^2 \\ &= |r^2 + |s(x,z)|^2 + r|s(x,z)|e^{-i2\pi\xi z}e^{-i\phi(x,z)} + r|s(x,z)|e^{i2\pi\xi z}e^{i\phi(x,z)} \quad (2.4) \\ &= r^2 + |s(x,z)|^2 + 2r|s(x,z)|cos(2\pi\xi z + \phi(x,z)) \quad (2.5) \end{aligned}$$

From Equation 2.5 we see that the intensity at the image plane varies cosinusoidally along the z-direction with a period dictated by the angle of reference beam, modulated by the phase of the signal. An example of such an interferogram is shown in Figure 2.4a. The phase of the signal processes rapidly as polaritons propagate along the waveguide. Consequently the angle (θ) formed by the signal and reference beams only needs to be 1-2° to achieve a good contrast on the CCD camera.

2.3.2 Fourier-transform evaluation of interferograms

Fourier-transform evaluation using spatial heterodyning is a method which allows the evaluation of a single interferogram to recover the underlying phase of the signal. The technique can be illustrated first rewriting Equation 2.4 as:

$$I(x,z) = a(x,z) + c(x,z)e^{i2\pi\xi x} + c^*(x,z)e^{-i2\pi\xi x} \quad (2.6)$$

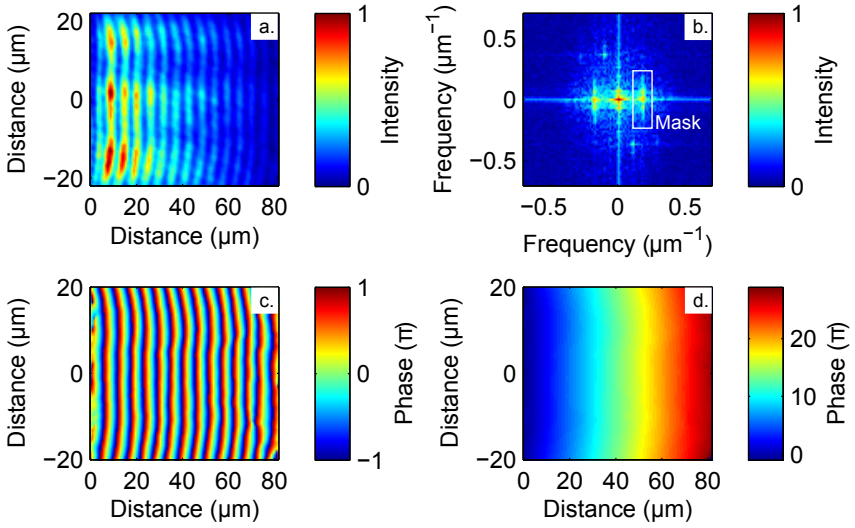

Figure 2.4: Evaluation of a two-dimensional interferogram. The recorded interferogram (a) is transformed using the fast Fourier transform algorithm and filtered (b). The inverse transform then yields a complex image with phase modulo 2π (c) which is then 'unwrapped' to recover the underlying signal phase (d).

where $a(x,z) = r^2 + |s(x,z)|^2$, $c(x,z) = \frac{1}{2}r|s(x,z)|e^{i\phi(x,z)}$ and $c^*(x,z)$ denotes its complex conjugate. Performing the Fourier transform then yields:

$$\mathcal{I}(v) = \mathcal{A}(u,v) + \mathcal{C}(u,v)\delta(u - 2\pi\xi, v) + \mathcal{C}^*(u,v)\delta(u + 2\pi\xi, v) \tag{2.7}$$

where u and v is the spatial frequency in x and z, and $\mathcal{A}$ and $\mathcal{C}$ are the Fourier transforms of the functions of a and c respectively. In practice this is done by performing the fast-Fourier transform (FFT) algorithm on a computer. An example of the transformed interferogram is shown in Figure 2.4b.

From Equation 2.7 is clear that the Fourier transform of the interference pattern has a near zero-frequency component and terms at $\pm 2\pi\xi$ which contain all the information of the signal. By filtering out all but one of these high frequency terms and taking the inverse Fourier transform we obtain the complex function $c(z)$. The phase of the signal is then:

$$\phi(x,z) = tan^{-1}\left(\frac{Im\ c(x,z)}{Re\ c(x,z)}\right) \tag{2.8}$$

The recovered phase of the interferogram is shown in Figure 2.4c which shows the precession in phase as polaritons travel along the waveguide.

2.3.3 Phase unwrapping

The phase obtained from Equation 2.8 is modulo 2π. A final problem therefore remains to add or subtract multiples of 2π in order to obtain a smooth phase map. This phase *unwrapping* can be achieved by following rows of pixels through the image and correcting the phase at the discontinuities where the phase difference between adjacent pixels is approximately 2π. However this tends to propagate errors in the phase throughout the image as the phase is unwrapped. More complicated *path-independent* algorithms exist which can be guided by the quality of the phase map achieved. The implementation of such an algorithm is beyond the scope of this work and therefore a freely distributed MATLAB® realisation[1] by Bruce Spottiswoode was used. The performance of this script was verified by comparing against the phase maps produced by unwrapping in a simple raster scan. Figure 2.4d shows the unwapped phase map recovered from the interferogram.

2.4 Time-resolved experiments

The experimental setup for the time resolved experiments in Chapter 5 is shown in Figure 2.5. Excitation was provided by a tuneable pulsed Ti:Sapphire (Spectra Physics Tsunami®) laser producing $\sim$100 fs duration pulses at a repetition rate of 82 MHz. This was used in conjunction with pulse shaping optics to control the spectral-width and center wavelength of the pulses. The output power from the waveguide was again measured using a power meter place directly behind A.S and accounting for losses on the intermediate optics. The emission projected onto the entrance slit of the spectrometer was either dispersed onto a CCD camera or directed onto the entrance slit of a streak camera.

The operating principle of the streak camera is illustrated in Figure 2.6. Photons incident on the entrance slit are focused onto the photocathode where they are converted into electrons which are accelerated through the streak tube. These electrons

[1] http://www.mathworks.co.uk/matlabcentral/fileexchange/22504-2d-phase-unwrapping-algorithms

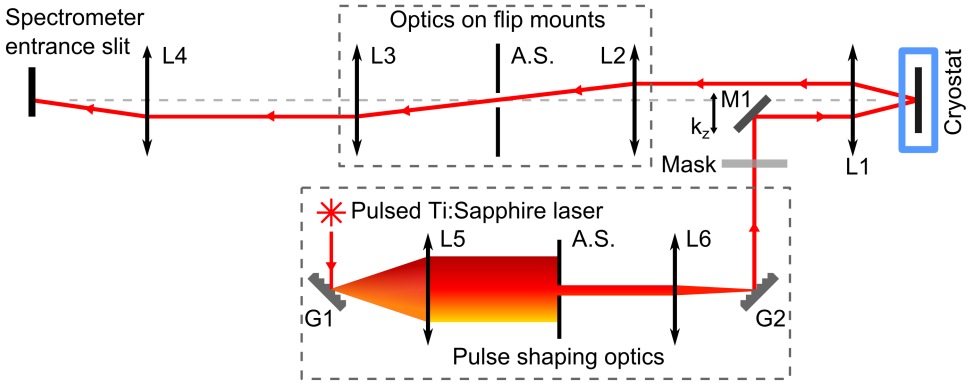

Figure 2.5: Schematic of the micro-photoluminescence setup used in the time-resolved experiments. In the pulse-shaping optics the ∼100 fs pulses from the laser were dispersed using a diffraction grating (G1) and filtered before being recombined on a second grating (G2). Here the different colours represent different wavelengths.

are accelerated towards the micro-channel plate which multiplies their number before bombarding a phosphor screen whereupon they are converted back to photons and detected on a CCD camera. The voltage across the sweep electrode is swept such that the electrons corresponding to successive photons are deflected by different amounts, resulting in a two dimensional streak image in which the vertical axis gives to the time of arrival. The voltage sweep is synchronised with the repetition rate of the laser so that the image may be integrated over many pulses.

The polariton time of flight was measured by projecting the Fourier transform of the emission onto the entrance slit of the streak camera. The horizontal entrance slit therefore selects a particular emission angle, corresponding to a particular in-plane wavenumbers along the z-direction. By displacing the lens in front of the spectrometer the wavenumber projected onto the entrance slit may be scanned. The time of flight is then the time between the laser reflection from the sample surface and the polariton emission from the output.

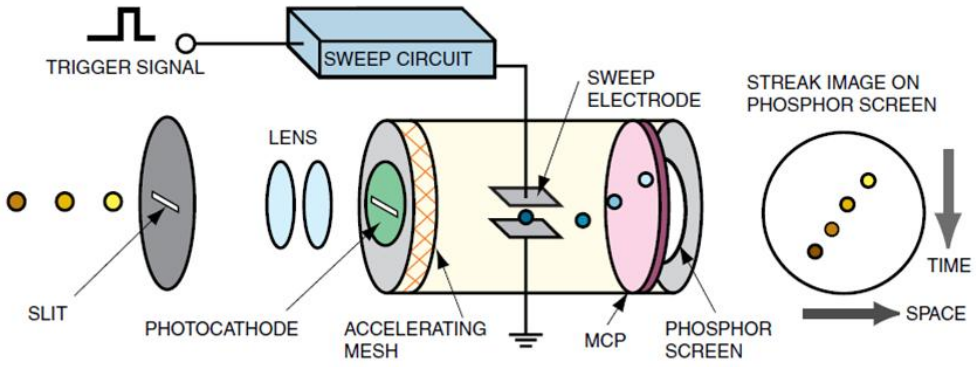

Figure 2.6: Operating principle of the streak camera tube. Taken from *Guide to Streak Cameras*, Hamamatsu

Chapter 3

Strong coupling in semiconductor waveguides

This chapter describes the first direct observation of strong coupling in semiconductor waveguides, the optimisation of the waveguide guide device used in the following chapters and the observation of the strong coupling regime up to 100 K. The results of Section 3.1 were reported in Applied Physics Letters in 2013 [108].

3.1 Waveguide polaritons

The device under test consisted of a 135 nm thick GaAs-based waveguide clad in $Al_{0.9}Ga_{0.1}As$ and SiN_x containing a single 10 nm $In_{0.04}Ga_{0.96}As$ QW. Several iterations of growth and PL characterisation were conducted to optimise the exciton linewidth of the QWs. Figure 3.1a shows a schematic of the waveguide device. The device was grown by MBE at the University of Cambridge and capped with a 200 nm thick layer of polycrysaline SiN_x grown by chemical vapour deposition (CVD). The MBE grown structure is as follows: 500 nm cladding layer of $Al_{0.9}Ga_{0.1}As$; 45 nm of GaAs; a 10 nm thick $In_{0.04}Ga_{0.96}As$ QW; 57 nm of GaAs; a 3 nm $Al_{0.9}Ga_{0.1}As$ etch stop layer and a final 20 nm GaAs cap. 100×100 µm grating couplers were etched to a depth of 160 nm into the SiN_x layer using electron beam lithography and reactive ion etching. The 250 nm grating period was chosen to scatter light in

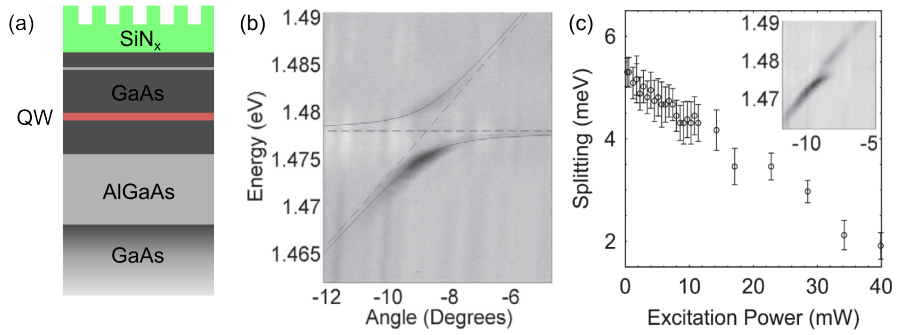

Figure 3.1: Schematic of waveguide device under test (a) not shown to scale. Angle-resolved spectrum of PL emission collected from grating (b). Here the exciton line has been subtracted in post-processing. Power dependence of the Rabi splitting between the upper and lower polariton branches (c) and angle-resolved spectrum at high power (inset). Panels (b) and (c) taken from Walker *et al*, 2013 [108].

vicinity of the anti-crossing out of the waveguide at $\theta = \pm 9°$.

The sample was placed in an optical cryostat held at 5 K. Excitation was provided by a tunable CW Ti:Sapphire laser emitting at 780 nm - well above the GaAs band gap - focused to a 60 µm diameter spot FWHM. The emission was collected from the grating etched into the SiN_x cladding layer and the Fourier transform imaged onto the entrance slit of the spectrometer. Figure 3.1b shows the angle-resolved PL emission spectrum from the waveguide at low excitation power (250 µW) showing the clear anti-crossing behaviour of the upper- and lower-polariton branches indicative of the strong-coupling regime. The dispersion shown in Figure 3.1b is mirrored around $\theta = 0°$, either arm corresponding to polaritons travelling in either direction parallel to the z-axis. In the image the background exciton line was subtracted in post-processing, the energy of which is indicated in the spectrum by a dashed line.

With increasing excitation power the observed Rabi splitting reduces, as shown inset in Figure 3.1c where at high power the anti-crossing behaviour is greatly diminished. This dependence of the Rabi splitting with power was extracted by fitting a two-coupled oscillator model to the observed dispersion. (The details of this fitting procedure are described in Appendix A). The extracted Rabi splitting versus excitation power is shown in Figure 3.1c. This reduction in Rabi splitting with excitation power is due to the reduction in exciton oscillator strength as a result of screening

by the increasing number of free carriers created at the pump spot [109].

Figure 3.2a shows the polariton dispersion with the pump spot 480 μm away from the grating coupler. Here the UPB, and polaritons in the LPB within 2.5 meV below the exciton line are strongly attenuated due to absorption by the exciton. In this case only the arm of the LPB at negative emission angles is present. Similarly when the pump spot was positioned on the opposite side of the grating only the arm of the LPB at positive angle was present. This confirms that polaritons are travelling from the pump spot to the grating whereupon they are detected, rather than excitons diffusing from the pump spot before recombining which would emit into all wavenumbers and populate the polariton branch at positive emission angles.

In the case where the pump spot and detection grating are spatially separate the effect of free-carrier screening and the subsequent reduction in Rabi splitting is negated. From fitting the Rabi-splitting was found to be 5.9 ± 0.6 meV which compares favourably with 5 meV reported in a semiconductor microcavities containing three QWs of similar composition [14]. The group velocity of the bare photon mode was found to be 48 ± 2 μm ps^{-1}. On resonance ($\Delta = 0$) this yields a polariton group velocity of 26 ± 2 μm ps^{-1} which is an order of magnitude greater than that found in microcavities [97, 105].

As the finite size of the grating coupler introduces uncertainty in the measurement of both momentum and energy of the LPB it is not possible to directly measure the linewidth in order to determine the polariton lifetime. Instead by moving the pump spot relative to grating the decay in intensity can be extracted from the LPB as shown in Figure 3.2b-c. From this propagation length the lifetime can be deduced using the group velocity determined from the dispersion. The deduced lifetime is shown in Figure 3.2d. At large detuning the lifetime of the predominantly photon-like polaritons is 8.5 ps. The lifetime increases near resonance to 11.4 s before reaching tail of the exciton line where the lifetime is reduced due to absorption. An exponential decay of 11.4 ps corresponds to a Lorentzian line shape with a FWHM of 115 μeV. Whilst this lifetime is comparable to that in microcavities it should be noted that because of the much larger group velocity waveguide polaritons propa-

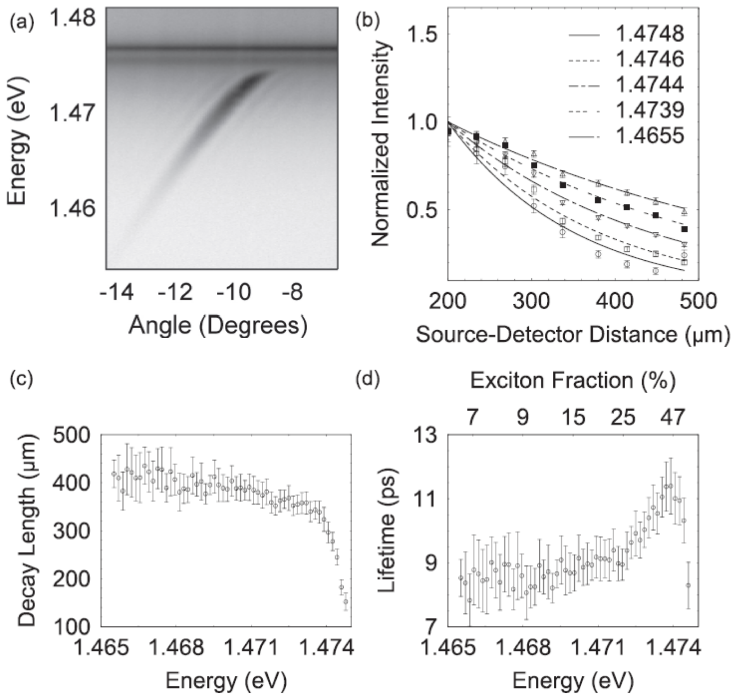

Figure 3.2: Angle-resolved PL spectrum after propagation plotted on a logarithmic grey scale (a). Extracted intensity versus position of the pump spot (b) for several photon energies showing fitted exponential decay. Polariton propagation length versus photon energy (c) and deduced lifetime (d). Images taken from Walker *et al*, 2013 [108].

gate much further within their lifetime. This makes them potentially more suited to applications involving the transmission of information.

Such an increase in polariton lifetime close to resonance has also been observed in microcavities and is attributed to a motional narrowing effect where the increased size of the polariton wavefunction results in a greater spatial averaging of the QW potential arising from fluctuation in alloy or layer thickness. This effect was not predicted in the work of Beggs *et al* [65] where the linewidth was calculated to vary between that of the uncoupled exciton and photon modes. Their approach however was based classical approach using non-local dielectric response theory which cannot reproduce this quantum mechanical effect.

3.2 Waveguide optimisation

In Section 3.1 it was shown that polaritons decay exponentially during propagation. For small Δ where polaritons are predominantly exciton-like ($|X|^2 \sim 1$) this occurs

Table 3.1: Summary of second generation waveguide devices detailing the number and composition of the QWs and the fraction of Al in the guide layer. All devices consisted of an $Al_xGa_{1-x}As$-based waveguide containing one or more 10 nm $In_yGa_{1-y}As$ QWs

Device No.	Wafer No.	No. QWs	In Frac. (%)	Al Frac. (%)
1	W0888	1	3.75	0
2	W0889	1	6	0
3	W0890	3	3.75	0
4	W0891	1	3.75	10

due to the increased absorption in the tail of the exciton line, and potentially by impurities close to the GaAs band edge. Whilst for large Δ where ($|C|^2 \sim 1$) this occurs due to photonic losses such as those attributed to roughness within the guide, or coupling to leaky waveguide modes. For future experiments and potential applications in this waveguide scheme it is important that the dominant source of these losses is identified and reduced as far as possible. To this end four different designs of waveguide were compared under the same conditions; the details of which are summarised in Table 3.1.

Nominally Sample 1 is a repeat growth of that used in Section 3.1; sample 2 has an increased fraction of indium in the QW which shifts the exciton line, and thus operating point to lower energy; sample 3 contains three QWs and thus is expected to show an increased coupling between the exciton and photon; and finally aluminium has been added to the guide layer of sample 4 to closer match the lattice constant of the cladding and reduce strain. For each device the period of the grating couplers was adjusted to ensure that the both arms of the LPB lay within the detectable range of angle of the system.

3.2.1 Polariton dispersion

Optical characterisation of the waveguide devices was performed at 5 K in an optical cryostat with CW non-resonant excitation provided by a laser diode emitting at 685 nm focused to a 50 µm diameter spot FWHM. The pump power was adjusted such that the power density ($\sim$ 0.1 kW cm^{-2}) was sufficiently low as to avoid

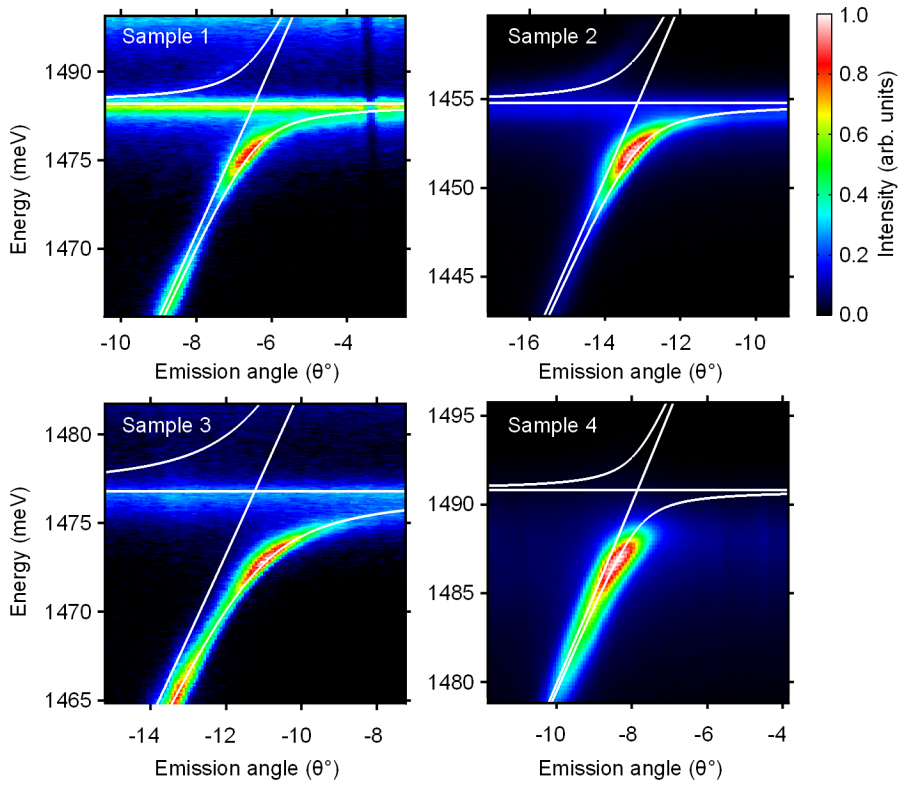

Figure 3.3: Angle-resolved spectra of the TE-polarised PL emission from each waveguide design showing fitted polariton dispersion and deduced uncoupled exciton and photon modes. All panels have been normalised individually and share a colour scale.

broadening of the exciton line and thus any reduction in the Rabi splitting. A Glan-Thompson linear polariser was use to select the TE-polarised PL emission from 1 mm gratings etched into the surface of the waveguide device. The exciton emission, being unpolarised is therefore suppressed relative to the strongly polarised polariton mode yielding an increased signal to noise ratio. The Fourier transform of the emission was then imaged on the entrance slit of the spectrometer to yield an angle-resolved spectrum.

Figure 3.3 shows angle-resolved spectra of the TE-polarised PL emission from each waveguide design. For each waveguide design a clear anti-crossing behaviour of the LPB with the exciton- and photon-modes can be seen indicating the strong-coupling regime. The characteristic waveguide parameters were obtained by extracting the position of the LPB in energy-momentum space and fitting to a two coupled-oscillator model (see Appendix A). The fitted model is shown overlaid in

Table 3.2: Summary of parameters extracted from fitting to a two coupled-oscillator mode detailing the exciton energy (E_x) the Rabi splitting (Ω) and group velocity of the bare photonic mode (v_g^c).

Device No.	Wafer No.	E_x (eV)	Ω (meV)	v_g^c (μm ps^{-1})
1	W0888	1.4782	5.3 ± 0.3	57.4 ± 0.8
2	W0889	1.4548	5.39 ± 0.07	62.4 ± 0.3
3	W0890	1.4768	9.37 ± 0.09	57.7 ± 0.7
4	W0891	1.4908	4.4 ± 0.1	61.5 ± 0.4

each panels and the parameters summarised in Table 3.2.

Samples 1 and 3 contain nominally identical 3.75 % $In_xGa_{1-x}As$ QWs. From the fitted parameters the increase in Rabi splitting with the number of QWs is in agreement with the relationship $\Omega \propto \sqrt{N_{QW}}$ as observed in semiconductor microcavities [110].

In sample 2 the increased indium fraction in the QW has resulted in shifting the exciton line to a lower energy whilst maintaining a similar Rabi splitting to that in sample 1. Similarly the addition of aluminium to the guide layer in sample 4 has shifted the exciton line to a slightly higher energy whilst maintaining a similar Rabi splitting. However the exciton lineshape in this sample is strongly asymmetric with a long tail at the low energy side resulting in strong absorption which limits the approach of the LPB towards the exciton line in Figure 3.3d.

3.2.2 Propagation length

The propagation length for each device was measured by moving the pump spot relative to one 150×200 μm grating etched into the surface of the waveguide and using spatial filtering to ensure only the emission from this grating was collected. An angle-resolved spectrum was recorded at each pump spot position and the intensity extracted as a function of detuning. An exponential function was then fitted to the decay in emission intensity with distance at each detuning to obtain the characteristic propagation length.

Figure 3.4 shows the measured propagation length of polaritons in the LPB for

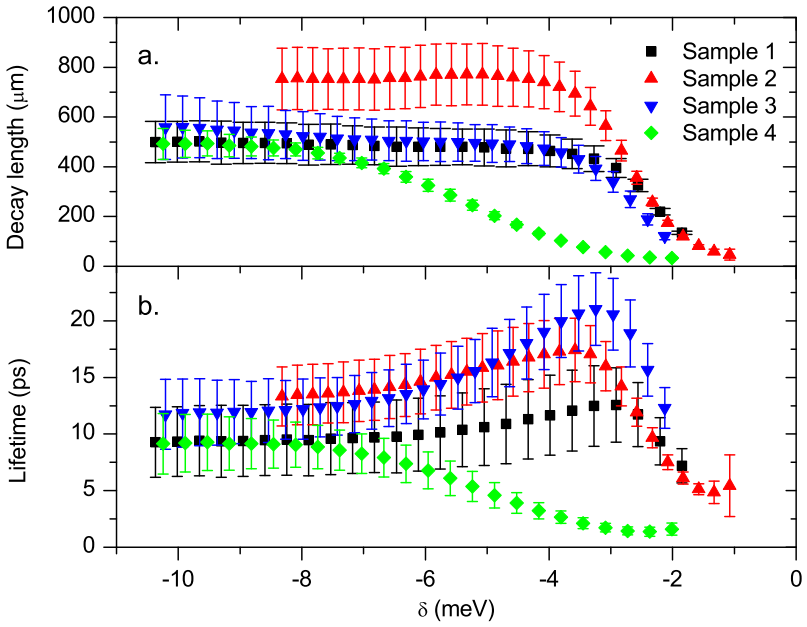

Figure 3.4: Decay length of polaritons (a) and deduced polariton lifetime (b) versus detuning (δ) relative to exciton line for each waveguide design.

each waveguide device plotted against the detuning (δ) from the exciton and the lifetime deduced from the group velocity extracted in Section 3.2.1. For each sample the propagation length is approximately constant at large δ and reduces towards zero with proximity to the exciton line. At large δ polaritons are predominantly photonic and the propagation length reduces to that of the bare waveguide. Samples 1, 3 and 4 contain similar x = 3.75% $In_xGa_{1-x}As$ QWs and have operating wavelengths and thus similar propagation lengths of approximately 450 μm for photon-like polaritons, whilst the increased indium content of the QW in sample 2 shifts the operating point further away from the cut-off and thus increasing the propagation length of the bare waveguide to approximately 800 μm.

For small δ polaritons are exciton-like and travel at vanishingly small group velocities. Such polaritons therefore travel shorter distances within their lifetime. This effect is compounded by the increased absorption in the tail of the exciton line. From Figure 3.4 increased absorption near the exciton line due to the addition of aluminium to the guide layer in sample 4 as observed in the PL spectrum is born out in the reduced propagation length.

Noting the intensity of transmitted light falls-off exponentially the intensity at

the output is approximately constant in photon-like region where the propagation length is constant. Using this as a baseline, the usable bandwidth can be defined by the point at which the propagation length is such that the intensity at the end of the 600 μm waveguide is halved. For samples 1, 2 and 3 this occurs at the point where $\delta_{min} \approx 2.5$ meV, and $\delta_{min} \approx 5$ meV for sample 4. This minimum accessible detuning corresponds to the maximum exciton fraction ($|X|^2$) as given by Equation 1.11. For samples 1 and 2 the maximum accessible exciton fraction is $|X|^2 \approx 0.53$ and 0.54 respectively whilst in sample 3 the increased Rabi splitting increases the accessible exciton fraction to $|X|^2 = 0.78$. Finally the increased absorption near the exciton line in sample 4 reduces the accessible exciton fraction to $|X|^2 = 0.16$.

By this metric sample 3 is the most suitable of this second generation of devices for soliton studies. The increased Rabi splitting affords a greater GVD (from Equation 1.13) and allows access to greater exciton fractions and thus to greater nonlinearities. Furthermore this increased exciton fraction at a particular detuning implies a lower group velocity (from Equation 1.12) and therefore an increased polariton lifetime, born out in the deduced polariton lifetime in Figure 3.4b.

Notably whilst the exciton fraction for a given detuning is greater - and thus the group velocity lower - in sample 3 than sample 1 the roll-off in propagation length is similar. This suggests that absorption in the exciton tail, even in these state-of-the-art QWs, is the dominant effect limiting the propagation length at small detunings.

3.3 Temperature dependence of polaritons

Shortly after the first observation of polartons in microcavities it was shown by Houdré *et al* [111] using an AlGaAs/GaAs-based microcavity device containing $In_{0.13}Ga_{0.87}As$ QWs that the strong coupling regime can persist up to room temperature. Recently nonlinear polariton phenomena have been observed in GaN-based devices at room temperature [112, 20]. Technologically this is an important point as even using liquid nitrogen (77 K) as a coolant instead of liquid helium (4.2 K)

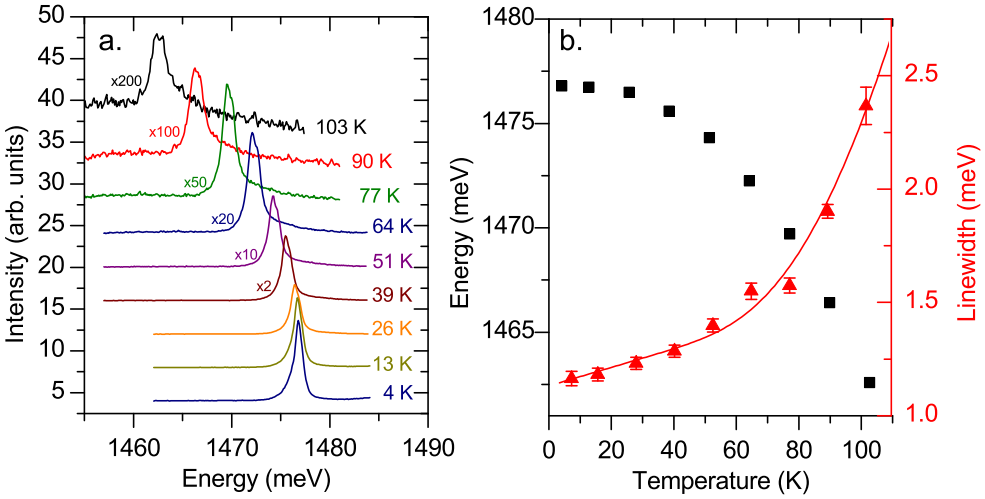

Figure 3.5: Temperature dependence of the exciton PL emission. Exciton spectra at temperatures between 4 and 100 K at low excitation power (a) and extracted central energy and linewidth versus temperature (b).

significantly reduces the cost of operating the device potentially allowing for wider adoption.

For the purpose of this demonstration sample 3 was chosen as from Equation 1.9 the larger the Rabi-splitting at low temperature means that a larger exciton linewidth can be tolerated before quenching of the strong coupling regime. The sample was once again placed in a helium-flow cold-finger cryostat. The sample temperature was raised up from the base temperature of the cryostat by control of the helium flow-rate and was stabilised to within one degree using a PID controller. Non-resonant excitation was provided by a tunable Ti:Sapphire laser tuned to 40 meV above the GaAs band edge. The laser was focused to a 30 μm spot on the sample surface and the power density (0.3 W cm^{-2}) was chosen to be sufficiently low as to avoid broadening of the exciton line.

Figure 3.5 shows the excitonic PL emission observed away from the grating region at low excitation power and the extracted central energy and linewidth at various temperatures. With increasing temperature the central energy of the emission shifts towards lower energy, broadens and reduces in intensity, becoming 200 times weaker by 100 K than at 4 K.

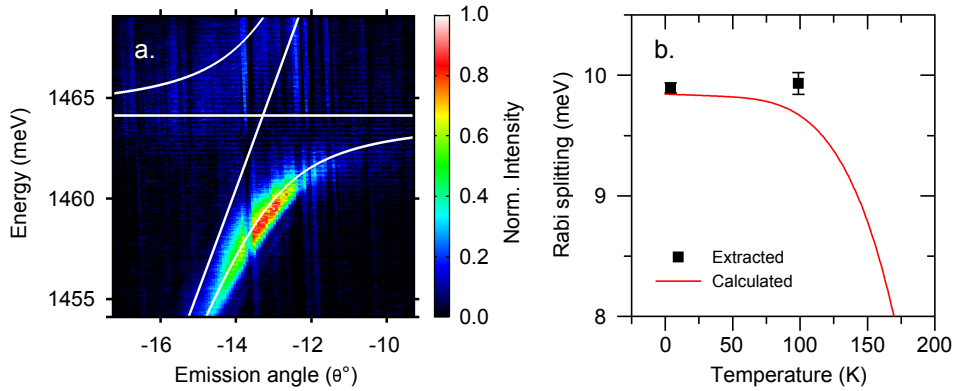

Figure 3.6: Angle-resolved spectrum of PL emission at 100 K (a) and plot of calculated Rabi splitting versus temperature and that extracted from spectra.

The dependence of the central energy and linewidth of the emission was extracted by fitting of a single Gaussian distribution to the PL spectrum. Following the approach of Gammon *et al* [113] the temperature dependence of the exciton linewidth γ_X was then fitted using the formula:

$$\gamma_X(T) = \gamma_{inh} + \gamma_{AC}T + \frac{\gamma_{LO}}{e^{E_{LO}/k_BT} - 1} \tag{3.1}$$

where γ_{inh} is the inhomogeneous homogeneous linewidth; γ_{AC} describes the dependence due to coupling to acoustic phonons; k_B is the Boltzmann constant; E_{LO} is the energy of longitudinal optic (LO) phonons. As the QW contains only a small fraction of indium and is surrounded by a GaAs matrix the LO phonon energy was taken as 35 meV as used by Gammon *et al* for GaAs QWs [113]. From fitting $\gamma_{inh} = 1.15$ meV, $\gamma_{AC} = 3.9$ μeV and $\gamma_{LO} = 41$ meV.

Figure 3.6 shows angle-resolved spectrum of the emission collected from a 1 mm long grating on the sample at 100 K and the dependence of the Rabi splitting on temperature. In spectrum there is a clear anti-crossing behaviour indicative of the strong coupling regime. From the fitting proceedure using a two-coupled oscillator model (shown in white overlaid in Figure 3.6a) the Rabi splitting was found to be 9.90 ± 0.09 meV, equal to that observed at 4 K.

The dependence of the Rabi splitting can be predicted from Equation 1.9 by substitution in of Equation 3.1. The photon linewidth was calculated from the decay length $l_d = 500$ μm and group velocity $v_g^c = 57.7 \pm 0.7$ μm ps^{-1} by $\tau = l_d/v_g^c$.

This yields $\tau = 8.6$ ps, corresponding to Lorentzian 153 μeV FWHM. Figure 3.6b shows $\Omega(T) = \sqrt{\Omega(4\text{ K})^2 + (\gamma_X(T) + \gamma_C)^2}$ using the exciton linewidth from fitting in Figure 3.5b.

From the expression relating the Rabi splitting to the exciton linewidth the strong coupling regime is expected to be fully quenched at room temperature. However the intensity of the emission is already several orders of magnitude lower at 100 K than at 4 K which may make the integration times required to obtained a reasonable signal to noise ratio prohibitively long at higher temperatures.

3.4 Conclusion

In this chapter the first direct observation of polaritons in semiconductor waveguide was made by direct imaging of the characteristic anti-crossing in the dispersion. At low power the increased coupling between exciton and photon modes over microcavity structures was demonstrated. At high excitation powers it was shown that this anti-crossing behaviour can be quenched as a result of reduction in oscillator strength due to screening by free carriers created at the pump spot. By extracting the propagation length and group velocity of polaritons in the LPB a clear increase in lifetime near resonance was found attributed a motional narrowing effect.

By comparing four different sample designs it was found that moving the operating point of the device to longer wavelengths, away from cut-off increases the propagation length for photon-like polaritons. It was also found that increasing the number of QWs serves to increase the Rabi splitting as for microcavities. This effectively pushes the LPB further from the exciton line allowing access to the more excitonic part of the LPB where nonlinear effects are expected to be more pronounced. Future designs may therefore contain a greater number of QWs containing a greater indium fraction to exploit these findings.

Finally it was shown that in these devices the strong coupling regime can persist up to 100 K. This could potentially be exploited in future III-V polaritonic devices operating at liquid nitrogen temperatures or alternatively the scheme could be re-

produced in nitride-based or organic material systems for devices operating room temperature.

Chapter 4

CW experiments and dark spatial solitons

This chapter describes the results of continuous-wave (CW) measurements on waveguide polaritons. The first section describes the observation of a self-defocusing nonlinearity arising from polariton-polaritons interactions inherited from the exciton component which is then shown support the formation dark spatial solitons. Finally the nonlinear effects arising from polaritons are shown to persist up to 100 K.

4.1 Introduction

Dark solitons are solutions to the NLSE which, in the ideal case consists of dip in intensity on an bright background extending out to infinity. At the point of the dip in intensity, which will be referred to hereafter as a *dark notch*, the wavefunction of this ideal dark soliton undergoes an instantaneous phase jump of π. For a grey soliton the phase jump is less than π radians and is more gradual. Experimentally dark solitons can be excited by imprinting either this phase jump or the dip in intensity onto the input beam. In the absence of an optical nonlinearity or at low intensity the input beam simply diffracts. However in the soliton regime the shape of the dark notch does not change as it propagates and its size is dictated by the optical intensity and the strength of the nonlinearity.

Due to the equivalence in the NLSE dark solitons can be formed in either space or time. Spatially-dark solitons have been observed in a range of nonlinear systems such as photovoltaic- [88, 89] and photorefractive-crystals [90] and more recently in the superfluid flow inside a semiconductor microcavities [52].

As dark spatial solitons are supported in materials with negative nonlinear refractive indices the index within the dark notch is locally higher than in surrounding regions. Dark solitons have therefore been proposed as reconfigurable waveguides [91, 92], y-splitters [93] and multiport routers [94] which can be written by imprinting either a phase jump or dip in intensity onto a pump beam.

The aim of this chapter is to investigate the nonlinear properties of the waveguide polariton device, building upon the first observations of strong coupling in the previous chapter. To this end the formation of dark spatial solitons is used as a demonstrator of the hereto unobserved nonlinear properties of waveguide polaritons.

4.2 Resonant injection and self-defocusing

Sample 3 from Chapter 3 was placed in a continuous-flow helium cold-finger cryostat held at approximately 5 K, monitored using a factory-fitted and -calibrated sensor. The temperature could be raised above this base level through control of the helium flow and was stabilised by a heater attached to the cold-finger connected to a PID controller.

CW excitation was provided by a tunable Ti:Sapphire laser focused through a microscope objective to spot approximately 10 μm in diameter on the sample surface with angular spread of $\Delta k_\perp = 0.5\ \mu\mathrm{m}^{-1}$. Polaritons were excited in the waveguide by tuning the laser wavelength and incidence angle to be in resonance with part of the lower polariton branch. This is illustrated in Figure 4.1 which shows an angle-resolved PL spectrum collected under non-resonant excitation and tomographic image extracted at $\delta = -3.8$ meV indicating the size of the pump spot in momentum space.

Figure 4.2 shows real-space images of the pump spot and output beam at low

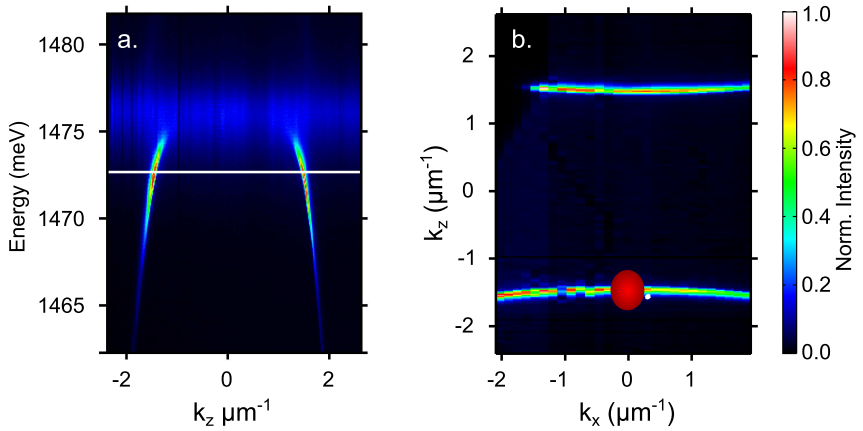

Figure 4.1: Angle-resolved PL spectrum of emission from a 1 mm long grating on the sample surface with non-resonant excitation showing the energy of the laser excitation (solid white line). Tomographic image of dispersion at $\delta = -3.8$ meV relative to the exciton line showing size of pump spot (red) in momentum space.

and high power. The pump spot was positioned at the edge of the grating to avoid polaritons leaking out before reaching the waveguide. Care was taken to ensure that the transverse component of the injected beam was negligible ($k_x = 0$) by adjusting the incidence angle such that the output beam arrived at the centre of the output grating at $x = 0$. The laser was tuned to $\delta = -5.6$ meV relative to the exciton line and the incidence angle fine-tuned to maximise the output signal. At low power the input beam diffracts, slightly increasing in width. At high power this natural diffraction is enhanced resulting in a dramatic increase in the width of the beam.

This behaviour was characterised by extracting the full width one-third of the maximum intensity (FWTM). This definition of beam width was used to avoid difficulty in extracting the width due to modulation in the beam profile. Figure 4.2d shows the extracted beam width versus incident power on the sample surface. At low power the beam width is approximately constant, the input beam (11.7 ± 0.06 μm FWTM[1]) diffracts to approximately 15 μm before increasing significantly above 1 mW of incident power.

Intuitively this nonlinearity can be explained as being the result of repulsive inter-particle interactions which tend to deflect polaritons from their trajectory along the

[1]For a Gaussian distribution FWTM = $\sqrt{\log_2 3}$FWHM.

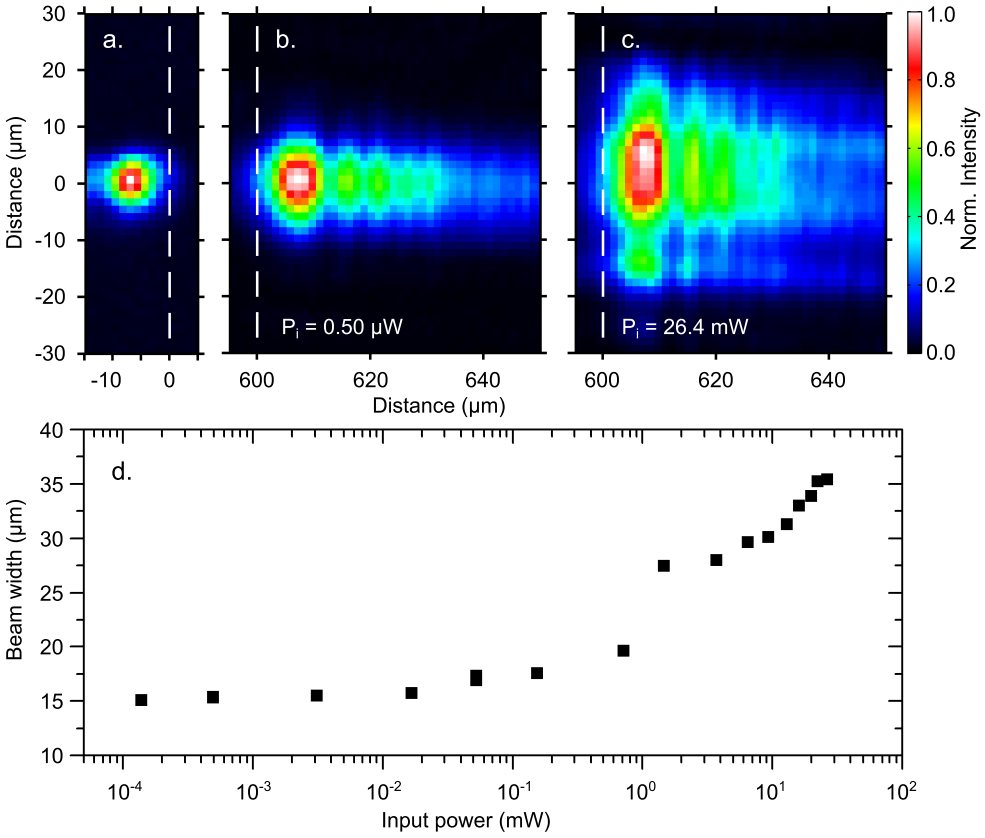

Figure 4.2: Psuedo-colour real-space images of the pump spot reflection at the input grating (a) and of the emission from the output grating at low (b) and high power (c). The approximate position of the edge of the diffraction gratings is indicated by dashed white lines. Extracted beam width at the output grating versus pump power (d).

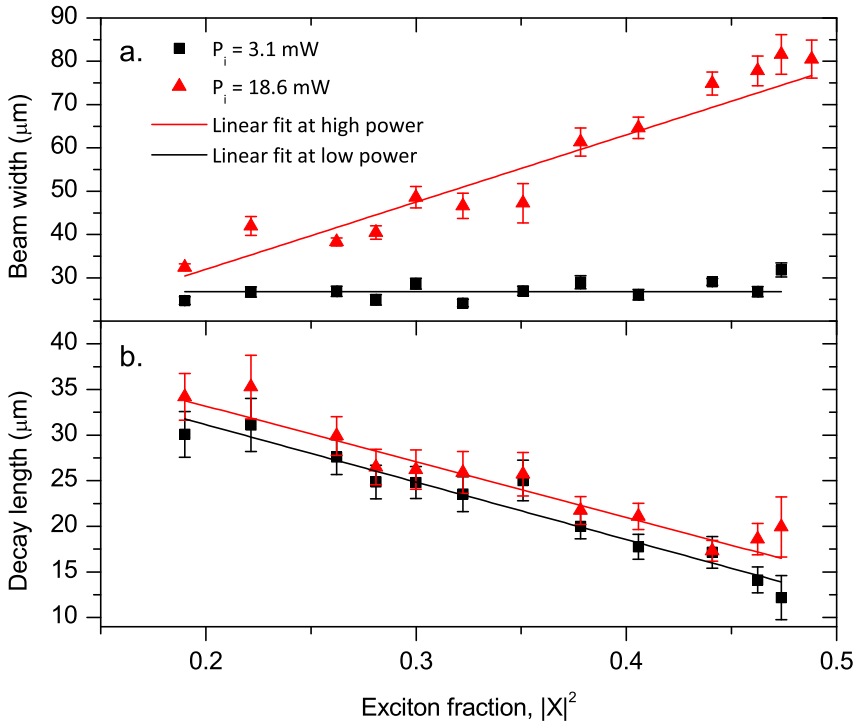

Figure 4.3: Extracted beam width (a) and decay length of PL emission at the output grating versus exciton fraction at low and high power (b). Panels share the same legend.

waveguide resulting in a spreading of the beam. As the particle density increases the effect of the interactions becomes more prominent. Equivalently however this can be described from a nonlinear optics perspective as a negative nonlinear refractive index.

To verify that this effect derives from the polariton-polariton interactions and not simply a nonlinear response of the waveguide itself, the size of the defocusing was extracted as a function of exciton fraction. Here the pump spot was 16.19 ± 0.06 μm FWTM in diameter. Figure 4.3 shows the beam width and decay length in the grating region at low and high power versus exciton fraction. At each detuning the incident power was kept constant and the coupling fine-tuned to maximising the emission intensity at the output. The scatter in the data here can be attributed to variations in the coupling efficiency which could be eliminated by instead comparing the spreading at the same output power.

At low power, where the particle density is sufficiently low that the effect of inter-particle interactions are negligible, the width of output beam is 26.8 ± 0.6 μm independent of photon fraction whilst at high power the output beam width decreases near-linearly with photon fraction. The increase in beam width at low power from Figure 4.2 is in approximate agreement with increase in diameter of the pump spot.

The linear dependence of beam width at high power can be understood by noting that the polariton interactions are inherited from the exciton parent species: the greater the exciton fraction, the larger the interaction strength and thus the larger the defocusing effect observed at the output. From Figure 4.3a this effect becomes negligible for exciton fractions below $|X|^2 = 0.2$ where the interactions between particles are too weak to produce a defocusing effect for this particle density. Similarly it can be expected that the defocusing effect is diminished at large exciton fractions where particle density is reduced due to the increased absorption .

A dependence of the output emission on the exciton fraction is also born-out in the decay length in the grating region. Figure 4.3b shows the decay length extracted by fitting an exponential function to the emission intensity at low and high excitation

power for various exciton fractions. By contrast to that observed in Section 3.2.2 the decay length in the grating region is significantly shorter than in the waveguide (approximately 460 μm) and decreases near linearly with exciton fraction over the range investigated.

The decay length is a product of the lifetime and group velocity. As the decay length is so dramatically foreshortened in the grating region and only the photonic part experiences the effect of the grating it is reasonable to neglect other contributions to the lifetime. Therefore in the grating region it should be expected that the decay length is the product of polariton group velocity ($v_g = v_g^c|C|^2$ from Equation 1.12) and the bare photon lifetime (τ_c) scaled by the photon fraction, i.e. $l_d \approx v_g^c|C|^2 \times \tau_c/|C|^2$. For the range of exciton fractions here, where motional narrowing and excitonic absorption are not expected to play a roll, it should be expected that the decay length is constant.

The cause for the dependence of the decay length in the grating region on the exciton fraction remains unclear. However it may be that the coupling strength of the grating - and therefore the photon lifetime in the grating region - is itself dependent on the photon fraction.

Taking the linear fit to the data shown in Figure 4.3 as a guide for eye the decay length is slightly longer at high power. Assuming that the photon lifetime is constant for a given exciton fraction this implies that the group index is reduced at high power which supports the description of the nonlinearity as a negative nonlinear refractive index.

4.3 Dark spatial solitons at 4 K

After verifying the existence of an optical nonlinearity deriving from polariton-polariton interactions attention is now turned to examining if this nonlinearity support the formation dark spatial solitons. In the experiment the laser was passed through either a phase or amplitude mask before being focused to a 30 μm diameter spot (FWHM) on the sample surface. The mask was imaged onto the sample

surface, producing either a 6 μm dark notch or π-phase jump to the centre of the beam. The laser was tuned to $\delta = -3.8$ meV corresponding to $|X|^2 = 0.60$. The power output of the waveguide was measured by focusing the emission from the output grating onto a commercially available photodiode-based power meter.

4.3.1 Generation of single dark solitons

Figure 4.4 shows pseudo-colour real-space images of the pump spot at the input grating and of the emission from the output grating at low and high pump power. The pump spot has an approximately Gaussian distribution with an intensity minimum at the point of the π-phase jump introduced by the mask (see Figure 4.4d). At all powers investigated the output beam has a characteristic shape consisting of two bright lobes with a dark notch at the centre. At low power the output beam width is comparable to that at the input whilst the dark notch is considerably wider. At high power the notch is only slightly wider than at the input whereas the full beam width is considerably larger.

This behaviour was characterised by extracting the output beam parameters versus pump power. The full beam beam width was once again defined by the full width at one-third of the maximum intensity. The notch width was defined as the full width between the half maximum points relative to the minimum intensity of the notch, i.e. by the points $I = (I_{max} + I_{notch})/2$. The blackness of the soliton was defined as the depth of the dark notch relative to the lobes, i.e. $(I_{max} - I_{notch})/I_{max}$. Figure 4.5 shows the extracted beam parameters at the output versus pump power. The error bars here are comparable to the size of the markers and have been omitted.

At low power the beam width and blackness of the dark notch are defined by the input profile and are approximately constant. With increasing power above 10 mW the beam width increases by 60 % whilst the dark notch narrows by 50 % relative to low power. Simultaneously the blackness of the soliton decreases from that dictated by the phase mask at the input (> 0.9) to that of the soliton (approximately 0.85 at saturation). From Equation 1.19 and 1.20 the blackness of a grey soliton on an infinite background is equal to $\cos^2(\phi)$ where $\pi - 2\phi$ is the total phase shift across

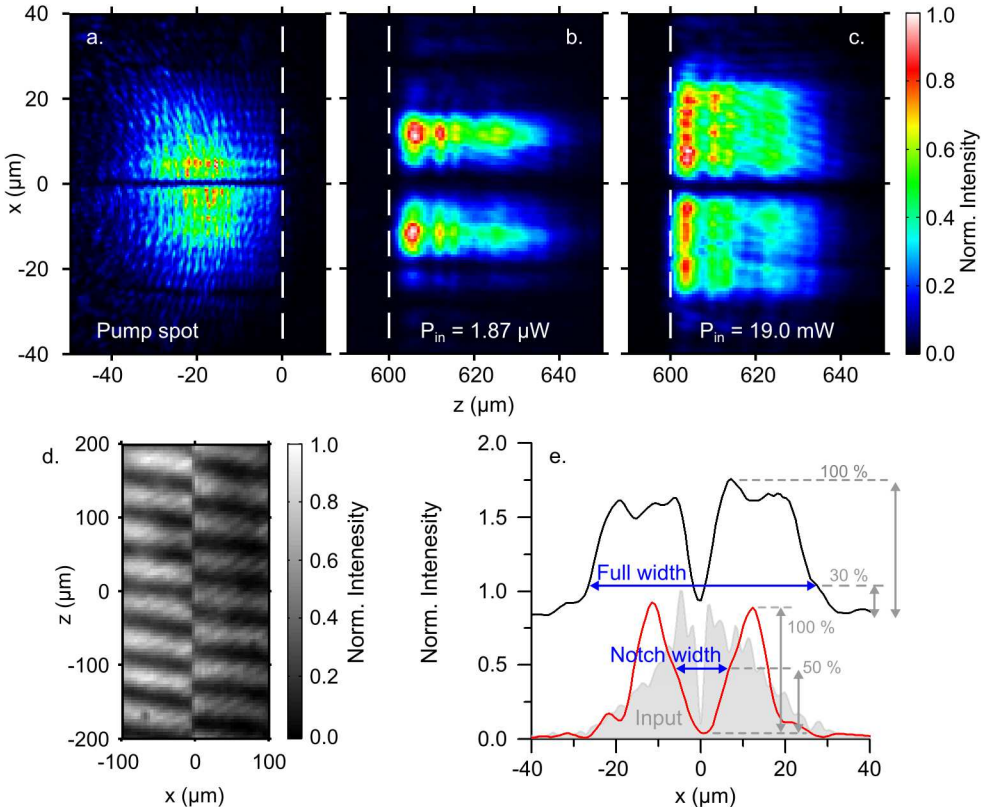

Figure 4.4: Pseudo-colour real-space image of the pump spot on the input grating (a) and emission from output grating at low (b) and high pump power (c). Panels a, b and c share the same colour scale. The edge of the input and output grating is indicated by a dashed white line. Interferogram of the mask placed in the pump beam showing π-phase jump (d). Extracted cross sections of the input and output beam taken from panels a to c showing defition of the full beam width and notch width (e).

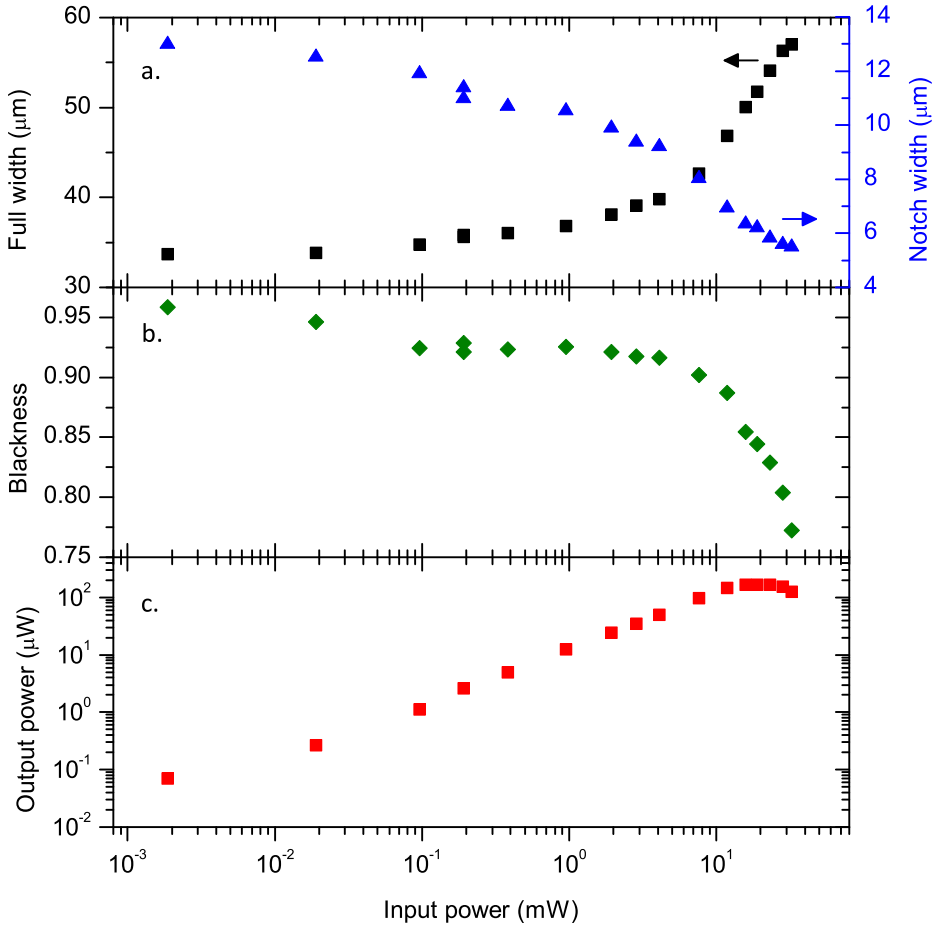

Figure 4.5: Characteristic widths of the beam at the output grating with phase mask versus pump power (a) showing full width (left) and notch width (right). Blackness of the dark notch (b) and output power versus input power (c).

the soliton. Given the observed blackness of 0.85 the total phase shift at the output is expected to be 0.75π radians.

In Figure 4.5c it can be seen that above 10 mW the output power saturates at 188 μW. Multiplying this output power by a factor of 4 determined by FDTD simulations to account for the power lost into the substrate yields the power inside the wavegude at the output grating. Taking the decay length at this detuning to be 460 μm from Section 3.2.2 the power at the input of the 600 μm-long waveguide can be estimated by further multiplying by exp(600/460) yielding an input power of 2.77 mW. Given this power and the photon energy (1.473 eV) at this detuning the exciton density at the input to the waveguide can be estimated from:

$$\rho = \frac{P}{E_{ph}} \frac{|X|^2}{N_{QW}} \frac{1}{\Delta x v_g} \tag{4.1}$$

where N_{QW} is the number of QWs, $\Delta x = 30$ μm is the FWHM of the beam and $v_g = 22.9 \pm 0.5$ μm ps^{-1} is the group velocity at this detuning. An input power of 2.77 mW therefore corresponds to an exciton density of $\rho = (3.4. \pm 0.1) \times 10^8$ cm^{-2} per QW, several orders of magnitude below the Mott density reported for similar QWs of between 10^{10} and 10^{11} cm^{-2} [114]. This suggests that the system remains in the strong coupling regime at high power and therefore the resulting nonlinearities are derived from the presence of polaritons. The saturation in the output power versus input power may instead be attributed to heating of the sample which results in a broadening of the exciton line and increased absorption.

Drawing an analogy with the solitons found in superfluids the healing length (ξ) can be related to the size of the soliton from Equation 1.26 by FWHM$= 2\sqrt{2}\ \tanh^{-1}\left(\sqrt{1/2}\right)\xi$. At saturation the FWHM of the soliton is 8 μm corresponding to a healing length of the fluid of $\xi = 3.2$ μm.

The healing length of the fluid is given by $\xi = \hbar/\sqrt{2mg|\psi_0|^2}$ where $|\psi_0|^2 = \rho_0$ is background particle density, m is the particle mass and g is the strength of their interactions. Assuming that the background density is approximately equal to the mean density inside the waveguide and making use of Equation 4.1 the particle density at the output of the waveguide is $\rho_0 = (9.3 \pm 0.3) \times 10^7$ cm^{-2}. Expanding

the polariton disperision in the transverse direction about $k_x = 0$ using Taylor series the effective mass is $m = \hbar\beta/v_g$. Using the expressions introduced in Section 1.3 the wavenumber can be deduced from the detuning to obtain $\beta = 23.4 \pm 0.8\ \mu\mathrm{m}^{-1}$. Substituting the resulting mass back into the expression and rearranging for the interaction strength yields $g = 34 \pm 3\ \mu\mathrm{eV}\ \mu\mathrm{m}^2$.

This estimation of the interaction strength is an order of magnitude greater than has been observed between polaritons in microcavities [14, 72]. The discrepancy can be attributed to interaction of polaritons with an exciton reservoir consisting of dark, localised and high-momentum exciton states which is constantly replenished by the scattering of polaritons into these states as has been observed in microcavities [115, 116]. As the repulsive interactions between polaritons are inherited from the exciton component the presence of this reservoir results in additional blueshift of the LPB which is manifested as an increased optical nonlinearity. Therefore the interaction strength extracted here contains a component relating to the interaction with the exciton reservoir in addition to the interactions between polaritons. The creation of this background reservoir could be avoided to measure the interaction strength between polaritons alone using pulsed excitation, provided that the time between pulses is longer than the lifetime of the exciton reservoir which is on the order of 50 ps [117].

4.3.2 Generation of dark soliton pairs

The phase mask used in the previous section was replaced by a 100 µm diameter wire imaged onto the sample surface to produce a dark notch in intensity of 6 µm at FHWM on the sample surface. Figure 4.6 shows pseudo-colour real-space images of the pump spot on the input grating and emission from the output grating. At low power the well-defined dark notch is washed-out, leaving an increase in intensity at the centre analogous to Arago's spot arising from Fresnel diffraction around an obstacle [118]. Once again at high power the total beam width increases but the single dark notch at the input now forms two at the output.

This behaviour was characterised by extracting beam parameters versus pump

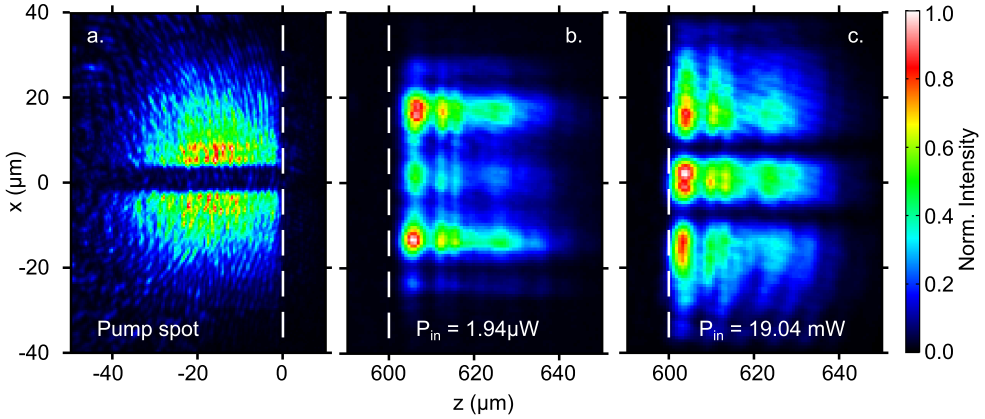

Figure 4.6: Pseudo-colour images of the pump spot on the input grating (a) and emission from the output grating at low (b) and high pump power (c). The edge of the grating couplers are indicated by a dashed white line. All panels share a colour scale.

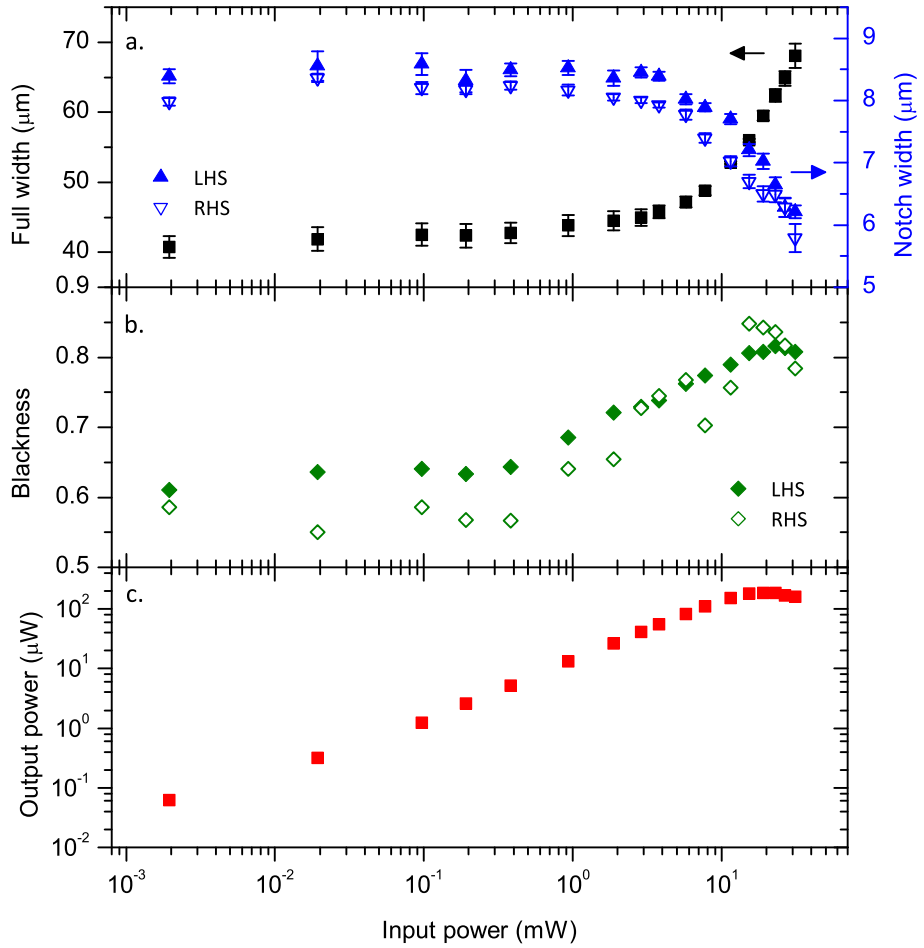

Figure 4.7: Characteristic widths of the beam at the output grating with amplitude mask versus pump power (a) showing full width (left) and notch width (right). Width of the LHS and RHS notch is shown in closed and open markers respectively. Blackness of the notches on the LHS and RHS (b) and output power versus input power (c).

power using the same definitions described in Section 4.3.1. Figure 4.7 shows the extracted beam widths and blackness of either soliton, and the total output power versus pump power. At low excitation powers the profile of the beam at the output is approximately constant and the full width comparable to that at the input. Above a threshold of 10 mW the total beam width increases by 50 % whilst the width of notches reduces by 40 %, both notches reproducing the behaviour observed of single dark solitons in Section 4.3.1. The blackness of these dark notches increases by a third at high power approaching a value of 0.8, approximately equal to that for the single dark soliton before the linearity between input and output power saturates. This behaviour is therefore indicative of the formation of a pair of dark spatial solitons.

4.3.3 Interference measurements

From its mathematical definition, the *smoking gun* of a dark soliton formation can be considered as the development of a phase shift across the dark notch in intensity. To observe this a Mach-Zehnder interferometer was constructed to interfere the output of the waveguide with a small portion of the pump beam to produce an interference pattern on the entrance slit of the spectrometer. (See Section 2.3.) The underlying phase of the emission was recovered from the interference pattern using Fourier transform interferometry.

Figure 4.8 shows real-space images of the PL emission intensity and recovered phase from interference patterns recorded at low and high power when using the π-phase mask to excite a single dark soliton. From Figure 4.8c the phase precesses linearly as polaritons propagate along the z-axis. This linear dependence was subtracted from the images (panels b and e) to highlight the change in phase in the transverse direction near $x = 0$. In both cases there is a phase change approaching $\pi/2$ at the point of the intensity minimum suggesting a grey soliton.

From the linear fit to the data shown in Figure 4.8c the phase extracted from the intensity precesses at 0.170 $\mu\mathrm{m}^{-1}$ in the z-direction. As both the signal and reference beams which interfere at the image plane are nearly parallel, this precession

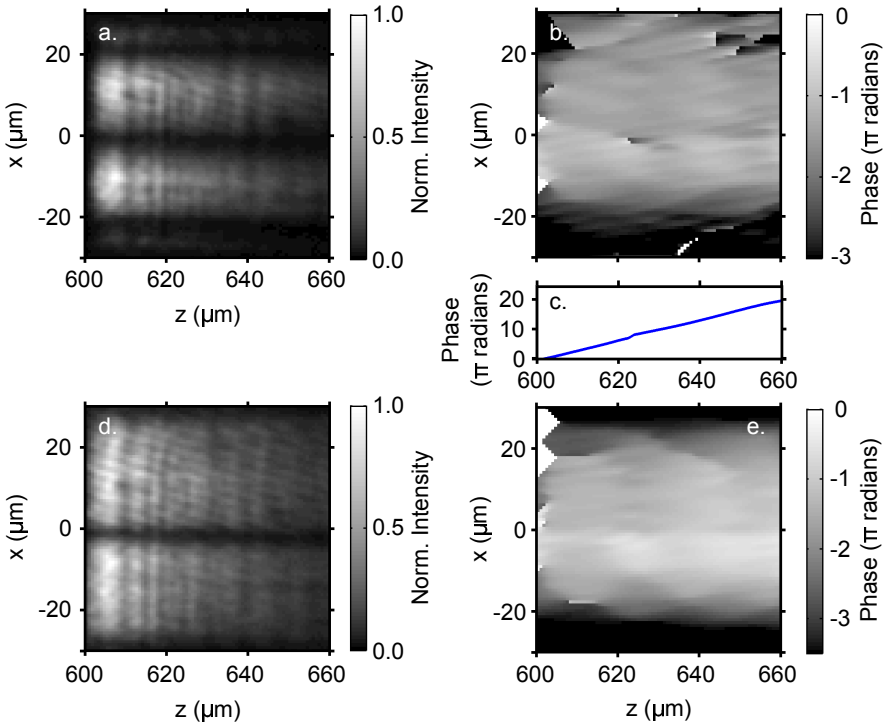

Figure 4.8: Real-space images of intensity and recovered phase of the output beam at low and high power (a-b and d-e respectively) with a phase mask imprinted on the pump beam. The precession of phase along the z-direction - shown in panel c - has been subtracted from the recovered phase to highlight the discontinuity in the transverse direction.

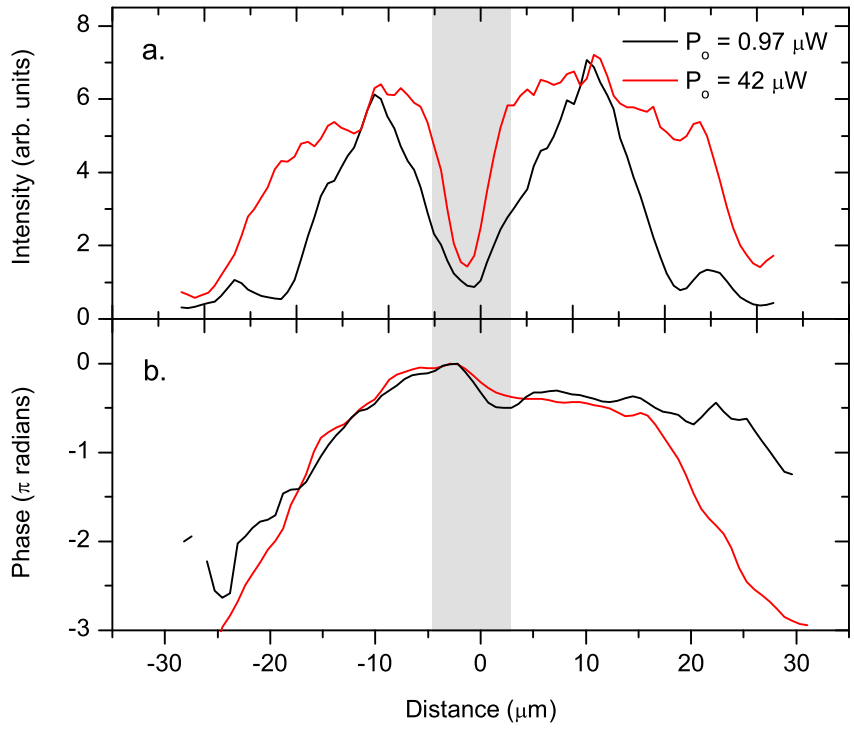

Figure 4.9: Amplitude (a) and phase (b) profiles of PL emission at low and high power with phase mask imprinted on pump beam. Both panels share a legend.

is largely due to the propagation of polaritons. The phase of polaritons therefore precesses at 0.085 μm^{-1} - noting that there are two intensity fringes per cycle. Given the emission wavelength of 0.841 μm this precession suggests a group index of 14, in approximate agreement with 14.9 predicted from the dispersion using group velocity at this detuning from Equation 1.12 and $n_{eff} = c/v_g$.

Figure 4.9 shows cross sections of intensity and phase taken at $x = 626$ μm from which the increase in full width and narrowing of dark notch can be seen clearly. This dark notch can be seen to coincide with a phase jump approaching $\pi/2$. Additionally it can be seen that the phase decreases away from $x = 0$. At low power this can be attributed a geometrical effect as off-axis components travel slightly further and therefore acquire a phase lag relative to those travelling along the z-axis. From Figure 4.9b this curvature is enhanced at high power where the reduction in effective index near the centre of the beam - where the density is greatest - serves to reduce the optical path length for those travelling along the z-axis increasing the relative phase lag of the off-axis components.

The phase mask was swapped for a 100 μm wire. Figure 4.10 shows real-space images of the of the emission and the recovered phase at the output grating. Once again the linear dependence of phase as polaritons travel along the z-direction has been subtracted. The phase precession was found to be the same as that with the phase mask. And again the off-axis components lag those travelling along the z-direction producing a curvature in the wavefront. This effect is enhanced a high power due to the local reduction in effective index at the centre of the beam.

At low power the dark notch in intensity is washed out and the phase varies smoothly in the transverse direction. By contrast at high power two dark notches in intensity form with a corresponding phase jump. This can be seen clearly in the cross sections presented in Figure 4.11 from which it the phase changes abruptly at the point of the dip intensity. Furthermore it can be seen that the jumps in phase are approximately equal and opposite in sign thus conserving the total phase across the whole beam.

This spontaneous development of a phase jump coinciding with a dip in intensity

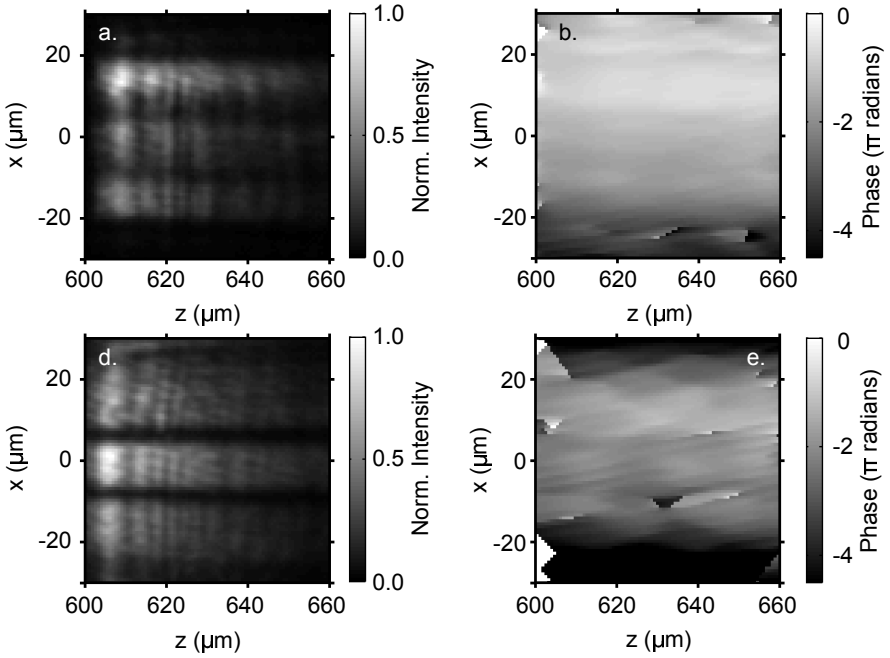

Figure 4.10: Real-space images of intensity and recovered phase of the output beam at low and high power (a-b and d-e respectively) with an amplitude mask imprinted on the pump beam. The precession of phase along the z-direction has been subtracted from the recovered phase to highlight the discontinuity in the transverse direction.

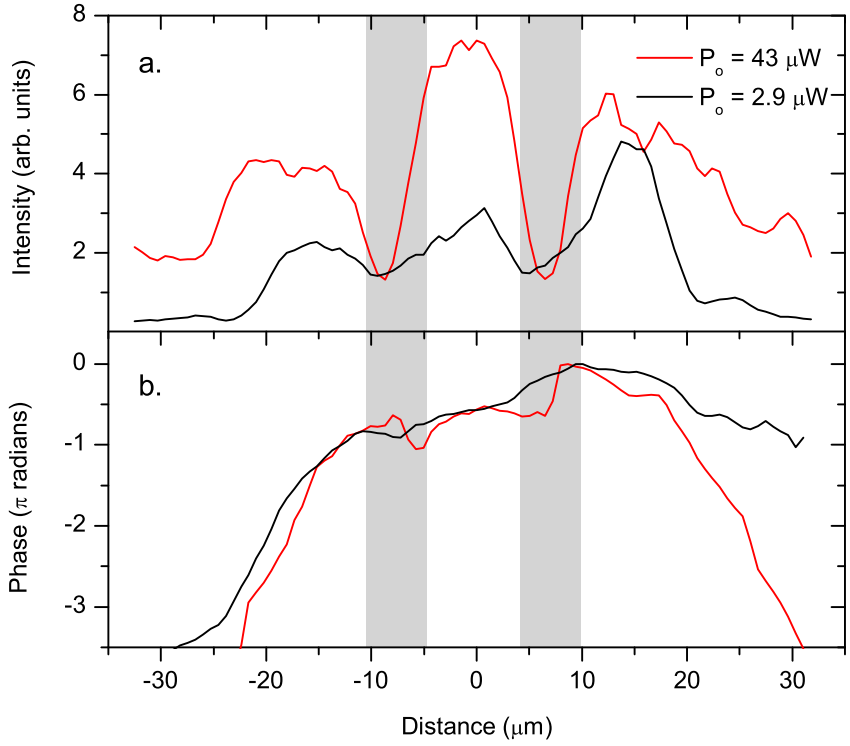

Figure 4.11: Amplitude (a) and phase (b) profiles of PL emission at low and high power with amplitude mask imprinted on pump beam. Both panels share a legend.

is clear evidence of the formation of a pair of dark spatial solitons arising from the nonlinear properties of the waveguide which in-turn derive from polariton-polariton interactions.

4.4 Generation of single dark solitons at 100 K

In Section 3.3 it was shown that the strong coupling regime in this polaritons waveguide device persists up to at least 100 K. From a technological point of view this is potentially a useful fact, allowing for a future waveguide polariton device to operate using liquid nitrogen, rather than liquid helium, as a coolant, greatly reducing the cost to run. However this promise of a III-V based polariton waveguide device operating at elevated temperatures is of course dependent on the accompanying nonlinearities also persisting to high temperatures. In this final section the nonlinear properties of the waveguide device at 100 K are investigated.

The pump beam was once again passed through a phase mask imaged onto the sample surface focused to a 30 μm spot. To avoid excessive absorption and heating the sample the laser was tuned to 8.4 meV below the exciton line and a mechanical shutter was employed to chop the pump beam, producing pulses of 0.1 s duration with a small duty cycle. The incident power on the sample surface was determined by measuring the power before the mechanical shutter and compensating for the losses in the subsequent optics. The average output power could not be measured reliably as the response of the photodiode-based power meter was too slow. However in future the output power could be measured using a fast photodiode calibrated against the power meter and synchronised with the chopping frequency of the input beam.

Figure 4.12 shows the power dependence of the beam width and blackness of the dark notch versus pump power. Above 1 mW the width of the beam and of the dark notch increases. Simultaneously the blackness of the dark notch increases slightly from its low power value. Above 10 mW the dark notch narrows once again to below its width at low power.

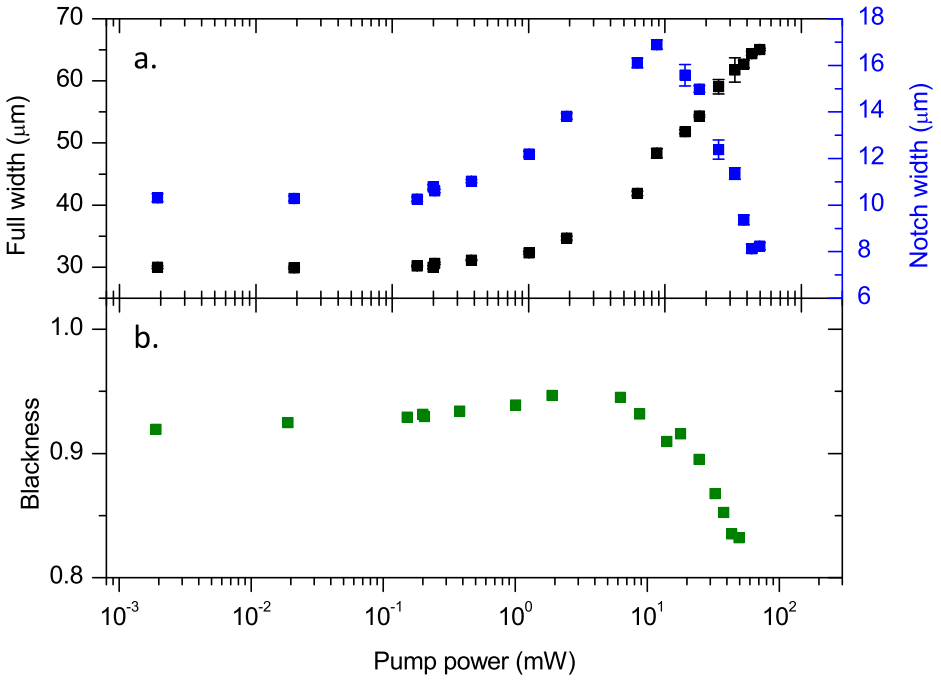

Figure 4.12: Characteristic widths of the beam at the output grating with the phase mask versus pump power (a) showing full width of the beam (left) and of the dark notch (b). Blackness of the dark notch versus pump power (b).

At intermediate powers the whole beam undergoes diffraction, simultaneously increasing the beam- and notch-width. This non-monotonic behaviour is attributed to pre-soliton dynamics which are highly sensitive to the exact input conditions. In any case the dependence of the characteristic widths on pump power illustrates that the nonlinear properties of the waveguide persist up to 100 K. Furthermore on comparing the characteristic widths at low- and high-power the behaviour is qualitatively similar to that observed at 4 K suggesting the formation of a dark spatial soliton.

4.5 Conclusion

In this chapter it was shown repulsive polariton-polariton interactions result in an optical nonlinearity analogous to a negative nonlinear refractive index which scales with the exciton fraction. This nonlinearity was shown to result in the defocusing

of a beam travelling through the waveguide.

By imprinting either a phase jump or a dip in intensity onto the injected beam single or pairs of dark solitons can be generated. The presence of dark solitons was evidenced by the spreading of the beam and narrowing of the dark notch, approaching the ideal case of a dip in intensity on an infinitely wide background. This was further supported by interference measurements which showed that a phase jump was developed at high excitation powers.

By measurement of the threshold powers and comparison with solitons in superfluids the interaction strength between particles was estimated to be some three orders of magnitude greater than that expect between polaritons. This was attributed to the creation of an exciton reservoir under CW conditions populated by the scattering of polaritons into dark-, localised- and high-momentum -exciton states. Using pulsed excitation on the order of several pico-seconds it should be possible to avoid this and measure the interactions between polaritons alone.

Finally it was shown that the nonlinear properties of the waveguide persist up to 100 K potentially allowing for rewritable waveguides and y-splitters devices based upon dark solitons operating at liquid nitrogen temperatures.

Chapter 5

Spatio-temporal solitons

This chapter describes the findings of time-resolved measurements of polaritons in semiconductor waveguides including solitonic effects. The results of this work were reported at the International Conference on the Physics of Semiconductors and at UK Semiconductors in 2014. At the time of writing a manuscript has been uploaded to the arXiv repository [119] and has been accepted for publication in Nature Communications.

5.1 Introduction

Temporal-solitons are shape-preserving excitations which form in the balance between dispersive and nonlinear effects. Temporal solitons have been proposed for [70], and demonstrated in long-haul communication systems [49] and more recently in micro- and nano-scale devices suitable for on-chip information processing and routing [56, 55, 78].

To achieve soliton formation on the short time- and length-scales suitable for on-chip applications requires a system with large dispersive- and nonlinear-effects. In the previous chapter it was established that the effect of polariton-polariton interactions in the waveguide manifests as a giant optical nonlinearity supporting the formation of dark-spatial solitons. The subject of this chapter is to investigate whether this same nonlinearity can be used to balance the GVD in the LPB arising

from the strong-coupling to form bright temporal solitons.

Bright temporal solitons have been observed in semiconductor microcavities, balancing repulsive polariton-polariton interactions against negative effective mass [51]. This waveguide scheme has several important advantages over traditional microcavities for the investigation of solitons however. Firstly the group velocity is an order of magnitude larger than in microcavities, meaning fast in-plane propagation. The use of TIR rather than DBR mirrors to confine the photonic mode mean that the losses are smaller and consequently an external pump is not required to replenish the polariton population. Finally the simple structure more naturally lends itself to create complex nonlinear photonic circuits with applications as novel polaritonic devices [15, 16, 18].

In this chapter experimental evidence is presented for the formation of bright picosecond temporal polaritons solitons at pulse energies less than 0.5 pJ. From this threshold and from the blueshift of the polariton dispersion the size of the exciton-exciton interaction constant and thus optical nonlinearity is deduced. Finally the unique properties of the system, namely the comparable dispersive, diffractive and nonlinear lengths are exploited to demonstrate hybrid spatially-dark and temporally-bright solitons.

5.1.1 Theoretical description

The experimental results presented here are complimented by the results of numerical calculations performed by Dr. Dimity Skryabin of the University of Bath, and Dr. Alexei Yulin of ITMO University, St. Petersberg. The interaction between the photonic mode and QW excitons was described using the Maxwell-Lorentz system. Within the spectral range of interest any GVD arising from the waveguide itself is negligible as are nonlinear effects at the excitation powers considered here. The set equations accounting for the dominant nonlinearity arising from exciton-exciton

interaction is:

$$2i\beta\left(\partial_z + v_g^{-1}\partial_t + \gamma_C\right)A + \partial_x^2 A = -k_X^2\psi \tag{5.1a}$$

$$-2i\left(\partial_t + \gamma_X\right)\psi = \kappa A - g|\psi|^2\psi \tag{5.1b}$$

where z and x are the coordinates along and transverse to the direction of travel and t is time. A is the amplitude of the photonic mode and ψ is the excitonic polarisation scaled to be in the same units. β and v_g is the propagation constant of the uncoupled photon mode at the exciton frequency ω_X and $k_X = \omega_X/c$. κ is the rate of light-matter coupling and g is the exciton-exciton interaction constant. The loss rates $\hbar\gamma_C = 44.3$ μeV and $\hbar\gamma_X = 7.5$ μeV were chosen to fit with the measured frequency dependence of the propagation length from Chapter 3. The input parameters to the simulation were those used in the experiment.

Neglecting losses and assuming plane wave solutions $(A, \psi) \propto e^{iQz - i\delta t}$ the lossless dispersion law is $Q = v_g^{-1}\sqrt{\delta - \Omega_R^2/\delta}$. Here δ is a frequency offset of the polariton branch from ω_X, Q is the offset in wavenumber from β and $2\Omega_R = k_X\sqrt{\kappa v_g/\beta}$ is the vacuum Rabi-splitting, which from sample characterisation is approximately 9 meV. This model reproduces the two-coupled oscillator model used previously and again can be differentiated to yield the GVD parameter β_2 for pulse propagation in the system given by Equation 1.13. For the range of detuning $(\delta_c)$of the LPB relative to the exciton line β_2 varies between 400 and 1000 $\mathrm{ps}^2\ \mathrm{m}^{-1}$.

5.1.2 Experimental methods

Sample 3 from Chapter 3 was placed in a continuous-flow cold-finger cryostat held at approximately 5 K. Excitation was provided by a tunable pulsed Ti:Sapphire laser producing 100 fs duration pulses at a repetition rate of 82 MHz. These pulses were passed through a dispersion-free diffraction pulse-shaper allowing the spectral width and central wavelength of the pulse to be controlled. As a consequence of the square aperture used in the pulse-shaper the resulting pulses have a top-hat spectrum.

The beam was focused to a 20 μm spot on the sample surface giving an angular spread of approximately 0.5 $\mu\mathrm{m}^{-1}$. The pulse was injected into the waveguide

through a grating coupler by matching the energy and incidence angle to a part of LPB. The PL emission from a second grating coupler 600 µm away was imaged onto the entrance slit of a single grating spectrometer and either dispersed onto the CCD or directed to a streak camera.

The streak camera had a resolution of 2 ps as measured from the response to the reflected laser pulse of duration 350 fs (deduced from the Fourier transform of the corresponding spectrum). The entrance to the streak camera has a 60 µm entrance slit which corresponds to 6 µm on the sample surface. Integrating over such a small area avoids the problem of uncertainty due to the finite polariton lifetime on the grating.

5.2 Time-resolved measurements

Figure 5.1 shows the streak camera images and corresponding angle-resolved spectrum of the PL emission from the output grating. At low excitation power the 350 fs duration pulse is dilated to 4 ps on propagation whilst at high power the pulse is much shorter in time, close to the resolution limit of the streak camera, and appears to be symmetrical in time. Simultaneously the pulse undergoes a lateral spreading in real space. Such lateral spreading was observed in the CW experiments presented in Chapter 4 attributed to a defocusing non-linearity where polariton-polariton interactions deflect polaritons away from their direction of travel.

At low power the output spectrum follows the LPB as only the portion of the input pulse - which has a finite range of energies and wavenumbers - coinciding with the LPB can propagate in the waveguide. Therefore polaritons in different parts of LPB can be injected by adjusting the central energy and incidence angle of the input pulse. At high power the spectrum undergoes a significant narrowing, typically towards the central energy of the input pulse.

The temporal profile was taken from the centre of the soliton and the spectrum extracted along the LPB. Figure 5.2 shows these cross sections for a number of excitation powers relative to that required for soliton formation. At low power the

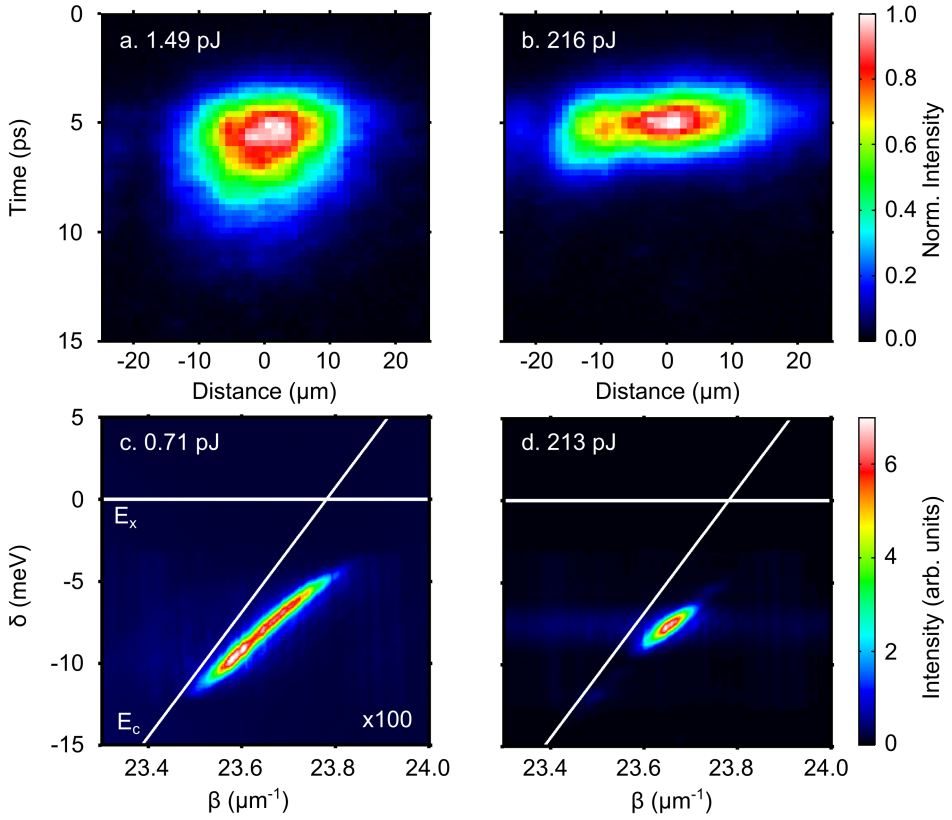

Figure 5.1: Time-resolved real-space images of PL emission from output grating at low (a) and high (b) excitation power and angle-resolved PL spectra at similar powers (c and d respectively). The pulse energy at the output is indicated in each panel. Panels a and b, and c and d share a colour scales.

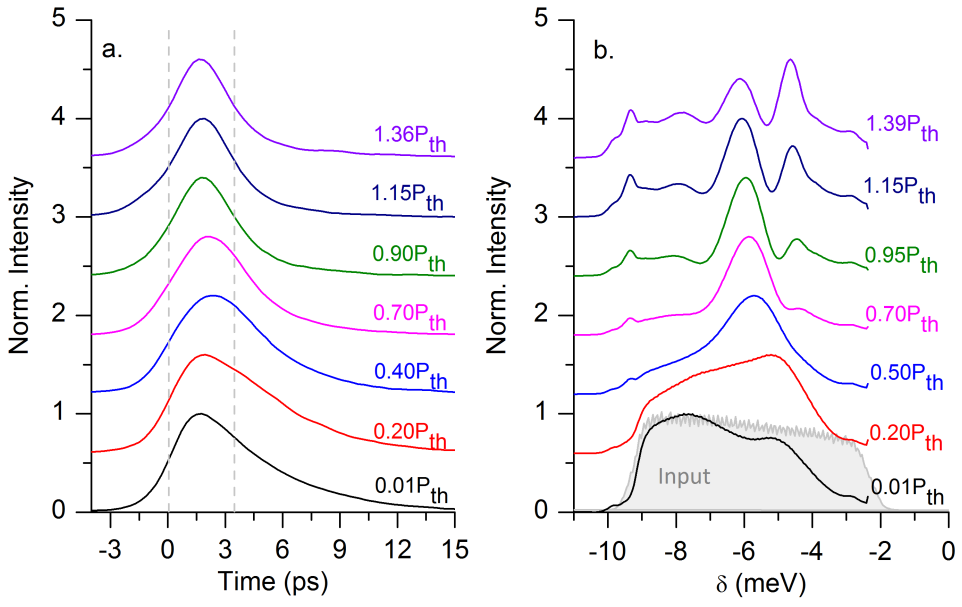

Figure 5.2: Temporal-profiles (a) for various excitation powers relative to that required for soliton formation (P_{th}) and the corresponding spectrum extracted along the lower polariton branch (b). The spectrum of the input pulse is shown in grey overlaid on the output spectrum at low power.

wavepacket has a characteristic shape with a sharp leading edge and long tail. This sharp turn-on corresponds to polaritons in the photonic part of the LPB which travel with the greatest group velocity and thus arrive at the output grating first. The long tail corresponds to progressively excitonic polaritons which travel at smaller group velocities. At low power the corresponding spectrum has a top-hat shape approximately equal to that at the input. The modification to the spectrum can be attributed to the angle- and energy-dependence of the coupling efficiency and absorption in the waveguide.

With increasing excitation power the wavepacket becomes increasingly narrow and symmetrical in time, the duration approaching the resolution of the streak camera. Simultaneously the spectrum narrows into a central soliton energy. Above the threshold power for soliton formation the spectrum becomes increasing modulated with appearance of the spectral side-bands to the central soliton energy. This modulation in the frequency-domain suggests similar modulation in the time-domain on the order of 650 fs. This is far below the resolution of the setup and only occurs at the highest pump powers available. Assuming that this second point can be addressed the structure in the time-domain could be investigated further using ultra-fast techniques such as autocorrelation [55], frequency-resolved optical gating (FROG) [120] or frequency-resolved electrical gating (FREG) [56].

5.2.1 Power and detuning dependence

The temporal- and spectral-narrowing effect with increasing excitation power was investigated by extracting the duration and spectral-width for a range of detuning (δ_c) of the central energy of the input pulse relative to the exciton line. The pulse duration was defined as the full-width at half-maximum (FWHM) whilst the spectral width was defined as the full-width at one-third maximum to avoid difficulties due to modulation in the spectrum. The spectral- and temporal-width versus pulse energy at the end of the waveguide is shown in Figure 5.3. The pulse energy was determined by focusing the emission from the output grating onto a photodiode-based power meter and dividing by the repetition rate of the laser (82 MHz). A further factor

of 4 was included to account for the fraction of power scattered into the substrate, determined by FDTD simulation to obtain the pulse energy before out-coupling.

At low power the spectral width at the output is constant and approximately equal to that at the input (5.5 meV) whilst the 350 fs pulse injected into the waveguide is dilated to several picoseconds. The time-bandwidth product of the wavepacket at the output is therefore well above the Fourier transform limit. Above a threshold of 100 fJ there is a significant spectral and temporal narrowing. This reduction in time-bandwidth product towards the Fourier limit is indicative of the reduction in GVD-induced chirp and is clear evidence for solitonic behaviour. This is well reproduced by the extracted duration and spectral width of the pulse from numerically calculated solutions of Equations 5.1. Here the results of the numerical calculations have been convolved with a Gaussian of 2 ps FWHM to account for the effect of the streak camera resolution.

The reduction in bandwidth above threshold here is a consequence of losses in the system. The soliton is initially formed with the temporal- and spectral-width close to that of the input pulse. As the soliton loses energy the effect of the nonlinearity reduces and so can only partially compensate the GVD. The soliton then adiabatically increases its temporal-width so that the nonlinearity once again compensates GVD. However in order to maintain the same time-bandwidth product - defined by the Fourier transform of the characteristic sech^2-shape - the soliton must also reduce its spectral-width. Indeed from Figure 5.3 the spectral narrowing, like the propagation length measured in Chapter 3 from which it is derived, is not strongly dependent on detuning over the range investigated.

The formation of a soliton requires that the characteristic nonlinear length (L_{NL}) is equal to the dispersion length (L_{DS}). Noting that the characteristic loss length of the sample for this range of detuning is approximately 400 μm, the input pulse energy at threshold is $E = 0.45$ pJ. Setting $L_{NL} = L_{DS}$ we obtain $\gamma = T/(EL_{DS}) \approx -18,000\ \mathrm{W^{-1}m^{-1}}$. This nonlinear parameter can then be related to the nonlinear refractive index by Equation 1.15. The effective mode volume of the waveguide is $A_{eff} = 6.6\ \mu\mathrm{m}^2$. Rearranging the expression γ yields $n_2 = -1.6 \times 10^{-14}\ \mathrm{m^2W^{-1}}$.

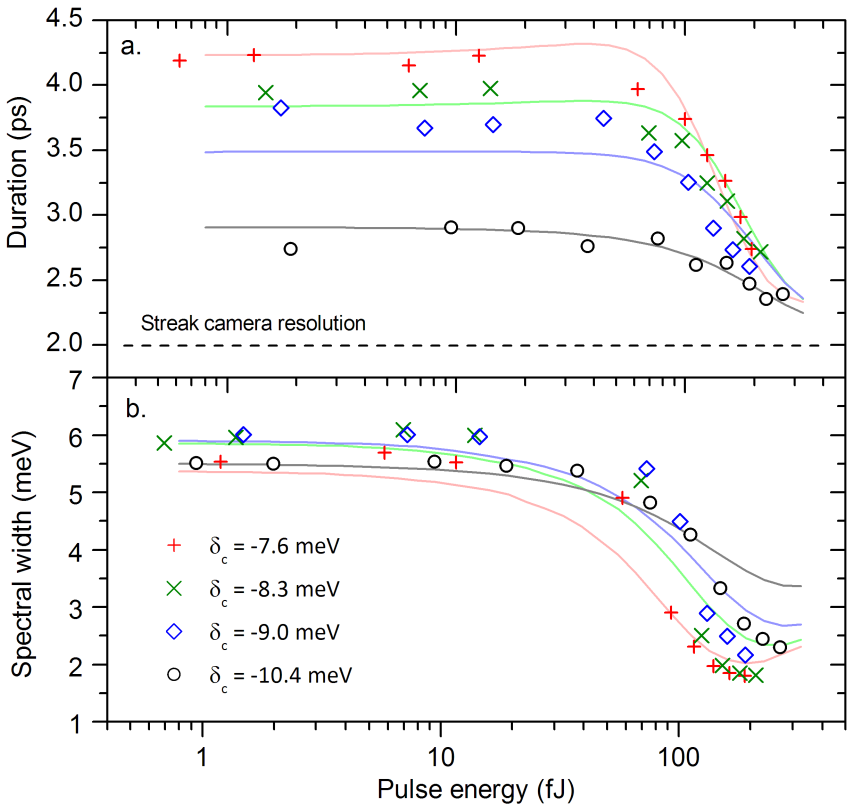

Figure 5.3: Power dependence of pulse duration (a) and spectral width (b) at the output of the waveguide for a range of detuning of the central pulse energy relative to the exciton transition energy (δ_c). Calculated duration and spectral width for each δ_c is shown by solid lines of the corresponding colour.

A key characteristic of solitonic behaviour is that the shape is invariant during propagation. This could be observed directly using multiple gratings etched into the waveguide at various positions, or equivalently, by varying the characteristic lengths L_{NL} and L_{DS} and keeping the physical length fixed. Therefore by changing δ_c between -7.6 meV and -10.4 meV the scale is varied between 5.5 and 13.6 dispersion lengths at each of which there is clear temporal narrowing from the low power case indicative of soliton formation.

Finally it is important to note that the pulse energy at the output is directly proportional the input power: the exact ratio is dependent on the exact experimental conditions such as incidence angle and central energy of the pulse. This indicates that polaritons are not lost from the system but rather transferred to different states. This rules-out a nonlinear absorption mechanism where it might be imagined that polaritons away from the central energy are simply filtered-out. The resulting spectrally-narrow pulse would then experience little GVD as it propagated and so would give the appearance of narrowing with increasing power but would have a sub-linear input-output power dependence. Additionally the lack of nonlinear absorption suggests that even at high power the Mott-density has not been reached and that the system therefore remains in the strong-coupling regime.

5.2.2 Spectral properties

At high power the repulsive interactions between polaritons in the soliton results in a renormalisation of the dispersion shown in the line cuts taken from angle-resolved spectra at the central soliton wavenumber in Figure 5.4a. This dependence was extracted by fitting a Gaussian distribution to line-cuts at each power and detuning. Figure 5.4b shows the extracted energy shift relative to that at low power from which there is a clear blueshift with increasing power which saturates above the threshold for soliton formation (100 fJ). This behaviour is strongest for small δ_c where $|X|^2$ and thus polariton-polariton interactions are stronger.

Crucially the maximum blueshift at saturation is orders of magnitude smaller than half the Rabi-splitting (4.5 meV) and decreases with δ_c and thus exciton frac-

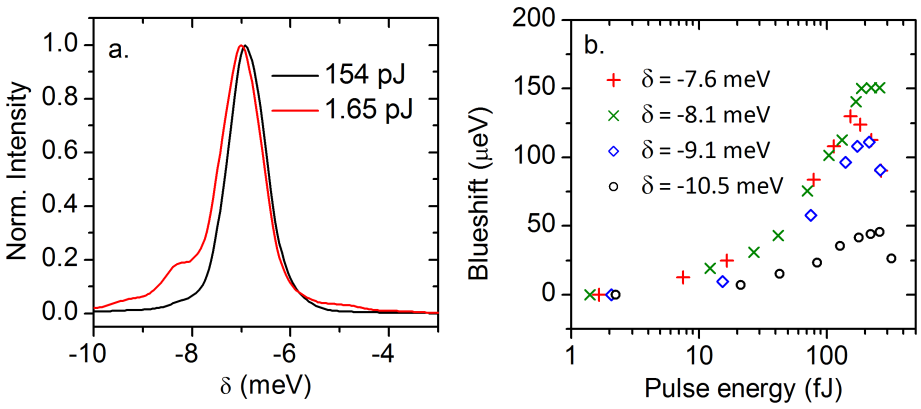

Figure 5.4: Line cuts taken from angle-resolved spectra at the central soliton wavenumber (a) for a detuning of $\delta_c = -7.6$ meV between the central pulse energy relative to the exciton line. Shift in energy versus power for various δ extracted by fitting a Gaussian distribution to the

tion. This indicates that the strong-coupling regime has not been quenched which would cause a collapse of the Rabi-splitting and should be insensitive to exciton fraction. Additionally the linearity in input-output power suggests that above threshold, at which the blueshift saturates, polaritons are not lost or absorbed but rather transferred from the soliton to different states, serving to reduce the peak density within the soliton and thus the interaction-driven blueshift.

From the pulse-energy the particle density within the soliton, and thus interaction strength producing the observed blueshift, can be evaluated. For a detuning of $\delta_c = -7.6$ meV, $|X|^2 = 26\%$ and $v_g = 43$ μm ps^{-1}. Taking the transverse width of the soliton $\Delta x = 20$ μm and duration $T = 1.5$ ps the particle density is:

$$N_x = \frac{|X|^2}{N_{QW}} \frac{E}{\hbar\omega} \frac{1}{v_g T \Delta x} \tag{5.2}$$

where E is the pulse energy, $\hbar\omega$ is the central soliton energy and N_{QW} is the number of QWs between which the exciton population is distributed. For a pulse energy of $E = 0.1$ pJ this gives an exciton density of $N_x = 28.5$ μm^{-2} per QW, well below the Mott density observed in similar QWs ($N_{Mott} = 100 - 1600$ μm^{-2}) [114]. From Figure 5.4 this exciton density results in an energy shift of $\Delta E = 100$ μeV giving an interaction constant of $g = \Delta E / N_x = 3.5$ μeV μm^2 in good agreement the theoretical estimate $g = 3a_b^2 E_x = 3$ μeV μm^2 where a_b and E_x is the exciton Bohr radius and binding energy respectively [72].

The interaction constant deduced here is an order of magnitude below that obtained in Chapter 4. This is because under CW the background reservoir of dark-, localised- and high-momentum exciton states is constantly replenished by the scattering of polaritons into these states. Polaritons then interacted with this reservoir in addition to each other resulting in an increased optical nonlinearity. In contrast, the pulses used here are sufficiently short and separated in time (19.2 ps) relative to the exciton lifetime (> 1 ps [115]) that these exciton states are not effectively populated. Therefore the value calculated here represents the interaction strength between polaritons alone.

From Equation 1.12 the shift in energy is equivalent to a change in wavenumber (Δk) which can be related to the nonlinear length by $L_{NL} = 1/\Delta k$. Substituting in Equation 5.2 then yields an expression for the nonlinear parameter:

$$\gamma = \frac{(g/\hbar)|X|^2}{\hbar\omega N_{QW}\Delta x v_g^2} \tag{5.3}$$

For $g = 3.5\ \mu\mathrm{m}^2$ this yields a nonlinear parameter $\gamma = -52800\ \mathrm{W}^{-1}\mathrm{m}^{-1}$ and subsequently $n_2 = -4.7 \times 10^{-14}\,\mathrm{m}^2\,\mathrm{W}^{-1}$ in close agreement with the estimate from the soliton threshold pulse energy determined in Section 5.2.1.

From Figure 5.4a the blueshift of the dispersion is accompanied by a reduction in linewidth from 1.07 ± 0.02 to 0.93 ± 0.01 meV, towards the lower limit of 0.84 ± 0.02 meV imposed by the finite lifetime in the grating region. This linewidth narrowing behaviour was observed at all detuning and suggests an increase in coherence in the soliton regime which can be attributed to the coherent redistribution of polaritons via stimulated scattering processes [35] into this central state. Whilst there is insufficient data here to drawing meaningful conclusions it does hint at the possibility of observing soliton squeezing effects [121, 122] in this waveguide system.

5.3 Polariton time of flight

An important evidence for solitonic propagation is the cancellation of GVD such that all spectral components travel with the same group velocity. This can observed directly by measuring the time of flight (ToF) though the waveguide. The polariton

ToF was measured by projecting the Fourier transform of the PL emission at the output of the waveguide onto the entrance of the entrance-slit of the streak camera which selects a particular in-plane wavenumber. As demonstrated in the angle-resolved PL spectra there is a one-to-one correspondence between wavenumber and energy of polaritons in the LPB. Therefore by extracting the ToF versus wavenumber we obtain the dependence on energy.

Figure 5.5a shows the signal from the streak camera observed just above threshold from which two main features can be seen, corresponding to the laser reflection and emission from the output of the waveguide. The PL emission consists of two components: a solitonic component for which the ToF is independent of wavenumber and a weaker, background component which has some dependence on wavenumber. With increasing power this non-solitonic background becomes weaker relative to the soliton intensity and can no longer be discerned at the highest powers. The time of arrival was extracted by fitting a Gaussian distribution to each peak (shown by the coloured areas under the streak camera signal). The ToF is then the delay between the laser reflection and PL emission from the output of the waveguide.

The raw ToF at low power is approximately 2 ps shorter than that predicted from the polariton dispersion. This however corresponds to a path difference of just 600 μm between the laser reflection and PL emission that can reasonably be attributed to path differences through the optics in the experiment. To account for this a constant offset was added to the ToF at all powers. This offset is the weighted-average discrepancy between the measured ToF at low power and that predicted from the observed polariton dispersion.

Figure 5.5b shows the extracted ToF versus wavenumber at low power and just above threshold. At low power the change in group velocity predicted from the polariton dispersion is reproduced in the ToF. At high power the wavenumber-dependent background components also follow this dispersion. The significance of this co-propagating non-solitonic background polaritons is that it demonstrates that the strong coupling regime still holds even above the threshold for soliton formation. By contrast, all the components of the soliton arrive within > 1 ps. With this

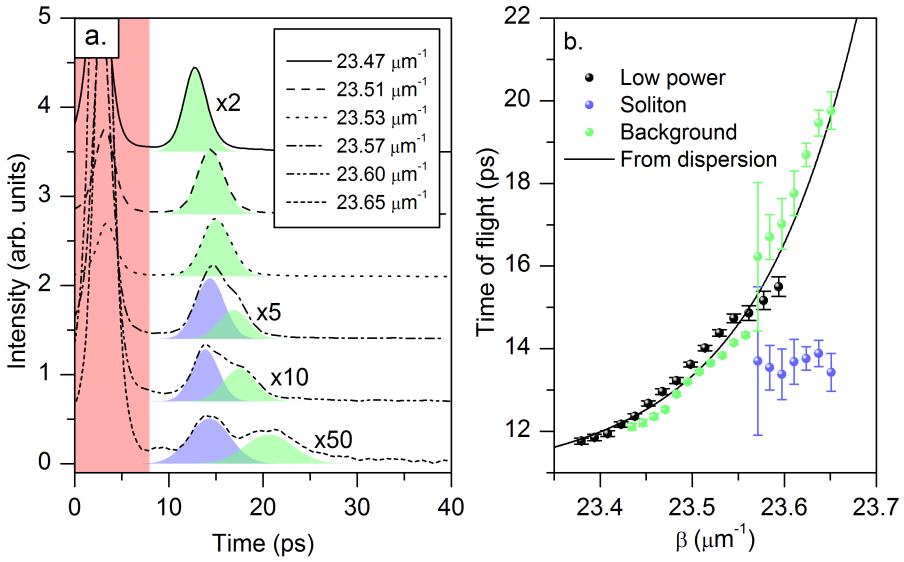

Figure 5.5: Streak camera signal extracted at various in-plane wavenumbers just above soliton formation threshold (a) showing laser reflection (pink), the soliton components (blue) and non-solitonic background (green). Extracted time of flight versus in-plane wavenumber at low and high power (b) showing soliton components and non-solitonic background. Here the central energy of the pulse was 8.0 meV below the exciton-line.

technique the soliton duration can therefore be measured with an accuracy greater precision than the resolution of the streak camera.

The polariton ToF was measured for different detuning between the central pulse energy and the exciton line. The same input power was used at each detuning. Figure 5.6 shows the dependence of polariton ToF at low power and above threshold for soliton formation. Again at low power the polariton ToF follows that predicted from the dispersion whilst above threshold ToF for all spectral components of the soliton is, within experimental error, independent of wavenumber and is consistently shorter than at low power. The independence of the ToF with wavenumber indicates cancellation of GVD which is clear evidence of soliton behaviour.

The linear soliton dispersion further discounts a nonlinear-absorption explanation of the spectral-narrowing as a such a pulse would still experience some dispersion. Additionally the dependence of soliton ToF on δ_c suggests that the observed effects derive from the presence of polaritons and that the system therefore remains in the strong-coupling regime. Furthermore the soliton ToF is consistently longer

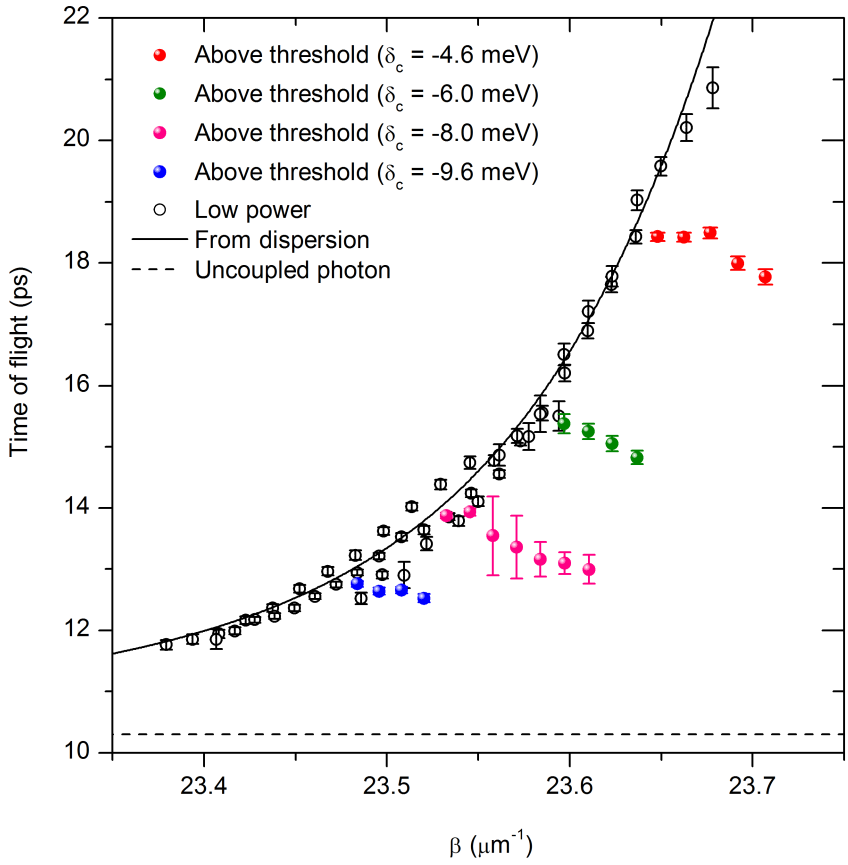

Figure 5.6: Extracted time of flight (left) versus wavenumber at low power and for soliton components well above threshold with detuning between the central pulse energy and exciton transition energy (δ_c).

than that expected for the bare waveguide (10.3 ps) as might be expected if the strong-coupling regime had simply been quenched.

5.4 Temporally-bright and spatially-dark solitons

In this section the conditions where diffraction in the transverse direction is important are considered. The unique combination of properties in this system - the comparable dispersive, diffractive and nonlinear length scales - allow for solitonic behaviour to be supported in both space and time. This section considers the hybridisation of the dark-spatial solitons from Chapter 4 with the bright-temporal solitons of this chapter.

As in Chapter 4 the pump beam was passed through a mask which introduces a π-phase jump to half of the beam. This produces a characteristic two-lobed pump spot with an intensity minimum at the point of the phase jump. An interferogram of the phase mask used and the resulting intensity distribution are shown in Figure 5.7 in addition to the streak camera images of the output wavepacket. The input pulse had a bandwidth of 9.4 meV was tuned to -7.5 meV below the exciton line.

At low power the two-lobed shape is retained at the output but the width of the distribution is slightly altered by diffraction in the waveguide. In the time-domain either lobe is dispersed as in Section 5.2 and has the characteristic sharp leading edge and long tail arising from the GVD. At high power both lobes undergo a narrowing in time as observed for the bright-temporal soliton. Simultaneously both lobes spread laterally, increasing the total width whilst decreasing the width of the notch. This is illustrated by the cross sections taken through the streak camera images shown in Figure 5.7e and f.

This behaviour was characterised by extracting the characteristic width and duration of the wavepacket at various pump powers. The total width was defined by the points at one-third of the maximum intensity for either lobe. The width of the notch was defined by the half-maximum points relative to the maximum intensity of the lobe and to that in the notch, i.e. $I = (I_{max} + I_{notch})/2$. The duration was

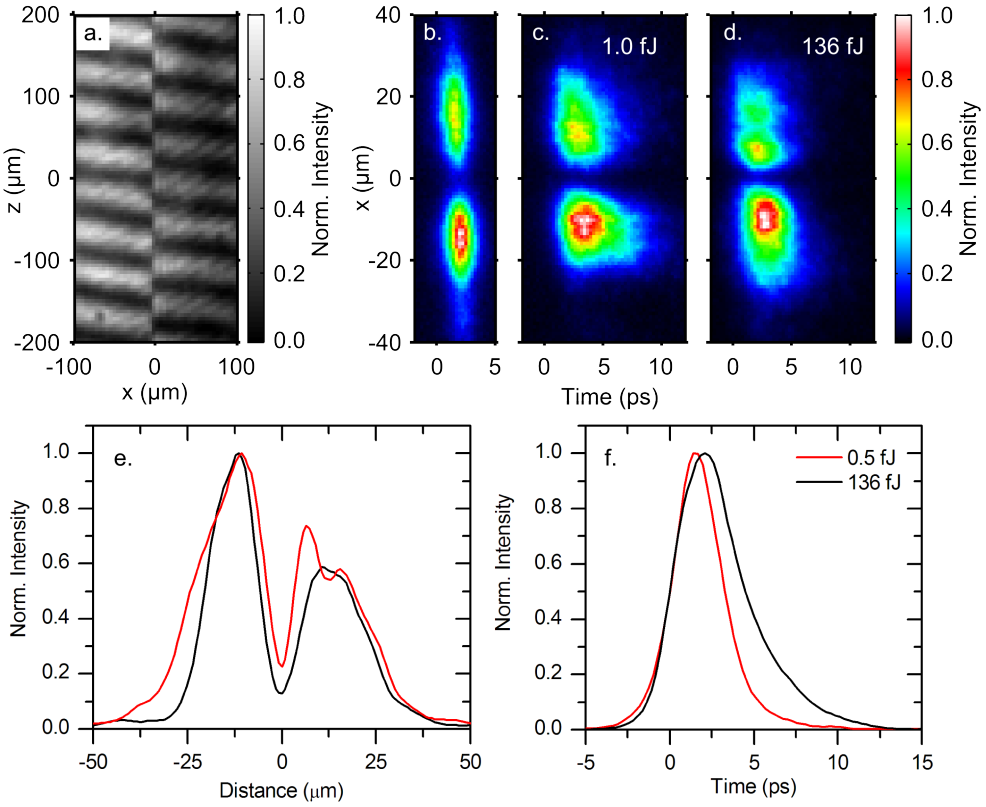

Figure 5.7: Interferogram of phase mask (a) and resulting intensity distribution of input pulse (b). Streak camera traces of the output pulse of the waveguide at low (c) and high power (d). Cross sections of the output pulse at low and high power in the transverse direction (e) and in time (f). Panels b, c and d share a colour scale and are plotted on the same vertical scale.

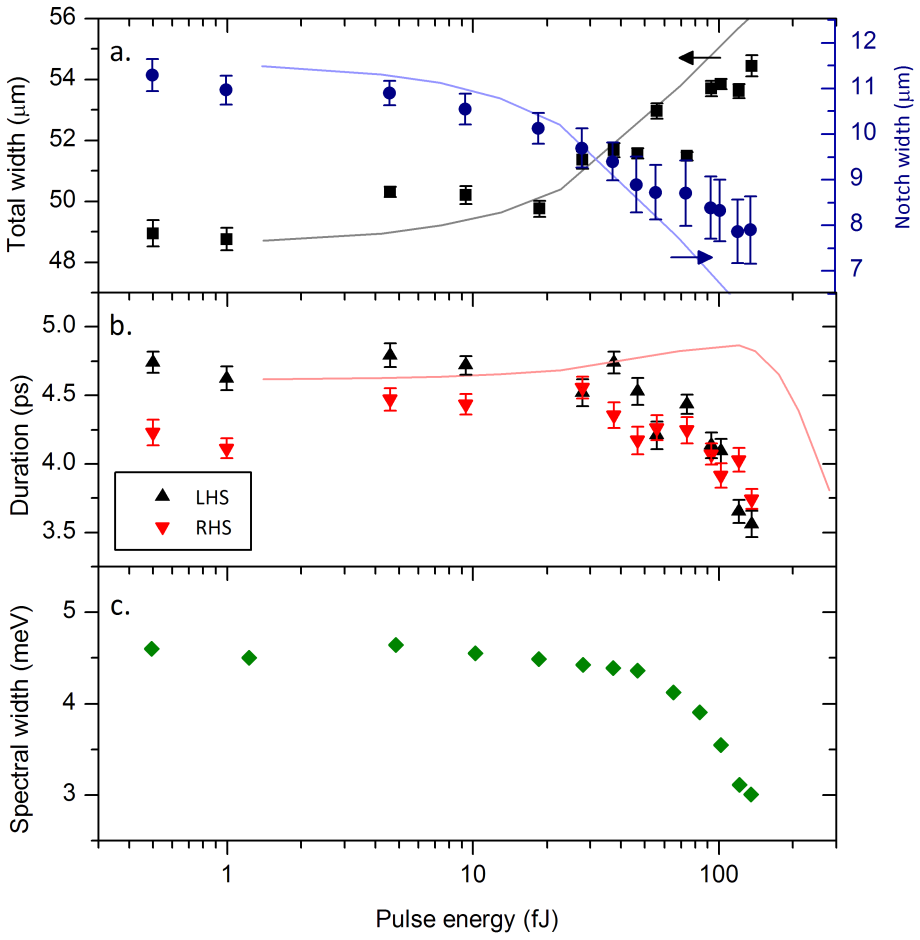

Figure 5.8: Extracted full width in transverse direction and width of the dark notch (a. left and right), duration of the left- and right-hand side (LHS and RHS) lobe (b) and spectral width (c) versus pulse energy. Results of numerical simulations shown in solid lines of the same colour.

again defined as the FWHM whilst the spectral width was defined as the full-width at one-third maximum. Figure 5.8 shows the extracted parameters versus pulse energy. The maximum pulse energy here is slightly less than that in the previous section due to the additional optics required.

With increasing power above 10 fJ the total width of the distribution increases by 10 % whilst the dark notch decrease in width by 30 %. In the ideal case the dark soliton is a dip in intensity on a bright background extending to infinity at either side. The width of the dark notch is then set by the balance of nonlinear and diffractive phases. The observed behaviour therefore represents the distribution moving towards that of a dark-soliton as observed in Chapter 4.

At low power either lobe is dispersed in time to approximately 4.5 ps whilst the output spectrum has a top-hat shape and a bandwidth of 5.5 meV, similar to that observed for the temporal soliton at this detuning in Section 5.2. The reduction in bandwidth here with respect to the input is due to the finite range of wavenumbers of the pump and thus the limited coupling efficiency, and to absorption near the exciton line.

At high power both lobes of the wavepacket undergo a temporal narrowing of 20 % accompanied by a reduction in spectral width of 30 %. In Section 5.2 it was shown that such a reduction in the time-bandwidth product was indicative of the formation of a bright-temporal soliton.

The wavepacket therefore simultaneously demonstrates properties of both dark- and bright-solitons and can be described intuitively as a dark-spatial soliton form between two bright-temporal solitons. Whilst a similar hybrid has been predicted [123] this is the first time that this particular flavour of spatio-temporal soliton has been observed and is only made possible by the properties of the system. This behaviour is qualitatively reproduced by the results of numerical calculations.

5.5 Discussion and conclusion

In this chapter the experimental evidence for solitonic propagation in polariton waveguides was presented; the foremost of which is the significant temporal narrowing above a threshold energy and the independence of ToF on wavenumber. This soliton behaviour is ascribed to the strong-coupling in the system which is evidenced by the linearity of input versus output power, the strong dependence on detuning, and the presence of co-propagating, non-solitonic background.

This experimental evidence is supported by numerical solution of Equations 5.1 shown overlaid in Figures 5.3 and 5.8 with which there is semiquantitative agreement. The results of the numerical calculations are summarised in Figure 5.9. At low power the wavepacket has the characteristic temporal profile with a sharp leading edge and long tail in both the lossless and lossy cases. With increasing power

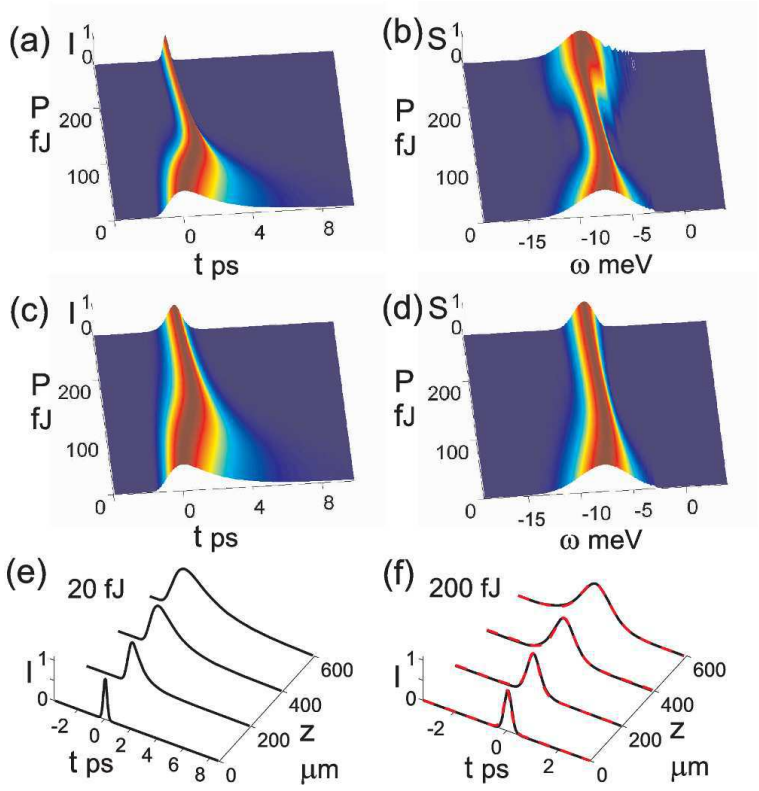

Figure 5.9: Numerically calculated time- and frequency profile at the end of the waveguide for the lossless (a, b) and lossy (c, d) cases. Evolution of the pulse at different points along the waveguide including loss below (e) and above (f) the soliton formation energy. The analytical solution for the lossless case is shown in red in panel f.

the wavepacket becomes increasingly short and symmetrical in time reproducing the behaviour observed in the experiment. Whilst the behaviour in each case is qualitatively similar it is clear that the introduction of losses in the system limits the temporal compression at the end of the waveguide.

In the frequency domain however these two cases differ significantly. In the lossless case the pulse initially undergoes spectral narrowing before increasing as extra harmonics are generated through self-phase modulation, whilst in the lossy case the pulse undergoes a spectral narrowing into a central soliton energy as observed experimentally. In the later, the simultaneous narrowing in time and frequency serves to maintain the same time-bandwidth product given by the transform-limit of the soliton envelope.

In the experiment it was not possible to observe the same soliton at several physical positions. It is therefore instructive to examine the pulse shape of the

numerically calculated pulse as it propagates along the waveguide. The calculated profile of the wavepacket at low and high power along the waveguide is shown in Figure 5.9e and f. At low power the sub-picosecond pulse injected to the waveguide disperses as it travels, acquiring the characteristic shape indicative of the GVD-induced chirp and increasing in duration. This similar to the dependence on detuning - and thus position in terms of dispersion length - observed experimentally. At high power however the wavepacket maintains the same shape but increases it duration as it propagates, thereby adiabatically accommodating the losses.

This dilation of the soliton to accommodate loss is further supported by comparison with an analytical solution to Equation 5.1 which can be obtained in the absence of loss and neglecting the transverse direction (see Appendix B). This analytical solution is shown overlaid in Figure 5.9f. The agreement between this ideal, analytical soliton solution and the numerically calculated profile illustrates that at each point along the waveguide the wavepacket is solitonic and that between each point the soliton looses energy and must adjust its size correspondingly.

In Section 5.2.1 the threshold power for soliton formation was used to deduce the nonlinear parameters of the waveguide, $\gamma = 18000\ \mathrm{W^{-1}m^{-1}}$ and $n_2 = -1.6 \times 10^{-14}\ \mathrm{m^2W^{-1}}$. It should be noted that this is an effective nonlinear refractive index used to allow a comparison between bulk media and this system in which the physics behind the nonlinear effects are derived is very different. It is clear however that the nonlinearity here is more than three orders of magnitude larger than $6 \times 10^{-18}\mathrm{m^2W^{-1}}$ found in silicon [56, 78] and InGaP [55] which have recently been used in a suspended PhC waveguide geometry. In those systems solitons were formed at pulse energies of 12 pJ for InGaP and 9 pJ for silicon, well above the 0.45 pJ deduced at the input grating in this system. Furthermore the effective mode areas are smaller ($\sim 0.5\ \mu\mathrm{m}^2$) and the physical lengths much longer (3.6 and 1 mm respectively) than in the waveguide polariton system, both of which serve to reduce the threshold power and the latter at the expense of increased circuit size.

It is also important to compare this nonlinearity to III-V waveguides in the weak coupling regime. In the 1997 work of Bélanger *et al* [124] soliton-like pulses were

generated in a 2.5 mm long AlGaAs waveguide at pulse energies of 40 pJ from which a nonlinear parameter of $\gamma \sim 20$ $\mathrm{W^{-1}m^{-1}}$ may be inferred. This agrees with their quoted nonlinear refractive index $n_2 = -1.82 \times 10^{-17}$ $\mathrm{m^2W^{-1}}$ given the effective area 5 $\mu\mathrm{m}^2$ and wavelength 820 nm. The utilisation of strong coupling therefore affords an increase of nearly three orders of magnitude in the nonlinearity.

Finally it is worthwhile to consider how the soliton velocity, which would govern data transmission rates, compares with other systems suitable for on-chip soliton devices. In Section 5.3 it was shown that the soliton velocity strong depends on detuning from the exciton line and varies between 32 and 49 $\mu\mathrm{m\,ps^{-1}}$ corresponding to a group index between 6.2 and 9.4. This is comparable to a group index of 8 and 30 quoted in Refs. [55] and [56] respectively and is only a factor ~ 2 higher than 3.477 for bulk silicon at 1550 nm which may be considered as the upper limit on the speed of light for on-chip semiconductor photonic devices.

In conclusion the strong-coupling between the photon and exciton modes of the waveguide provides a massive group velocity dispersion of 400-1000 $\mathrm{ps^2m^{-1}}$ which can be balanced against the effective nonlinearity of $\gamma = 18000$ $\mathrm{W^{-1}m^{-1}}$ that arises from inter-particle interactions inherited from the exciton component to form solitons at record breaking low-power and short formation lengths. Whilst this GaAs-based systems operates a 5 K it has been demonstrated that polariton and their nonlinearities can persist up to room temperature in wide bandgap materials such as GaN [112] and ZnO [125]. It can therefore be envisaged that such effects could be realised at high temperature and indeed it has been demonstrated that long-range propagation in the linear regime is possible in GaN waveguides [29].

Chapter 6

Future plans and conclusions

Polaritons in semiconductors waveguide were first investigated in the late 1980s and early 1990s but failed to make the same impact as semiconductor microcavities which during the two decades following their first observation have been shown to be rich vein of interesting physics. The lack of progress made with waveguide scheme may be attributed in part to the lack of direct access to the polariton dispersion which was a boon to studies in microcavities. However the last twenty years has also seen considerable advances in photonics which allow the dispersion of light to be engineered through the creation of photonic crystals and integrated grating couplers. Through the use of such integrated grating couplers in Chapter 3 the formation polaritons in a semiconductor waveguide was unambiguously demonstrated by the direct observation of the characteristic anti-crossing behaviour indicative of the strong coupling regime between the exciton and photon modes. This represents a significant advancement on previous studies where the presence of polaritons could only be inferred [27, 28, 29].

In Chapter 4 it was shown that the repulsive interactions between polaritons, inherited from exciton parent species manifest in the optical properties as a giant nonlinearity akin to a Kerr material. The negative sign of the nonlinear refractive index results in the defocussing of a high intensity beam travelling through the waveguide. This optical nonlinearity was then shown to support the formation of dark spatial solitions. By imprinting either a phase jump or a dip in intensity either

a single dark soliton, or pair of soltions could be generated. As the refractive index is reduced in the high intensity regions, the dark notch of the soliton has a higher index it was suggested that this could be used to create re-writeable waveguide or y-splitter router in a future polaritonic device.

In Chapter 5 it was shown that the anti-crossing region of the polariton dispersion gives rise to a massive GVD. This was shown to cause a dilation of a 100 fs duration pulses injected into the waveguide to several picoseconds. At high power, and thus high particle densities the nonlinear effect from polariton-polariton interactions cancels this GVD to form a bright temporal soliton. This was evidenced by both a narrowing in duration relative to the linear case and by observation of a linearisation of the dispersion for the soliton through time of flight measurements. By virtue of the comparable formation-length and loss-lengths it was found that in the presence of loss the soliton adiabatically adjust its duration and spectral width in order to maintain its time-bandwidth product. Finally due to the comparable nonlinear-, dispersive- and diffractive-lengths the waveguide polariton system was shown to simultaneously support the formation of dark-spatial solitons and bright temporal solitons form a previously unobserved variety of spatio-temporal soliton.

Future work on waveguide polaritons should be directed towards the creation of circuit elements and interconnects using ridge waveguides or photonic crystals to exploit the advances in photonics and nonlinear properties of polaritons. By reducing the dimensionality to a wire the interactions between polaritons should play a greater role, reducing the threshold powers for the onset of the nonlinear effects such as temporal solitons observed in this thesis. The squeezing of light in these temporal solitons could be investigated using an Sagnac interferometer [122] fabricate on-chip using ridge waveguides.

Preliminary work has already been conducted on ridge waveguide and has suggested that the transmission of a resonantly injected beam through the waveguide can be reduced by establishing a exciton reservoir using a non-resonant beam somewhere along its length. Alternatively with higher non-resonant excitation where exciton reservoir begins to dissociate the transmission through the waveguide could

actually be increased above that expected for pure photons which suggests the amplification of the polariton signal. A question for the future is whether the attenuation of the transmitted signal is due to interaction with the exciton reservoir which establishes a potential barrier as seen in microcavities [43] or if this is due to increased absorption by the broadened exciton line. This should be investigated using weak grating couplers along the length of the waveguide to observe the blueshift, if any, of the resonant beam. In either case the exciton reservoir could equally be created by electrical injection allowing for electrical control over the transmission. A further question is whether at high power the quenching of the strong coupling regime simply suppress losses in the waveguide or if the increase in transmission is actually an amplification by stimulated emission of radiation.

Finally it was also found that by changing duty period the grating couplers could be made to act as second order DBR mirrors forming a Fabry-Pérot cavity along the length of the wire. The spacing between these modes observed in the PL emission was found to change with the length of the wire. At high power where excitons in the reservoir begin to dissociate it was found that one of these modes would blueshift and increase nonlinearly in intensity. This too poses a question for the future, as whether this nonlinear increase in emission is due to the lasing which could be investigated through the coherence properties of the emission. In any case the leaked emission through the DBR mirrors formed by the grating could be fed into another waveguide where the strong-coupling regime is regained. The free carriers here could also be electrically injected to create an electrically controlled source of polaritons on-chip.

In conclusion the work described in this thesis lays the foundation for further studies into waveguide polaritons. It re-establishes the waveguide polaritons as an alternative to microcavities and highlights their specific advantages for the creation of polaritonic devices and to all-optical information processing.

Appendix A

Fitting the polariton dispersion

Characteristic information about the polariton dispersion can be extracted from angle-resolved PL spectra by fitting to a two coupled-oscillator model. This appendix describes how this was achieved.

Angle-resolved spectra were first rescaled into energy-momentum space. The position of the LPB was then extracted from the spectrum by fitting a Lorentzian function to cross sections taken at a particular energy. In order to achieve a robust fit the two coupled-oscillator model must first be rearranged. Recalling Equation 1.8 and neglecting the contributions of the photon and exciton linewidths the energy of the LPB is:

$$E_{LP}(\beta) = \frac{1}{2}\left(E_C(\beta) + E_X - \sqrt{(\hbar\Omega)^2 + \Delta^2}\right) \tag{A.1}$$

where $\Delta = E_c(\beta) - E_x$. Denoting $\delta = E_{LP}(\beta) - E_X$ Equation A.1 can be rearranged to give:

$$\left(\frac{\Omega}{2}\right)^2 = \delta^2 + \delta\Delta \tag{A.2}$$

Within the narrow range of energies spanning the anti-crossing region the photonic waveguide mode can be approximated as a linear function of wavenumber as in Equation 1.3. Substituting into Equation A.2 yields:

$$\left(\frac{\Omega}{2}\right)^2 = \delta^2 + \delta\left(\hbar v_g^c \beta + E_0 - E_X\right) \tag{A.3}$$

Plotting $\delta\beta$ versus δ yields a 2^{nd} order polynomial in δ which can be fitted using the least squares method to obtain the Rabi splitting and group velocity of the bare

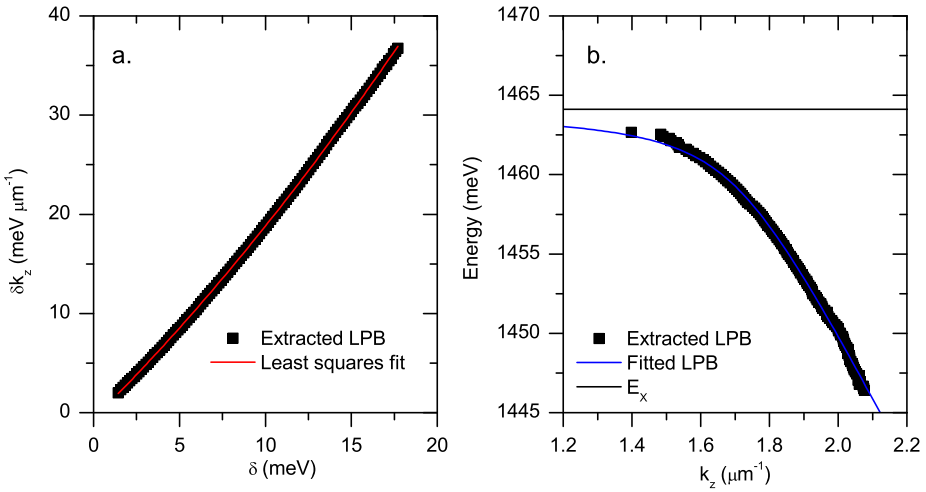

Figure A.1: Detuning of the LPB multiplied by the external in-plane wavenumber plotted against the detuning showing the result of a least squares fit (a). Extracted dispersion and fitted dispersion using coefficients from least squares fit (b).

waveguide. As the effect of the diffraction grating coupler is to shift the dispersion in momentum space by $\pm\Lambda$ this can further be simplified using the external wavenumber k_z by instead plotting δk_z versus δ.

Figure A.1a shows the extracted position of LPB in this rearranged parameter space and the result of a least squares polynomial fit. The coefficients were then rearranged to give the device parameters and used to calculate the dispersion shown in Figure A.1b.

Appendix B

Analytical soliton solution

The set of equations describing the exciton-photon coupling accounting for the dominant nonlinearity arising from two-body interactions between excitons is given by Equations 5.1. Neglecting loss ($\gamma_C = \gamma_X = 0$) and disregarding diffraction transverse to the direction of travel ($\partial_x^2 A = 0$) this reduces to:

$$2i\beta\left(\partial_z + v_g^{-1}\partial_t\right)A = -k_X^2\psi \tag{B.1a}$$

$$-2i\partial_t\psi = \kappa A - g|\psi|^2\psi \tag{B.1b}$$

The conservative solitonic solutions are parameterised by the soliton frequency δ_s and velocity v_s and can be sought in the form:

$$\psi = \rho_\psi e^{i\delta_s\tau + i\theta_\psi} \tag{B.2a}$$

$$Ai = \rho_A e^{i\delta_s\tau + i\theta_A} \tag{B.2b}$$

where ρ_ψ, ρ_A, θ_ψ and ρ_A are all real functions of $\tau = t - zv_s$. Substituting the anzats from Equations B.2 we obtain expression for the amplitudes ρ_ψ and ρ_A of the field:

$$\rho_\psi^2 = \frac{1}{g\mu}\frac{4\sigma(1-\sigma^2\mu^2\delta_s^2)}{\cosh(\frac{\sigma}{\mu}\sqrt{1-\sigma^2\mu^2\delta_s^2}\tau) + \sigma\mu\delta_s} \tag{B.3a}$$

$$\rho_A = \sigma\rho_\psi \tag{B.3b}$$

where $\sigma^2 - \frac{v_s}{v_s - v_g}$ and $\mu^2 = \frac{\beta}{\kappa v_g k^2}$.

The expression for the phases θ_ψ and θ_A of the fields are given by the integrals:

$$\theta_\psi = \frac{1}{2}\sigma^2\delta_s\tau - \frac{3g}{8} - \int_{-\infty}^{\tau} \rho_\psi^2 d\tau' \tag{B.4a}$$

$$\theta_A = \frac{1}{2}\sigma^2\delta_s\tau - \frac{g}{8} - \int_{-\infty}^{\tau} \rho_A^2 d\tau' \tag{B.4b}$$

Bibliography

[1] J. J. Hopfield, "Theory of the contribution of excitons to the complex dielectric constant of crystals," *Physical Review*, vol. 112, no. 5, pp. 1555–1567, 1958.

[2] D. Fröhlich, E. Mohler, and P. Wiesner, "Observation of exciton polariton dispersion in CuCl," *Physical Review Letters*, vol. 26, no. 10, pp. 554–556, 1971.

[3] U. Heim and P. Wiesner, "Direct evidence for a bottleneck of exciton-polariton relaxation in CdS," *Physical Review Letters*, vol. 30, no. 24, pp. 1205–1207, 1978.

[4] C. Weisbuch, M. Nishioka, A. Ishikawa, and Y. Arakawa, "Observation of the coupled exciton-photon mode splitting in a semiconductor quantum microcavity," *Physical Review Letters*, vol. 69, no. 23, pp. 3314–3317, 1992.

[5] A. V. Kavokin, J. J. Baumberg, G. Malpuech, and F. P. Laussy, *Microcavities*. Oxford University Press, 2007.

[6] B. Deveaud, ed., *The physics of semiconductor microcavities*. Wiley-VCH Verlag GmbH & Co. KGaA, 2007.

[7] D. Sanvitto and V. Timofeev, eds., *Exciton Polaritons in Microcavities: New Frontiers*. Springer Series in Solid-State Sciences, Heidelberg: Springer, 2012.

[8] P. G. Savvidis, J. J. Baumberg, R. M. Stevenson, M. S. Skolnick, D. M. Whittaker, and J. S. Roberts, "Angle-resonant stimulated polariton amplifier," *Physical Review Letters*, vol. 84, pp. 1547–50, Feb. 2000.

[9] R. M. Stevenson, V. N. Astratov, M. S. Skolnick, D. M. Whittaker, M. Emam-Ismail, A. J. Tartakovskii, P. G. Savvidis, J. J. Baumberg, and J. S. Roberts, "Continuous wave observation of massive polariton redistribution by stimulated scattering in semiconductor microcavities," *Physical Review Letters*, vol. 85, pp. 3680–3, Oct. 2000.

[10] H. Deng, G. Weihs, C. Santori, J. Bloch, and Y. Yamamoto, "Condensation of semiconductor microcavity exciton polaritons.," *Science (New York, N.Y.)*, vol. 298, pp. 199–202, Oct. 2002.

[11] J. Kasprzak, M. Richard, S. Kundermann, A. Baas, P. Jeambrun, J. M. J. Keeling, F. M. Marchetti, M. H. Szymaska, R. André, J. L. Staehli, V. Savona, P. B. Littlewood, B. Deveaud, and Le Si Dang, "Bose-Einstein condensation of exciton polaritons.," *Nature*, vol. 443, pp. 409–414, Sept. 2006.

[12] K. G. Lagoudakis, M. Wouters, M. Richard, a. Baas, I. Carusotto, R. André, L. S. Dang, and B. Deveaud-Plédran, "Quantized vortices in an excitonpolariton condensate," *Nature Physics*, vol. 4, pp. 706–710, Aug. 2008.

[13] D. Sanvitto, F. M. Marchetti, M. H. Szymaska, G. Tosi, M. Baudisch, F. P. Laussy, D. N. Krizhanovskii, M. S. Skolnick, L. Marrucci, a. Lemaître, J. Bloch, C. Tejedor, and L. Viña, "Persistent currents and quantized vortices in a polariton superfluid," *Nature Physics*, vol. 6, pp. 527–533, May 2010.

[14] A. Amo, J. Lefrère, S. Pigeon, C. Adrados, C. Ciuti, I. Carusotto, R. Houdré, E. Giacobino, and A. Bramati, "Superfluidity of polaritons in semiconductor microcavities," *Nature Physics*, vol. 5, pp. 805–810, Sept. 2009.

[15] T. C. H. Liew, A. V. Kavokin, and I. A. Shelykh, "Optical Circuits Based on Polariton Neurons in Semiconductor Microcavities," *Physical Review Letters*, vol. 101, pp. 1–4, July 2008.

[16] H. S. Nguyen, D. Vishnevsky, C. Sturm, D. Tanese, D. Solnyshkov, E. Galopin, A. Lemaître, I. Sagnes, A. Amo, G. Malpuech, and J. Bloch, "Realization of

a Double-Barrier Resonant Tunneling Diode for Cavity Polaritons," *Physical Review Letters*, vol. 110, p. 236601, June 2013.

[17] T. Gao, P. Eldridge, T. Liew, S. Tsintzos, G. Stavrinidis, G. Deligeorgis, Z. Hatzopoulos, and P. Savvidis, "Polariton condensate transistor switch," *Physical Review B*, vol. 85, p. 235102, June 2012.

[18] D. Ballarini, M. De Giorgi, E. Cancellieri, R. Houdré, E. Giacobino, R. Cingolani, A. Bramati, G. Gigli, and D. Sanvitto, "All-optical polariton transistor.," *Nature communications*, vol. 4, p. 1778, Jan. 2013.

[19] S. I. Tsintzos, N. T. Pelekanos, G. Konstantinidis, Z. Hatzopoulos, and P. G. Savvidis, "A GaAs polariton light-emitting diode operating near room temperature.," *Nature*, vol. 453, pp. 372–5, May 2008.

[20] S. I. Tsintzos, P. G. Savvidis, G. Deligeorgis, Z. Hatzopoulos, and N. T. Pelekanos, "Room temperature GaAs exciton-polariton light emitting diode," *Applied Physics Letters*, vol. 94, no. 7, p. 071109, 2009.

[21] M. Z. Baten, P. Bhattacharya, T. Frost, S. Deshpande, A. Das, D. Lubyshev, J. M. Fastenau, and A. W. K. Liu, "GaAs-based high temperature electrically pumped polariton laser," *Applied Physics Letters*, vol. 104, p. 231119, June 2014.

[22] P. Cilibrizzi, A. Askitopoulos, M. Silva, F. Bastiman, E. Clarke, J. M. Zajac, W. Langbein, and P. G. Lagoudakis, "Polariton condensation in a strain-compensated planar microcavity with InGaAs quantum wells," *Applied Physics Letters*, vol. 105, p. 191118, Nov. 2014.

[23] L. Tinkler, P. M. Walker, E. Clarke, D. N. Krizhanovskii, F. Bastiman, M. Durska, and M. S. Skolnick, "Design and characterization of high optical quality InGaAs/GaAs/AlGaAs-based polariton microcavities," *Applied Physics Letters*, vol. 106, p. 021109, Jan. 2015.

[24] A. I. Tartakovskii, V. D. Kulakovskii, A. Forchel, and J. P. Reithmaier, "Exciton-photon coupling in photonic wires," *Physical Review B*, vol. 57, no. 12, pp. 6807–6810, 1998.

[25] T. Jacqmin, I. Carusotto, I. Sagnes, M. Abbarchi, D. Solnyshkov, G. Malpuech, E. Galopin, A. Lemaître, J. Bloch, and A. Amo, "Direct Observation of Dirac Cones and a Flatband in a Honeycomb Lattice for Polaritons," *Physical Review Letters*, vol. 112, p. 116402, Mar. 2014.

[26] C. Sturm, D. Tanese, H. S. Nguyen, H. Flayac, E. Galopin, a. Lemaître, I. Sagnes, D. Solnyshkov, A. Amo, G. Malpuech, and J. Bloch, "All-optical phase modulation in a cavity-polariton Mach-Zehnder interferometer.," *Nature communications*, vol. 5, p. 3278, Jan. 2014.

[27] K. Ogawa, T. Katsuyama, and H. Nakamura, "Time-of-flight measurement of excitonic polaritons in a GaAs/AlGaAs quantum well," *Applied Physics Letters*, vol. 53, no. 12, p. 1077, 1988.

[28] K. Ogawa, T. Katsuyama, and H. Nakamura, "Polarization dependence of excitonic-polariton propagation in a GaAs quantum-well waveguide," *Physical review letters*, vol. 64, no. 7, 1990.

[29] T. N. Oder, J. Y. Lin, and H. X. Jiang, "Propagation properties of light in AlGaN/GaN quantum-well waveguides," *Applied Physics Letters*, vol. 79, no. 16, p. 2511, 2001.

[30] K. Ogawa, T. Katsuyama, and M. Kawata, "Electric field dependence of the propagation of quantum-well exciton polaritons in a waveguide structure," *Physical Review B*, vol. 46, no. 20, 1992.

[31] T. Katsuyama and K. Hosomi, "Phase control of an exciton-polariton in a quantum well waveguide and its application to optical devices," *Microelectronic engineering*, vol. 63, pp. 23–26, 2002.

[32] F. Arith, A. Nizamuddin, A. A. Latiff, and T. Katsuyama, "Effects of Exciton-polariton on Mach-zehnder Interference Devices," *Research Journal of Applied Sciences, Engineering and Technology*, vol. 7, no. 15, pp. 3044–3048, 2014.

[33] D. Gerace and L. Andreani, "Quantum theory of exciton-photon coupling in photonic crystal slabs with embedded quantum wells," *Physical Review B*, vol. 75, pp. 1–12, June 2007.

[34] D. Bajoni, D. Gerace, M. Galli, J. Bloch, R. Braive, I. Sagnes, A. Miard, A. Lemaître, M. Patrini, and L. Andreani, "Exciton polaritons in two-dimensional photonic crystals," *Physical Review B*, vol. 80, pp. 1–4, Nov. 2009.

[35] G. Messin, J. Karr, A. Baas, G. Khitrova, R. Houdré, R. Stanley, U. Oesterle, and E. Giacobino, "Parametric Polariton Amplification in Semiconductor Microcavities," *Physical Review Letters*, vol. 87, p. 127403, Aug. 2001.

[36] D. N. Krizhanovskii, D. Sanvitto, A. P. D. Love, M. S. Skolnick, D. M. Whittaker, and J. S. Roberts, "Dominant effect of polariton-polariton interactions on the coherence of the microcavity optical parametric oscillator," *Physical Review Letters*, vol. 97, no. Sept. , pp. 1–4, 2006.

[37] D. N. Krizhanovskii, D. M. Whittaker, R. A. Bradley, K. Guda, D. Sarkar, D. Sanvitto, L. Vina, E. Cerda, P. Santos, K. Biermann, R. Hey, and M. S. Skolnick, "Effect of Interactions on Vortices in a Nonequilibrium Polariton Condensate," *Physical Review Letters*, vol. 104, pp. 1–4, Mar. 2010.

[38] T. Boulier, M. Bamba, A. Amo, C. Adrados, A. Lemaître, E. Galopin, I. Sagnes, J. Bloch, C. Ciuti, E. Giacobino, and A. Bramati, "Polariton-generated intensity squeezing in semiconductor micropillars.," *Nature communications*, vol. 5, p. 3260, 2014.

[39] S. L. Braunstein and P. van Loock, "Quantum information with continuous variables," *Reviews of Modern Physics*, vol. 77, no. April, p. 513, 2005.

[40] A. Verger, C. Ciuti, and I. Carusotto, "Polariton quantum blockade in a photonic dot," *Physical Review B*, vol. 73, p. 193306, May 2006.

[41] S. Dufferwiel, F. Fras, A. Trichet, P. M. Walker, F. Li, L. Giriunas, M. N. Makhonin, L. R. Wilson, J. M. Smith, E. Clarke, M. S. Skolnick, and D. N. Krizhanovskii, "Strong exciton-photon coupling in open semiconductor microcavities," *Applied Physics Letters*, vol. 104, p. 192107, May 2014.

[42] E. Wertz, L. Ferrier, D. D. Solnyshkov, R. Johne, D. Sanvitto, A. Lemaître, I. Sagnes, R. Grousson, A. V. Kavokin, P. Senellart, G. Malpuech, and J. Bloch, "Spontaneous formation and optical manipulation of extended polariton condensates," *Nature Physics*, vol. 6, pp. 860–864, Aug. 2010.

[43] C. Anton, T. C. H. Liew, G. Tosi, M. D. Martin, T. Gao, Z. Hatzopoulos, P. S. Eldridge, P. G. Savvidis, and L. Vina, "Dynamics of a polariton condensate transistor switch," *Applied Physics Letters*, vol. 101, no. 26, p. 261116, 2012.

[44] J. Schmutzler, P. Lewandowski, M. Aßmann, D. Niemietz, S. Schumacher, M. Kamp, C. Schneider, S. Höfling, and M. Bayer, "All-optical flow control of a polariton condensate using nonresonant excitation," *Physical Review B*, vol. 91, no. 19, p. 195308, 2015.

[45] E. Wertz, A. Amo, D. Solnyshkov, L. Ferrier, T. Liew, D. Sanvitto, P. Senellart, I. Sagnes, A. Lemaître, A. Kavokin, G. Malpuech, and J. Bloch, "Propagation and Amplification Dynamics of 1D Polariton Condensates," *Physical Review Letters*, vol. 109, Nov. 2012.

[46] J. S. Russell, "Report on waves," *Report of the fourteenth meeting of the British association for the advancement of science*, 1844.

[47] A. Chabchoub, O. Kimmoun, H. Branger, N. Hoffmann, D. Proment, M. Onorato, and N. Akhmediev, "Experimental Observation of Dark Solitons on the Surface of Water," *Physical Review Letters*, vol. 110, p. 124101, Mar. 2013.

[48] D. Duncan, "John Scott Russell's Soliton Wave Re-created."

[49] L. Mollenauer, R. H. Stolen, and J. P. Gordon, "Experimental observation of picosecond pulse narrowing and solitons in optical fibers," *Physical Review Letters*, vol. 45, no. 13, 1980.

[50] K. E. Strecker, G. B. Partridge, A. G. Truscott, and R. G. Hulet, "Formation and propagation of matter-wave soliton trains.," *Nature*, vol. 417, pp. 150–3, May 2002.

[51] M. Sich, D. N. Krizhanovskii, M. S. Skolnick, A. V. Gorbach, R. Hartley, D. V. Skryabin, E. A. Cerda-Méndez, K. Biermann, R. Hey, and P. V. Santos, "Observation of bright polariton solitons in a semiconductor microcavity," *Nature Photonics*, vol. 6, pp. 50–55, Nov. 2011.

[52] A. Amo, S. Pigeon, D. Sanvitto, V. G. Sala, R. Hivet, I. Carusotto, F. Pisanello, G. Leménager, R. Houdré, E. Giacobino, C. Ciuti, and A. Bramati, "Polariton superfluids reveal quantum hydrodynamic solitons.," *Science*, vol. 332, pp. 1167–70, June 2011.

[53] L. Khaykovich, F. Schreck, G. Ferrari, T. Bourdel, J. Cubizolles, L. D. Carr, Y. Castin, and C. Salomon, "Formation of a matter-wave bright soliton.," *Science (New York, N.Y.)*, vol. 296, pp. 1290–3, May 2002.

[54] S. Burger, K. Bongs, S. Dettmer, W. Ertmer, K. Sengstock, A. Sanpera, G. V. Shlyapnikov, and M. Lewenstein, "Dark solitons in Bose-Einstein condensates," *Physical Review Letters*, vol. 83, no. 25, 1999.

[55] P. Colman, C. Husko, S. Combrié, and I. Sagnes, "Temporal solitons and pulse compression in photonic crystal waveguides," *Nature Photonics*, vol. 4, no. December, 2010.

[56] A. Blanco-Redondo, C. Husko, D. Eades, Y. Zhang, J. Li, T. F. Krauss, and B. J. Eggleton, "Observation of soliton compression in silicon photonic crystals.," *Nature communications*, vol. 5, p. 3160, Jan. 2014.

[57] P. Dumais, a. Villeneuve, and J. S. Aitchison, "Bright temporal solitonlike pulses in self-defocusing AlGaAs waveguides near 800 nm.," *Optics letters*, vol. 21, pp. 260–2, Feb. 1996.

[58] R. Dekker, N. Usechak, M. Först, and A. Driessen, "Ultrafast nonlinear all-optical processes in silicon-on-insulator waveguides," *Journal of Physics D: Applied Physics*, vol. 40, pp. R249–R271, July 2007.

[59] S. Barland, J. R. Tredicce, M. Brambilla, L. A. L. Lugiato, S. B. Balle, M. Giudici, M. Miller, T. Maggipinto, L. Spinelli, G. Tissoni, T. Kn odl, and R. J ager, "Cavity solitons as pixels in semiconductor microcavities," *October*, vol. 419, pp. 699–702, 2002.

[60] O. Madelung, *Semiconductors: Data Handbook*. Springer-Verlag, 3rd ed., 2004.

[61] Q. V. Tran, S. Combrie, P. Colman, and A. De Rossi, "Photonic crystal membrane waveguides with low insertion losses," *Applied Physics Letters*, vol. 95, no. 6, p. 061105, 2009.

[62] R. G. Hunsperger, *Integrated optics*, vol. 42. Sept. 2004.

[63] W. Bogaerts and D. Vermeulen, "Off-chip coupling," in *Handbook of Silicon Photonics* (L. Vivien and L. Pavesi, eds.), ch. 3, pp. 97–133, Taylor & Francis, 2013.

[64] D. M. Beggs, M. A. Kaliteevski, S. Brand, R. A. Abram, V. V. Nikolaev, and A. V. Kavokin, "Interaction of quantum well excitons with evanescent plane electromagnetic waves," *Journal of Physics: Condensed Matter*, vol. 16, pp. 3401–3409, May 2004.

[65] D. M. Beggs, M. A. Kaliteevski, S. Brand, R. A. Abram, and A. V. Kavokin, "Waveguide polaritons: interaction of a quantum well exciton with an electromagnetic mode of a planar waveguide," *Physica Status Solidi (C)*, vol. 2, pp. 787–790, Feb. 2005.

[66] L. Andreani, "Exciton-polaritons in superlattices," *Physics Letters A*, vol. 192, no. August, pp. 99–109, 1994.

[67] A. Armitage, T. A. Fisher, M. S. Skolnick, D. M. Whittaker, and P. Kinsler, "Exciton polaritons in semiconductor quantum microcavities in a high magnetic field," *Physical Review B*, vol. 55, no. 24, pp. 395–403, 1997.

[68] D. M. Whittaker, P. Kinsler, T. A. Fisher, M. S. Skolnick, A. Armitage, A. M. Afshar, M. D. Sturge, and J. S. Roberts, "Motional Narrowing in Semiconductor Microcavities.," *Physical review letters*, vol. 77, pp. 4792–4795, Dec. 1996.

[69] A. V. Kavokin, "Motional narrowing of inhomogeneously broadened excitons in a semiconductor microcavity: Semiclassical treatment," *Physical Review B*, vol. 57, no. 7, pp. 3757–3760, 1998.

[70] Y. S. Kivshar and G. P. Agrawal, *Optical solitons: from fibers to photonic crystals*. Academic Press, 2003.

[71] B. J. Eggleton, R. E. Slusher, C. Martin de Sterke, P. A. Krug, and J. E. Sipe, "Bragg grating solitons.," *Physical review letters*, vol. 76, pp. 1627–1630, Mar. 1996.

[72] L. Ferrier, E. Wertz, R. Johne, D. Solnyshkov, P. Senellart, I. Sagnes, A. Lemaître, G. Malpuech, and J. Bloch, "Interactions in Confined Polariton Condensates," *Physical Review Letters*, vol. 106, pp. 1–4, Mar. 2011.

[73] P. Renucci, T. Amand, X. Marie, P. Senellart, J. Bloch, B. Sermage, and K. V. Kavokin, "Microcavity polariton spin quantum beats without a magnetic field: A manifestation of Coulomb exchange in dense and polarized polariton systems," *Physical Review B*, vol. 72, p. 075317, Aug. 2005.

[74] M. Vladimirova, S. Cronenberger, D. Scalbert, K. V. Kavokin, A. Miard, A. Lemaître, J. Bloch, D. Solnyshkov, G. Malpuech, and A. V. Kavokin,

"Polariton-polariton interaction constants in microcavities," *Physical Review B*, vol. 82, p. 075301, Aug. 2010.

[75] G. Khitrova and H. M. Gibbs, "Nonlinear optics of normal-mode-coupling semiconductor microcavities," *Reviews of Modern Physics*, vol. 71, pp. 1591–1639, Oct. 1999.

[76] M. J. LaGasse, K. K. Anderson, C. A. Wang, H. A. Haus, and J. G. Fujimoto, "Femtosecond measurements of the nonresonant nonlinear index in AlGaAs," *Applied Physics Letters*, vol. 56, no. 5, p. 417, 1990.

[77] C. J. Hamilton, B. Vögele, J. S. Aitchison, G. T. Kennedy, W. Sibbett, W. Biehlig, U. Peschel, T. Peschel, and F. Lederer, "Bright solitary pulses in AlGaAs waveguides at half the band gap.," *Optics letters*, vol. 21, pp. 1226–8, Aug. 1996.

[78] J. Zhang, Q. Lin, G. Piredda, R. W. Boyd, G. P. Agrawal, and P. M. Fauchet, "Optical solitons in a silicon waveguide.," *Optics express*, vol. 15, pp. 7682–8, June 2007.

[79] R. Chiao, E. Garmire, and C. Townes, "Self-trapping of optical beams," *Physical Review Letters*, vol. 13, no. 15, 1964.

[80] J. Bjorkholm and A. Ashkin, "CW self-focusing and self-trapping of light in sodium vapor," *Physical Review Letters*, no. 4, 1974.

[81] P. Kelley, "Self-focusing of optical beams," *Physical Review Letters*, no. 26, pp. 1005–1008, 1965.

[82] V. Zakharov and A. Rubenchik, "Instability of waveguides and solitons in nonlinear media," *Sov. Phys. JETP*, vol. 1011, no. September 1973, pp. 494–500, 1974.

[83] A. Shabat and V. Zakharov, "Exact theory of two-dimensional self-focusing and one-dimensional self-modulation of waves in nonlinear media," *Soviet Physics JETP*, vol. 34, no. 1, pp. 62–69, 1972.

[84] V. Zakharov and A. Shabat, "Interaction between solitons in a stable medium," *Sov. Phys. JETP*, vol. 37, no. 5, pp. 823–828, 1973.

[85] D. R. Andersen, D. E. Hooton, G. A. Swartzlander, and A. E. Kaplan, "Direct measurement of the transverse velocity of dark spatial solitons.," *Optics letters*, vol. 15, pp. 783–5, July 1990.

[86] G. A. Swartzlander Jr, D. R. Andersen, J. J. Regan, H. Lin and A. E. Kaplan, "Spatial dark-soliton stripes and grids in self-defocusing materials," *Physical Review Letters*, vol. 66, no. 12, 1991.

[87] J. S. Aitchison, A. M. Weiner, Y. Silberberg, M. K. Oliver, J. L. Jackel, D. E. Leaird, E. M. Vogel, and P. W. Smith, "Observation of spatial optical solitons in a nonlinear glass waveguide.," *Optics letters*, vol. 15, pp. 471–3, May 1990.

[88] M. Taya, M. Bashaw, M. Fejer, M. Segev, and G. Valley, "Observation of dark photovoltaic spatial solitons," *Physical Review A*, vol. 52, no. 4, 1995.

[89] V. Shandarov, D. Kip, M. Wesner, and J. Hukriede, "Observation of dark spatial photovoltaic solitons in planar waveguides in lithium niobate," *Journal of Optics A: Pure and Applied Optics*, vol. 2, pp. 500–503, Sept. 2000.

[90] G. Duree, M. Morin, and G. Salamo, "Dark photorefractive spatial solitons and photorefractive vortex solitons," *Physical Review Letters*, vol. 74, no. 11, 1995.

[91] B. Luther-Davies and X. Yang, "Steerable optical waveguides formed in self-defocusing media by using dark spatial solitons," *Opt. Lett*, vol. 17, no. 24, pp. 1755–1757, 1992.

[92] M. Chauvet, S. Chauvin, and H. Maillotte, "Transient dark photovoltaic spatial solitons and induced guiding in slab LiNbO(3) waveguides.," *Optics letters*, vol. 26, pp. 1344–6, Sept. 2001.

[93] B. Luther-Davies and Y. Xiaoping, "Waveguides and Y junctions formed in bulk media by using dark spatial solitons.," *Optics letters*, vol. 17, pp. 496–8, Apr. 1992.

[94] A. A. Sukhorukov and N. N. Akhmediev, "Multiport soliton devices with controllable transmission.," *Optics letters*, vol. 28, pp. 908–10, June 2003.

[95] L. Pitaevskii and S. Stringari, *Bose-Einstein Condensation*. Oxford: Oxford University Press, 2003.

[96] J. Denschlag, "Generating Solitons by Phase Engineering of a Bose-Einstein Condensate," *Science*, vol. 287, no. 5450, pp. 97–101, 2000.

[97] D. Tanese, D. Solnyshkov, A. Amo, L. Ferrier, E. Bernet-Rollande, E. Wertz, I. Sagnes, A. Lemaître, P. Senellart, G. Malpuech, and J. Bloch, "Backscattering Suppression in Supersonic 1D Polariton Condensates," *Physical Review Letters*, vol. 108, pp. 1–5, Jan. 2012.

[98] R. Hivet, H. Flayac, D. D. Solnyshkov, D. Tanese, T. Boulier, D. Andreoli, E. Giacobino, J. Bloch, A. Bramati, G. Malpuech, and A. Amo, "Half-solitons in a polariton quantum fluid behave like magnetic monopoles," *Nature Physics*, vol. 8, pp. 724–728, Aug. 2012.

[99] B. Nelsen, G. Liu, M. Steger, D. W. Snoke, R. Balili, K. West, and L. Pfeiffer, "Dissipationless Flow and Sharp Threshold of a Polariton Condensate with Long Lifetime," *Physical Review X*, vol. 3, Nov. 2013.

[100] O. A. Egorov, D. V. Skryabin, A. V. Yulin, and F. Lederer, "Bright Cavity Polariton Solitons," *Physical Review Letters*, vol. 102, pp. 17–20, Apr. 2009.

[101] O. A. Egorov, A. V. Gorbach, F. Lederer, and D. V. Skryabin, "Two-Dimensional Localization of Exciton Polaritons in Microcavities," *Physical Review Letters*, vol. 105, pp. 11–14, Aug. 2010.

[102] N. A. Gippius, I. A. Shelykh, D. D. Solnyshkov, S. S. Gavrilov, Yuri G. Rubo, A. V. Kavokin, S. G. Tikhodeev, and G. Malpuech, "Polarization Multista-

bility of Cavity Polaritons," *Physical Review Letters*, vol. 98, pp. 1–4, June 2007.

[103] M. Sich, F. Fras, J. K. Chana, M. S. Skolnick, D. N. Krizhanovskii, A. V. Gorbach, R. Hartley, D. V. Skryabin, S. S. Gavrilov, E. A. Cerda-Méndez, K. Biermann, R. Hey, and P. V. Santos, "Effects of Spin-Dependent Interactions on Polarization of Bright Polariton Solitons," *Physical Review Letters*, vol. 112, p. 046403, Jan. 2014.

[104] J. K. Chana, M. Sich, F. Fras, A. V. Gorbach, D. V. Skryabin, E. Cancellieri, K. Biermann, R. Hey, P. V. Santos, M. S. Skolnick, and D. N. Krizhanovskii, "Spatial patterns of dissipative polariton solitons in semiconductor microcavities," *arXiv*, 1407.7713v1, July 2014

[105] A. Amo, D. Sanvitto, F. P. Laussy, D. Ballarini, E. del Valle, M. D. Martin, A. Lemaître, J. Bloch, D. N. Krizhanovskii, M. S. Skolnick, C. Tejedor, and L. Viña, "Collective fluid dynamics of a polariton condensate in a semiconductor microcavity.," *Nature*, vol. 457, pp. 291–295, Jan. 2009.

[106] S. Utsunomiya, L. Tian, G. Roumpos, C. W. Lai, N. Kumada, T. Fujisawa, M. Kuwata-Gonokami, a. Löffler, S. Höfling, a. Forchel, and Y. Yamamoto, "Observation of Bogoliubov excitations in exciton-polariton condensates," *Nature Physics*, vol. 4, pp. 700–705, Aug. 2008.

[107] P. K. Rastogi, *Holographic Interferometry: Principles and Methods*. Springer Series on Wave Phenomena, Springer, 1994.

[108] P. M. Walker, L. Tinkler, M. Durska, D. M. Whittaker, D. N. Krizhanovskii, M. S. Skolnick, I. Farrer, and D. Ritchie, "Exciton Polaritons in Semiconductor Waveguides," *Applied Physics Letters*, vol. 102, p. 012109, 2013.

[109] R. Houdre, J. L. Gibernon, P. Pellandini, R. P. Stanley, U. Oesterle, C. Weisbuch, J. O'Gorman, B. Roycroft, and M. Ilegems, "Saturation of the strong-coupling regime in a semiconductor microcavity: Free-carrier bleaching of cavity polaritons," vol. 52, no. 11, pp. 7810–7813, 1995.

[110] V. Savona and L. Andreani, "Quantum well excitons in semiconductor microcavities: Unified treatment of weak and strong coupling regimes," *Solid State Communications*, vol. 93, no. 9, pp. 733–739, 1995.

[111] R. Houdré, R. P. Stanley, U. Oesterle, M. Ilegems, and C. Weisbuch, "Room-temperature cavity polaritons in a semiconductor microcavity," *Physical Review B*, vol. 49, no. 23, pp. 761–764, 1994.

[112] S. Christopoulos, G. von Högersthal, A. Grundy, P. Lagoudakis, A. Kavokin, J. Baumberg, G. Christmann, R. Butté, E. Feltin, J.-F. Carlin, and N. Grandjean, "Room-Temperature Polariton Lasing in Semiconductor Microcavities," *Physical Review Letters*, vol. 98, pp. 1–4, Mar. 2007.

[113] D. Gammon, S. Rudin, T. L. Rein, D. Katzer, and C. S. Kyono, "Phonon broadening of excitons in GaAs-AlGaAs quantum wells," *Physical Review Bys*, vol. 51, no. 23, 1995.

[114] L. Kappei, J. Szczytko, F. Morier-Genoud, and B. Deveaud, "Direct Observation of the Mott Transition in an Optically Excited Semiconductor Quantum Well," *Physical Review Letters*, vol. 94, p. 147403, Apr. 2005.

[115] D. Sarkar, S. S. Gavrilov, M. Sich, J. H. Quilter, R. A. Bradley, N. A. Gippius, K. Guda, V. D. Kulakovskii, M. S. Skolnick, and D. N. Krizhanovskii, "Polarization Bistability and Resultant Spin Rings in Semiconductor Microcavities," *Physical Review Letters*, vol. 105, pp. 1–4, Nov. 2010.

[116] A. V. Sekretenko, S. S. Gavrilov, and V. D. Kulakovskii, "Polariton-polariton interactions in microcavities under a resonant 10 to 100 picosecond pulse excitation," *Physical Review B*, vol. 88, p. 195302, Nov. 2013.

[117] D. N. Krizhanovskii, G. Dasbach, A. A. Dremin, V. D. Kulakovskii, N. A. Gippius, M. Bayer, and A. Forchel, "Impact of exciton localization on cavity polaritons," *Solid State Communications*, vol. 119, pp. 435–439, 2001.

[118] E. Hecht, *Optics*, vol. 1. Addison-Wesley, 4th ed., 2001.

[119] L. Tinkler, P. M. Walker, D. V. Skryabin, A. Yulin, B. Royall, I. Farrer, D. A. Ritchie, D. N. Krizhanovskii, and M. S. Skolnick, "Ultra-Low-Power Hybrid Light-Matter Solitons," *arXiv*, 1409.0725, Sept 2014.

[120] J. Liao, M. Marko, X. Li, H. Jia, J. Liu, Y. Tan, J. Yang, Y. Zhang, W. Tang, M. Yu, G.-q. Lo, D.-l. Kwong, and C. W. Wong, "Cross-correlation frequency-resolved optical gating and dynamics of temporal solitons in silicon nanowire waveguides," vol. 38, no. 21, pp. 4401–4404, 2013.

[121] S. Friberg, S. Machida, and M. Werner, "Observation of optical soliton photon-number squeezing," *Physical Review Letters*, vol. 77, no. 18, pp. 3775–3778, 1996.

[122] M. Rosenbluh and R. Shelby, "Squeezed optical solitons," *Physical Review Letters*, vol. 66, no. 2, 1991.

[123] K. Hayata and M. Koshiba, "Bright-dark solitary-wave solutions of a multidimensional nonlinear Schrödinger equation," *Physical Review E*, vol. 48, no. 3, pp. 2312–2315, 1993.

[124] N. Bélanger, A. Villeneuve, and J. S. Aitchison, "Solitonlike pulses in self-defocusing AlGaAs waveguides," *Journal of the Optical Society of America B*, vol. 14, p. 3003, Nov. 1997.

[125] Feng Li, L. Orosz, O. Kamoun, S. Bouchoule, C. Brimont, P. Disseix, T. Guillet, X. Lafosse, M. Leroux, J. Leymarie, M. Mexis, M. Mihailovic, G. Patriarche, F. Réveret, D. Solnyshkov, J. Zuniga-Perez, and G. Malpuech, "From Excitonic to Photonic Polariton Condensate in a ZnO-Based Microcavity," *Physical Review Letters*, vol. 110, p. 196406, May 2013.